

# **Large-area fabrication of pyramidal plasmonic nanoprobes and their characterisation in tip-enhanced Raman spectroscopy applications**

## **Dissertation**

der Mathematisch-Naturwissenschaftlichen Fakultät  
der Eberhard Karls Universität Tübingen  
zur Erlangung des Grades eines  
Doktors der Naturwissenschaften  
(Dr. rer. nat.)

vorgelegt von  
Manuel Martina  
aus Leonberg

Tübingen  
2017

Gedruckt mit Genehmigung der Mathematisch-Naturwissenschaftlichen Fakultät  
der Eberhard Karls Universität Tübingen.

Tag der mündlichen Qualifikation:

24.08.2017

Dekan:

Prof. Dr. Wolfgang Rosenstiel

1. Berichterstatter

Prof. Dr. M. Fleischer

2. Berichterstatter

Prof. Dr. D. Wharam

*"If I have seen further, it is by standing on the shoulders of giants."*

Sir Isaac Newton, 1676



# Abstract

In tip-enhanced Raman spectroscopy (TERS), plasmonically active structures are utilised to confine and enhance the Raman signal in the range of some ten nanometres by several orders of magnitude. Yet today, the reproducible batch fabrication of suitable nano-antennas is still a challenging task, and thus limits the routine application of TERS.

In this work, a batch process to fabricate nanostructures suitable for different scanning probe microscopy (SPM) feedback mechanisms as well as for the realisation of surface-enhanced Raman spectroscopy (SERS) substrates is investigated. Therefore, a finite element method simulation to investigate the influence of geometrical parameters of the projected structures as well as parameters of the experimental set-up on the TERS performance is presented. It is found that for pyramidal gold probes a tip apex angle between  $30^\circ$  to  $70.5^\circ$  as well as the smallest possible tip radius are beneficial. In contrast, the orientation of the probe relative to the excitation beam for side illumination is found to be less influential within the typical experimental parameter range.

With this knowledge, the establishment of a known, batch fabrication compatible template stripping process is reported. This allows to fabricate metallic structures with smooth surfaces and nano-scale features which are suitable for TERS. As a result, pyramidal micro-cavities are achieved on the wafer-scale, and apex angles down to  $30^\circ$  as well as tip radii in the range of some nanometres are observed.

Furthermore, a release process yielding individual nano-antennas suitable for scanning tunnelling microscopy (STM) imaging and TER spectra acquisition is developed. The fabricated probes are characterised by scanning electron microscopy (SEM) and their STM properties are compared to standard tungsten probes. It is found that pyramidal gold tips with tip radii in the range of 25 nm are reliably achieved. These are operated with STM feedback, and topography imaging comparable to standard STM tips is possible.

Afterwards, the probes are utilised to collect tip-enhanced signals from clean gold surfaces, few dye molecules, ultra-thin layers of amorphous carbon and thin layers of PEDOT:PSS molecules, allowing to investigate their TERS properties. As a result, strong near-field signals are collected from all samples, and on suitable samples contrast factors of 10 and above are determined. Furthermore, it is found that a thin PEDOT:PSS layer provides a well-suited surface to verify near-field Raman spectroscopy due to a stable signal generation, sharp bands and compatibility to various SPM feedback mechanisms.

Additionally, a process to realise soft, polymeric cantilevers with template-stripped tips is developed. The cantilevers are characterised by SEM as well as by acquiring atomic force microscopy images and collecting TER spectra. In the first applications, near-field signals along linescans on carbon structures are collected and

the information is correlated to the imaged topography. Such a process can form the foundation for a wafer-scale fabrication of soft, polymeric TERS cantilevers for contact mode AFM feedback.

Finally, the application of template stripping for the fabrication of SERS substrates is shown. The fabricated substrates, featuring arrays of metal pyramids, are coated with dye molecules and SER spectra are collected. In this case, strong Raman signals are found at sharp features of the pyramidal metal structure: at the tips and at the edges. Besides showing the versatility of template stripping, a further development including sub-micron lithography techniques could allow for well-defined SERS substrates with high densities of hotspots.

# Zusammenfassung

Bei der spitzenverstärkten Raman-Spektroskopie (TERS) verwendet man plasmomische Strukturen, um das Raman-Signal auf Bereiche von einigen zehn Nanometern zu begrenzen und gleichzeitig um mehrere Größenordnungen zu verstärken. Jedoch stellt heutzutage die reproduzierbare Kleinserienproduktion von geeigneten Nanoantennen immer noch eine anspruchsvolle Aufgabe dar und schränkt die routinemäßige Durchführung von TERS-Analysen ein.

Im Rahmen dieser Arbeit wird ein Prozess für die Kleinserienherstellung von Nanostrukturen für verschiedene Rastersondenmikroskopie-Verfahren wie auch für die Realisierung von Substraten für die oberflächenverstärkte Raman-Spektroskopie (SERS) untersucht. Dafür wird zuerst eine Simulation basierend auf der Methode der finiten Elemente vorgestellt, um die Einflüsse von geometrischen Parametern der beabsichtigten Spitzengeometrie wie auch von Parametern des experimentellen Aufbaus auf die TERS-Eigenschaften zu untersuchen. Dabei zeigt sich, dass für pyramidenförmige Goldsonden ein Apexwinkel zwischen  $30^\circ$  bis  $70.5^\circ$  sowie ein möglichst kleiner Spitzenradius von Vorteil sind. Im Gegensatz dazu beeinflusst die Orientierung der Sonde relativ zum anregenden Laserstrahl bei der Beleuchtung von der Seite, innerhalb der für die Experimente typischen Bereiche, die Feldverstärkung weniger.

Anhand dieser Ergebnisse wird die Etablierung einer bekannten Methode zur Übertragung einer Vorlagenform 'template stripping' vorgestellt. Dieser Prozess erlaubt die Herstellung von metallischen Strukturen mit glatten Oberflächen und Geometrien im Bereich von Nanometern, welche zur Anwendung als TERS-Sonden geeignet sind. Infolgedessen werden pyramidenförmige Aushöhlungen mit Dimensionen im Bereich von einigen zehn Mikrometern auf Waferbasis erzeugt und Apexwinkel bis zu  $30^\circ$  sowie Spitzenradien im Bereich einiger Nanometer sind messbar.

Weiterhin wird ein Prozess zum Herauslösen einzelner Nanoantennen entwickelt, welche sowohl für die Rastertunnelmikroskopie (STM) als auch für TERS geeignet sind. Die hergestellten Sonden werden mit Hilfe der Rasterelektronenmikroskopie charakterisiert und ihre STM-Eigenschaften werden mit üblichen Wolframsonden verglichen. Es zeigt sich, dass Goldspitzen mit Radien im Bereich von 25 nm zuverlässig erzeugt werden können. Diese werden im Rastertunnelmikroskop eingesetzt und Aufnahmen von Oberflächen, vergleichbar wie sie mit üblichen STM-Sonden erreicht werden, sind möglich.

Im Anschluss werden die Sonden verwendet, um spitzenverstärkte Signale von reinen Goldoberflächen, einigen Farbmolekülen, ultradünnen amorphen Kohlenstoffschichten und dünnen Schichten aus PEDOT:PSS Molekülen zu messen. Dies erlaubt die TERS-Eigenschaften der Sonden zu untersuchen. Infolgedessen werden starke Nahfeldsignale von diesen Oberflächen gemessen, und bei geeigneten Oberflächen werden Kontrastfaktoren von über 10 für die Spitzen festgestellt. Weiter-

hin zeigt sich, dass dünne PEDOT:PSS Schichten sehr geeignet sind um Nahfeld-Raman-Spektroskopie zu verifizieren, da sie ein stabiles Signal generieren, schmale Raman-Banden aufweisen und kompatibel zu verschiedenen SPM Steuersignalen sind.

Zusätzlich wird ein Prozess zur Realisierung von weichen Polymercantilvern mit Hilfe von 'template stripping' entwickelt. Die Cantilever werden mit Hilfe der Rasterelektronenmikroskopie charakterisiert sowie durch den Einsatz zur Bildgebung im Rasterkraftmikroskop und durch Messen von TERS Signalen untersucht. Bei den ersten Anwendungen werden Nahfeld-Signale entlang Linienmessungen an Kohlenstoffstrukturen gemessen und die Information wird mit der abgebildeten Topographie korreliert. Solch ein Herstellungsprozess kann die Basis für eine Fabrikation von weichen Polymercantilvern auf der Waferskala bilden, welche geeignet sind für TERS in Kombination mit Kontaktmodus AFM.

Schließlich wird die Anwendung von 'template stripping' für die Herstellung von SERS Substraten gezeigt. Diese Substrate, welche regelmäßige Anordnungen von metallischen Pyramiden aufweisen, werden mit Farbstoffmolekülen beschichtet und SER Spektren werden gemessen. Es zeigt sich dabei, dass starke Raman Signale an scharfen geometrischen Merkmalen der pyramidenförmigen Metallstrukturen gefunden werden: an den Spitzen und den Kanten. Daneben zeigt sich die Vielseitigkeit von 'template stripping', und eine Weiterentwicklung durch die Anwendung von Lithographietechniken mit Auflösungen unter der Mikrometerskala könnte die Herstellung von wohl definierten SERS Substraten mit hohen Hotspotdichten erlauben.

# Abbreviations

AFM	Atomic force microscopy / microscope
CARS	Coherent anti-Stokes Raman spectroscopy
DNA	Desoxyribonucleic acid
EBID	Electron beam-induced deposition
EDS	Energy-dispersive X-ray spectroscopy
FIB	Focused ion beam
FRET	Förster resonance energy transfer
HIM	Helium ion microscopy / microscope
LSP	Localised surface plasmon
MEMS	Microelectromechanical systems
PECVD	Plasma-enhanced chemical vapour deposition
PIRET	Plasmoninduced resonance energy transfer
PVD	Physical vapour deposition
RIE	Reactive ion etching
SEM	Scanning probe microscopy / microscope
SERS	Surface enhanced Raman spectroscopy
SNOM	Scanning near field optical microscopy / microscope
SPM	Scanning probe microscopy / microscope
SPP	Surface plasmon polariton
STM	Scanning tunnelling microscopy / microscope
TER	Tip-enhanced Raman
TERS	Tip-enhanced Raman spectroscopy



# Contents

<b>Abstract</b>	<b>iii</b>
<b>Zusammenfassung</b>	<b>v</b>
<b>Abbreviations</b>	<b>vii</b>
<b>1. Motivation and Objectives</b>	<b>1</b>
<b>2. Introduction</b>	<b>3</b>
2.1. Plasmonics . . . . .	3
2.2. Raman spectroscopy . . . . .	5
2.3. Tip-enhanced Raman spectroscopy . . . . .	7
2.4. Plasmonic Nanostructures for TERS . . . . .	8
<b>3. Basic Principles</b>	<b>13</b>
3.1. Scanning tunnelling microscopy . . . . .	13
3.2. Raman scattering . . . . .	15
3.3. Plasmonics . . . . .	18
3.4. Tip-enhanced Raman scattering . . . . .	22
3.5. Finite element method . . . . .	25
<b>4. Materials and Methods</b>	<b>27</b>
4.1. Computational Modelling and Simulation . . . . .	28
4.2. Silicon mould fabrication . . . . .	32
4.2.1. Silicon etching . . . . .	32
4.2.2. Oxidation and Metallization . . . . .	35
4.3. Fabrication of STM TERS probes . . . . .	37
4.3.1. Bonding and Release . . . . .	37
4.3.2. Adapter pieces and glueing . . . . .	37
4.3.3. Tungsten STM probe fabrication . . . . .	40
4.4. Fabrication of TERS cantilevers . . . . .	41
4.4.1. Structuring of the cantilevers . . . . .	41
4.4.2. Release of the cantilevers . . . . .	44
4.5. Fabrication of SERS substrates . . . . .	45
4.6. Sample fabrication . . . . .	47
4.6.1. Gold on silicon . . . . .	47
4.6.2. Malachite green isothiocyanate (MGITC) samples . . . . .	47
4.6.3. Amorphous carbon samples . . . . .	48
4.6.4. Thin PEDOT:PSS coating . . . . .	49

<b>5. Experimental set-up</b>	<b>51</b>
5.1. Raman set-up . . . . .	51
5.2. Raman characterisation and measurements . . . . .	53
5.3. SPM set-up and measurements . . . . .	53
5.4. Raman-SPM coupling for TERS . . . . .	55
<b>6. Results and Discussion</b>	<b>57</b>
6.1. Computational Modelling and Simulation . . . . .	58
6.2. Silicon mould fabrication . . . . .	65
6.2.1. Wet etching of pyramidal cavities in silicon . . . . .	65
6.2.2. Oxidation and Metallisation . . . . .	69
6.3. Fabrication of STM TERS probes . . . . .	73
6.3.1. Bonding and Release . . . . .	73
6.3.2. Analytical Characterisation . . . . .	75
6.4. Scanning tunnelling microscopy and tip-enhanced Raman spectroscopy	79
6.4.1. STM imaging of a sputtered gold surface . . . . .	80
6.4.2. Near-field measurements on gold . . . . .	84
6.4.3. Tip-enhanced Raman spectroscopy on a malachite green covered gold surface . . . . .	86
6.4.4. Investigation of ultra-thin amorphous carbon layers . . . . .	89
6.4.5. Mapping concentration variations of PEDOT:PSS on the nano-scale . . . . .	92
6.5. Template stripping of AFM TERS cantilevers . . . . .	96
6.5.1. Fabrication of metal, beam and chip . . . . .	97
6.5.2. Cantilever release . . . . .	99
6.5.3. AFM TERS measurements . . . . .	100
6.6. Template stripping of SERS substrates . . . . .	103
6.6.1. Fabrication of SERS substrates . . . . .	103
6.6.2. SERS measurements . . . . .	105
<b>7. Summary and Outlook</b>	<b>109</b>
<b>Bibliography</b>	<b>113</b>
<b>A. Appendix</b>	<b>121</b>

# 1. Motivation and Objectives

## Motivation

People perceive their environment with five main biological senses: vision, hearing, olfaction, gustation and tactile sense. Being able to observe and measure something is the prerequisite for understanding and interaction. Furthermore, the performance of an organism's senses directly influences its capabilities. For example, the human eye collects photons scattered from objects to use this information for visual image generation. Thereby, it is capable to differentiate between over  $10^6$  colours and, according to recent results, detect a single photon [1]. Simultaneously, it is able to perform over fourteen orders of luminance and change its entrance pupil diameter between 2 mm to 8 mm. Thus, this high performance organ is estimated to acquire up to 80 % of the perceived information for humans.

In science, the first step of observation and measurement is performed by probing for something and recording the response. Instead of senses for perception, specialised detectors can be utilised. These allow for new forms and choices of probes, each offering certain advantages and implicating other disadvantages. Such probes could be waves, particles or physical structures.

In Raman spectroscopy, one detects photons which are inelastically scattered from matter to acquire information about chemical composition, material properties and physical state. A further development thereof is tip-enhanced Raman spectroscopy (TERS), a relatively young technique which allows to acquire Raman information on the nanometre scale. Instead of a laser spot, specifically manufactured nano-antennas are utilised to concentrate the probing photons to a small spot and likewise amplify the generated photons carrying the response.

The probe in tip-enhanced Raman spectroscopy could be regarded as the combination of nano-antenna and laser photons. While the latter can nowadays reliably be generated, the reproducible fabrication of nano-antennas for this purpose is still a challenging task. One reason for this is the relevant length scale of such structures, which is in the range of some ten nanometres and therefore, only accessible by complex techniques.

The present work is settled in the fields of nano- and microfabrication, plasmonics, scanning probe microscopy (SPM) and (tip-enhanced) Raman spectroscopy. It addresses the need for a reproducible fabrication process of nano-antennas, which is a fundamental requirement to establish tip-enhanced Raman spectroscopy as an accessible and common technique.

The possibility to reliably investigate samples of interest by TERS, and reproducibly measure tip-enhanced Raman spectroscopy on the nano-scale, possibly enables the observation of new science. Thereafter, interaction with and manipulation of nano-scaled systems can be performed.

## **Research Objectives**

The aim of this work was the development of a batch fabrication process for SPM probes, which are suitable for TERS. The properties of the fabricated probes in terms of geometry and surface roughness should be investigated and the probes should be tested for SPM and TERS performance.

The first objective was the establishment and further development of an already reported process for mould fabrication, which allows template stripping of smooth-surfaced metal pyramids with tip radii of some ten nanometres. Gold was investigated as the tip material to allow the application of such structures in TERS with an excitation wavelength of 633 nm. This process formed the basis for further fabrication of probes.

Next, the second objective was the successful development of methods to utilise the metal pyramids as SPM probe tips. Therefore, a bonding process for the controlled attachment to a wire and release from the substrate, yielding probes for STM or non-contact lateral force microscopy, was developed. Additionally, the fabrication of cantilevers featuring such metal pyramids as tips was a possibility to achieve the objective. Finally, a controlled release of an array of metal pyramids could be a method to fabricate a surface for SERS measurements.

The third objective of this work was the characterisation of the fabricated tips with respect to their nano-scale features and surface quality. To achieve this, high resolution imaging techniques like SEM and HIM were employed. Also, the fabricated probes were utilised in SPM measurements and the image quality was compared to images obtained with standard probes. Although SPM performance was not a key aspect of this work, good functionality of the tips with the respective feedback mechanism was needed to achieve stable TER signals. Furthermore, reproducibility of the tip fabrication had to be evaluated with respect to the TERS performance of the tips.

Finally, the fourth objective was the application of the fabricated probes in TERS and a comparison of the performance to results from others achieved with different probes. As a first step into TERS, substrates specifically coated with small surface concentrations of dye molecules were used to test the functionality of the set-up. Furthermore, a variety of samples were available, which could only be investigated by Raman spectroscopy with nanometre resolution and high sensitivity. For example, ultra-thin carbon layers or thin layers of PEDOT:PSS polymer could be fabricated. In this context, possible candidates which are suitable as a standardised TERS test sample were identified and investigated. This addressed the need for a reference, which can be utilised for objective comparison of TERS probes, TERS set-ups and plasmon excitation conditions.

## 2. Introduction

In the beginning of this chapter, a brief overview of the history of plasmonics is provided. Following, Raman spectroscopy and tip-enhanced Raman spectroscopy are introduced and the state-of-the-art of probe fabrication for the latter is discussed.

### 2.1. Plasmonics

The field of plasmon physics or plasmonics is not even a century old, but already underwent detailed fundamental research which still continues. This yielded an extensive theoretical description which is extended at a fast pace, gave rise to a great number of exciting experiments with surprising results and is pushing into applications in a broad variety of other subject areas. This first section grants a brief overview of the beginnings and a description of milestone experiments as well as some of today's *hot topics*.

In 1952, D. Pines and D. Bohm described the quantisation of oscillations of an electron gas in bulk metal which laid the foundations for plasmonics [2]. Prior to that, experiments conducted by G. Ruthemann and W. Lang allowed to observe material characteristic energy losses of around 20 eV of fast electrons when passing through a thin metal foil [3, 4].

This theory was supported by H. Watanabe in 1956 who investigated scattering angle dependent energy losses of 25 kV electrons passing through metal foils for a variety of materials [5]. He reported for several materials energy losses which could be attributed to bulk plasmon excitation as well as energy losses of unknown origin. Beside other effects which were discussed to explain this phenomenon, for example the interband transition of individual electrons [6], in 1957 R.H. Ritchie related the energy loss to the excitation of surface plasmons [7].

Henceforward, an increasing amount of experimental investigations of plasmon physics started. In 1960, R.W. Brown and W. Steinmann independently investigated the photon reradiation of plasmons in thin silver films [8, 9]. In both experiments, a silver layer was bombarded with electrons and the emitted photons were collected by a spectrometer with respect to the metal layer thickness or angular distribution. As result, the energy loss of the transmitted electrons could be attributed to the radiated photon energy.

Further experiments were conducted to allow for a more fundamental understanding and investigated different materials. For example, in 1966 B.W. Ninham extended the theory of plasmon damping in metals as a function of momentum transfer including polarisation effects [10] and in 1967 K. Zeppenfeld investigated the anisotropy of plasmon excitation in single graphite crystals as a function of the angle of incidence with respect to the lattice orientation [11].

Yet, experiments required an electron beam and could therefore only be conducted under vacuum conditions. This changed when in 1968 A. Otto [12] and E. Kretschmann [13] independently observed the excitation of surface plasmon polaritons by visible light. Both of them utilised total reflection in a prism, which generated evanescent waves. The latter couple to a metal film near the prism or deposited on the prism, and thus excite surface plasmon polaritons. Both techniques allowed for a wave vector matching of the visible light to the SPP. From there on, the physics of SPPs could be investigated utilising optical set-ups.

In the following years, there were numerous fascinating experiments reported, often yielding surprising results. In the work of P. Dawson et al., an optical fibre was placed in SPM feedback above a metal film, which was used to excite SPPs using the Kretschmann configuration [14]. The optical fibre was utilised to collect the electrical field of the SPPs, which extended in the dielectric medium, and thus allowed to image SPP propagation. In 1996, B. Hecht et al. reported the utilisation of a SNOM probe as point source for SPP excitation in metal. This allows to scan the point source over the metal film and use the reradiated optical signals to probe for the interaction of SPPs with the local metal properties [15].

Today, plasmonics has found application in different fields of physics, chemistry and biology. Besides its application in near-field Raman spectroscopy, which is a main topic of this work and is discussed later in detail, different devices incorporating integral plasmonically active components were developed. M.L. Juan et al. reported the fabrication of plasmon nano-optical tweezers, which were utilised to trap and align particles or bacteria in the nanometre range [16]. Therefore, single gold nanostructures or two nanostructures with a cavity in-between were fabricated and wetted with particles in solution. Upon the excitation of SPPs, polystyrene beads or bacteria were trapped in the resulting strong electrical fields at the structures. In comparison to conventional optical traps, stronger localisation and potential wells could be achieved.

J. Li et al. investigated the utilisation of plasmonic structures to facilitate a process opposite to FRET [17]. This allows to transfer energy non-radiatively from a red-shifted emitter to a blue-shifted absorber by dipole-dipole coupling. A distant objective could be the application in photovoltaics, where energy of the long-wavelength visible spectrum or the near-infrared could be efficiently harvested. Normally, the energy of such light lies below the semiconductor band gap.

Recently reported, E. Forati et al. proposed the application of plasmonic nanostructures to fabricate a transistor combining the advantages of vacuum tubes with the scalability of semiconductor-based microelectronics [18]. Briefly, an array of nanostructures was fabricated at the ends of two electric leads, featuring small gaps in-between each other. Upon excitation by laser light in a vacuum chamber, plasmon excitation led to photoemission, which allows to measure a current when voltage is applied between the two contacts, thus defining an on- and off-state. The aim is to utilise the high electron mobility in vacuum, which is around an order of magnitude greater than in silicon substrates, while preserving the integrability of semiconductor fabrication. Furthermore, higher power transfer is expected to be possible.

## 2.2. Raman spectroscopy

In Raman spectroscopy, one utilises the inelastic scattering of monochromatic light from molecules to probe for chemical composition, stress or strain, crystallinity and orientations of samples [19]. The Raman effect was theoretically predicted in 1923 by A. Smekal [20] and experimentally confirmed in 1928 by C.V. Raman [21]. In 1930, C.V. Raman was awarded the Nobel prize in physics for his work.

Today, Raman spectroscopy is a common tool in material science, biology and medical sciences, due to its non-invasive nature and applicability to a great variety of samples in different states (solid, liquid, gaseous). For example, Figure 2.1 depicts the results for a Raman investigation on HT29 colon cancer cells performed by Meister et al. [22]. The optical image (A) shows the cell and the area where Raman data was collected from. After signal collection, the peak intensities for a stretching vibration of C-H bonds (B), correlated to the cell components, and C≡O bonds (C), attributed to an organometallic molecule which was added, were evaluated and depicted in false colour. One can see that the cell component signal can be correlated to the nucleus, cell membrane and cytoplasm, while the organometallic molecule signal was mostly detected at the nucleus. Image (D) shows an overlay of the signals and images (E-G) a depth scan, respectively. Due to the non-invasive nature of Raman spectroscopy, cells can be studied over prolonged time without manipulation by probing.

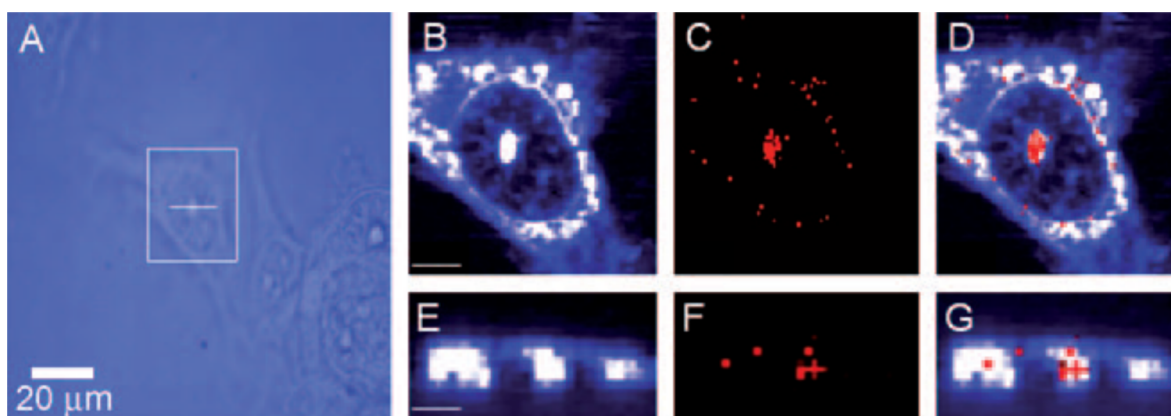


Figure 2.1.: Raman investigation on HT29 colon cancer cell. Reprinted with permission from [22]. Copyright 2010 John Wiley and Sons.

However, Raman scattering as a spectroscopy technique possesses different fundamental drawbacks. Its absolute intensity is relatively weak compared to other scattering mechanisms, which is also one of the reasons for its late discovery. For example, the Raman scattering cross section of the optical phonon in silicon at  $519\text{ cm}^{-1}$  was measured to be only around  $10^{-29}\text{ cm}^2$  [23]. The density of silicon atoms is around  $5 \times 10^{22}\text{ cm}^{-3}$ , and thus only five out of ten million photons are Raman scattered per centimetre travelled in silicon! Considering that the penetration depth of light in the visible regime for silicon is in the range of some micrometres, this

<sup>1</sup>8 atoms per  $(0.543\text{ nm})^3$  sized unit cell.

reduces the fraction of Raman scattered photons, compared to Rayleigh scattered ones, again by several orders of magnitude. Note that the reflectivity of silicon is in the range of 30 % to 50 %. Fluorescence is another inelastic scattering process, which can yield a scattering intensity several orders of magnitude higher than the Raman intensity. However, this is highly dependent on the sample material and the excitation conditions.

While today's optical components allow to sharply filter the Rayleigh signal in Raman set-ups, fluorescence can only partially be avoided by changing the excitation wavelength or optically bleaching the sample before acquiring Raman spectra.

Another drawback is the spatial resolution of Raman spectroscopy, which is typically limited to the size of the excitation spot. Using a high numerical aperture allows to achieve a lateral resolution in the range of the excitation wavelength  $\lambda$ , meaning some hundred nanometres. Likewise, with a confocal set-up a depth resolution of around  $\lambda$  can be realised.

Raman signals (Raman bands) are usually reported as function of the wavenumber  $\Delta\omega$  (Raman shift) in units of  $\text{cm}^{-1}$ .

$$\Delta\omega = \frac{1}{\lambda_0} - \frac{1}{\lambda_1}$$

Here,  $\lambda_0$  denotes the wavelength of the excitation photon and  $\lambda_1$  the wavelength of the scattered Raman photon. In this expression, the Raman shift is correlated to a distinct vibration energy  $\Delta\omega = E/(h \cdot c)$ , and thus independent of the excitation wavelength  $\lambda_0$  as it only depends on the inelastic energy transfer of the particular Raman band. However, note that dispersive Raman bands exist with  $E(\lambda_0)$ , leading to different Raman shifts for different excitation wavelengths.

Today, Raman instruments in various forms are commercially available, ranging from handheld devices for the detection of controlled substances and explosives to highly modifiable laboratory set-ups, which combine Raman spectroscopy with other techniques. Besides, several techniques to fundamentally improve the efficiency of Raman spectroscopy evolved since its discovery.

One of the further developments of conventional Raman spectroscopy is coherent anti-Stokes Raman spectroscopy (CARS), first observed in 1965 [24] and realised in 1974 [25]. In CARS, three laser beams are utilised to achieve an anti-Stokes signal several orders of magnitude higher than usual. A first pump laser is applied to transition a molecule into a virtual excited state, from which a second tunable laser facilitates the transition into the first vibrational state of the molecule. Finally, a third laser is applied probing for the conventional anti-Stokes Raman signal, which is far higher than usual due to the induced population inversion of states. The advantages of CARS are a fluorescence-free signal, due to the probing of photons of higher energy than the excitation laser. Further, the sensitivity of CARS is higher, compared to Raman, and due to the population inversion being a second-order process, the signal of the major component in the sample is dominant. Disadvantages compared to Raman are the complexity of the set-ups, the additional need for two pulsed lasers and the more difficult data evaluation and data comparison.

## 2.3. Tip-enhanced Raman spectroscopy

Another major further development of Raman spectroscopy was the addition of optical near-field concepts. Already in 1928, E.H. Synge proposed the idea of using a sub-micrometre scale aperture to geometrically confine light, and thus to increase the resolution of optical microscopy below the diffraction limit [26]. The first application of this principle in a scanning near-field optical microscope was reported in 1986 by E. Betzig et al. [27] and U. Dürig et al. [28] and transferred to Raman spectroscopy in 1995 by Smith et al. [29].

A different way to realise near-field Raman scattering was the application of apertureless SNOM, first proposed by J. Wessel in 1985 [30]. Already, plasmonics had entered the field of Raman spectroscopy in 1973 in the form of substrate-enhanced Raman spectroscopy (SERS) [31]. Briefly, plasmon excitation is utilised to generate an extremely confined and strong electrical field, amplifying the Raman signal. In contrast to SERS, this was now proposed to be performed using a single structure which can be scanned over the sample of interest.

In 2000, tip-enhanced Raman spectroscopy (TERS) was, for the first time, reported individually from three different groups [32–34]. In each case, the set-up consisted of a scanning-probe microscope (SPM) to provide a closed-loop feedback for tip positioning and topography imaging. The SPM was combined with a Raman spectrometer, utilising the Raman laser for plasmon excitation and the spectrometer path for signal collection. As a result, localised signals from thin films of molecules could be detected with high intensities.

Henceforward, interest in TERS grew rapidly and the technique spread into different scientific fields. It was reported that TERS allows to collect Raman signals from individual carbon nanotubes [35], which today is reported with a lateral resolution of 1.7 nm [36]. In biology, tip-enhanced Raman imaging of DNA for the purpose of direct sequencing was investigated [37] as well as its application for the investigation of cell surfaces [38]. In chemistry, TERS has been shown to allow for localised chemical reactions, driven by plasmon excitation [39]. On the other side, fundamental research was performed to yield a greater understanding of the underlying plasmonic processes [40, 41].

Today, several TERS set-ups are commercially available from different manufacturers which allows for a quick start into the field of near-field Raman spectroscopy. As a result, TERS is on the leap from fundamental research to routine application. Although some few probes for TERS are also commercially available, a high quality, low cost, reproducible fabrication process is still missing. Such a process would certainly accelerate the establishment of TERS in laboratories as common instrumentation and support the extension of scientific knowledge.

## 2.4. Plasmonic Nanostructures for TERS

The final section of this chapter comprises different state-of-the-art fabrication techniques and methods to create nanostructures on SPM probes suitable for TERS. Each technique offers distinct advantages and disadvantages, yet, for a batch fabrication major attributes are reproducibility, performance and scalability of the process. Note that reproducibility in terms of geometrical features can often be directly evaluated, while the reproducibility and performance of TERS enhancement is more complex to access and can often hardly be compared between different works. One of the reasons for this is a lack of standardised and common test samples, which would allow for a straightforward comparison of different probes and set-ups.

A nowadays well established technique is the **electrochemical wet etching of metal wires**, which was already used for tip fabrication in one of the firstly reported TERS experiments [34]. A metal wire, typically gold or silver, with a diameter in the range of 100  $\mu\text{m}$  to 200  $\mu\text{m}$  is placed such that it touches the surface of a wet etchant and a meniscus forms at its end. Next, a pulsed voltage is applied against a counter electrode, which facilitates etching of the metal wire. After no more electrical current is detected, typically, a sharp tip formed at the end of the wire. Figure 2.2a shows gold tips fabricated in this way for different voltages. With optimised values for etchant concentrations and voltage, tip radii in the range of some 10 nm can routinely be achieved [42, 45, 46]. Yet, although massive parallelisation of the etch step is possible, monitoring of each single tip by high magnification microscopy techniques, to verify the proper nanostructure formation, is still required. Furthermore, TERS performance is often found to vary from tip to tip, which is supposed to be also related to the geometrical differences between the tips. The grain configuration of the metal and the precise positioning of the wire on the etchant surface, as well as the positioning of the counter electrode in the bath, influence the result. In summary, this technique offers a direct way to fabricate single tips for STM or shear force feedback, while lacking the possibilities for a highly reproducible mass fabrication without the requirement of monitoring each single tip after production.

Another technique established since the beginning of TERS is the **metallisation of commercial silicon cantilevers** with gold or silver [32–34]. Briefly, a metal layer is sputter deposited or evaporated from below the beam or both, from below and from top, on standard cantilevers. Essentially, two approaches exist. One can deposit a thin layer of around 10 nm and pursue the formation of an isolated metal island at the very tip, which facilitates the excitation of LSPs for TERS. On the other hand, one can deposit thicker layers of around 40 nm and achieve a full metal coverage of the tip, which is expected to allow for SPP and/or LSP excitation at the very apex. Yet, in this case the metal thickness reduces the lateral resolution of the AFM topography image. Figure 2.2b shows typical cantilever tips after silver deposition. While this technique, together with the availability of the required infrastructure, allows for a direct access to TERS probes, reproducibility is limited, especially in the case of island formation. Often, rather than monitoring the process, the tips are directly installed in an AFM-TERS set-up and are tested for tip-enhancement of the Raman signal. Note that scalability and batch processing is possible with respect to the fabrication, yet, reproducibility of the TERS performance or any TERS

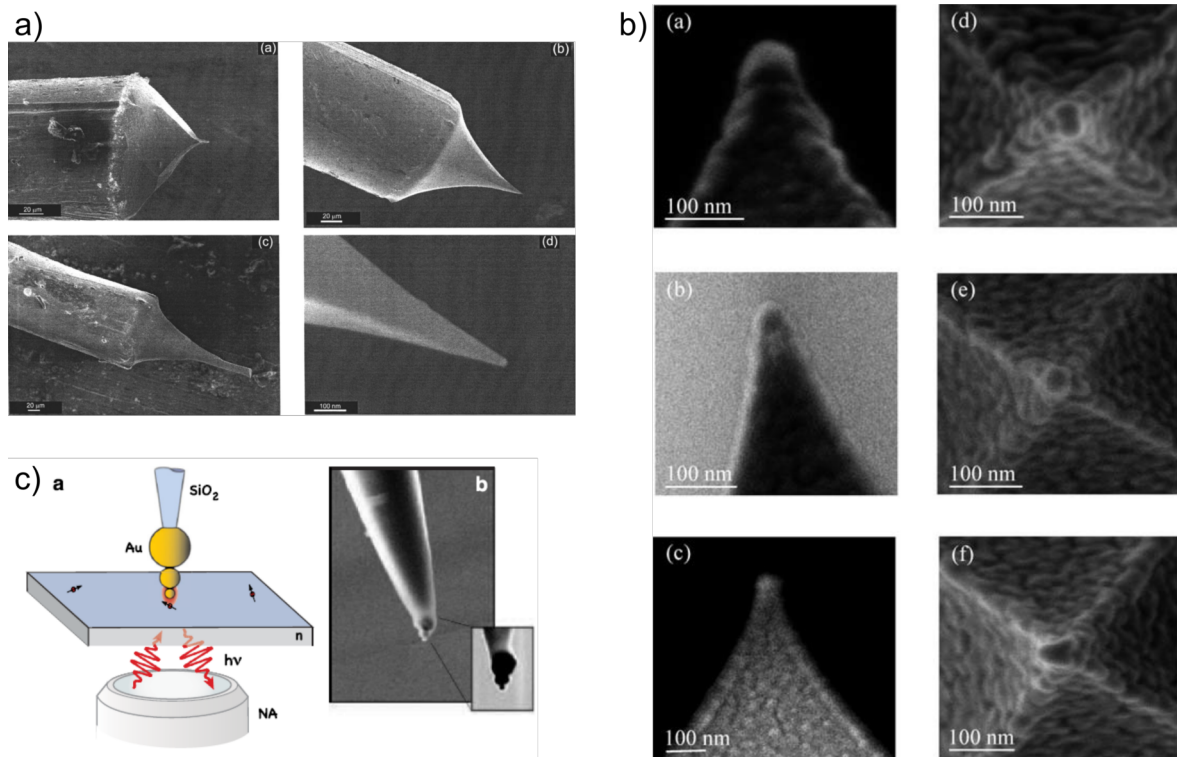


Figure 2.2.: Different TERS probes fabricated by the: a) electrochemical wet etching of metal wires. Reprinted with permission from [42]. Copyright 2008, American Vacuum Society. b) metallisation of cantilevers. Reprinted with permission from [43]. Copyright 2006, Society for Applied Spectroscopy. c) attachment of nanoparticles to a SPM tip. Reprinted Figure 1 with permission from [44]. Copyright 2012 by the American Physical Society.

performance at all is not granted. Nevertheless, nowadays metallised cantilevers are commercially available and often a certain amount of working tips, together with a distinct factor for tip-enhancement is granted by the manufacturer.

A next idea, originating from SERS substrate fabrication, is the **attachment of nanoparticles to SPM probe tips**. Earlier reported was the attachment of a single nanoparticle on the end of an optical fibre [47]. Briefly, colloidal nanoparticles are dispersed on a substrate surface and imaged by an optical fibre in shear force feedback. Due to a functionalisation of the fibre with linker molecules (e.g. polyethylenimine), it is possible to pick up a single particle by engaging the tip in direct proximity to the latter. After changing to the sample of interest, these tips could be directly employed for TERS. A more advanced process was reported ten years later, in which a stack of three differently sized nanoparticles was achieved by repeating the procedure [44]. This was reported to allow for a cascaded-enhancement of the electrical field, yielding far stronger TER signals than for a single particle. Figure 2.2c depicts a structure of this kind. Without a complex automation, these processes are not compatible to scalable batch fabrication. Quite the contrary is the case; due to the formation of the tip inside the very TERS set-up, this technique is used to

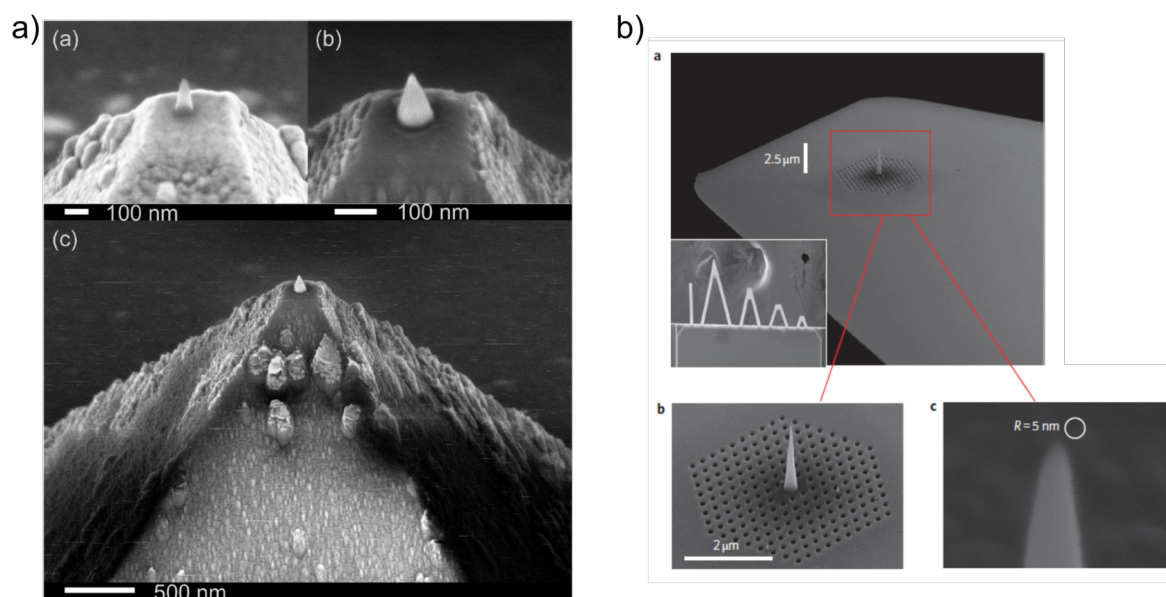


Figure 2.3.: Different TERS probes fabricated by: a) electron-beam induced mask deposition and direct ion milling. Reprinted with permission from [49]. Copyright 2011 American Chemical Society. b) nanostructuring an optical crystal and a tapered waveguide. Reprinted by permission from Macmillan Publishers Ltd: nature nanotechnology [51], copyright 2010.

generate a single tip before the planned measurement. However, note that a well-defined nanoparticle can be attached, which gives control of the resonance of the LSP utilised for TERS. As a result, reproducibility of TERS performance is expected, as long as the attachment of an isolated particle can be achieved reliably.

In the last years, more advanced techniques entered the field of TERS probe fabrication. For example, electron beam-induced deposition (EBID) combined with focused ion beam (FIB) milling allows for the **fabrication of self-designed nanostructures** directly on different kinds of SPM probes [48–50]. Briefly, a plateau is milled at the very tip of a cantilever and afterwards covered by a metal layer. Next, EBID is used to deposit a silicon oxide nanostructure as etch mask. Finally, directed ion milling is applied to create a cone like shape out of the metal layer, which then serves as nano-antenna. Figure 2.3a shows a silicon oxide nanostructure as etch mask (top left), the resulting gold nano-antenna after etching (top right) and an overview image of the TERS probe (bottom). Again, due to the complexity of such processes and the one-by-one fabrication a batch manufacturing is not possible. However, these techniques offer many degrees of freedom, which one can use to tune the plasmonic response of the tip. The choice of metal, of lateral dimensions and height, of the precise shape, of the orientation and the SPM probe type (optical fibre, cantilever) make such a process perfectly suited for the fabrication of tailored TERS probes.

Highly related to the previous is the combination of nanostructuring techniques with the design of **photonic crystals and tapered waveguides** on SPM tips. Briefly, nanostructuring is applied to unite different concepts to an optimised plasmonic excitation. For example, the FIB structuring of a waveguide on a TERS tip, matching

the excitation light was reported to facilitate the generation of SPPs, and thus the TERS performance of the tip [52]. Going further, it was reported that the structuring of a photonic crystal by FIB milling allows for an even more efficient coupling of the laser source, exciting SPPs along a defined waveguide structure [51]. Figure 2.3b shows images of a plasmonic crystal, consisting of periodic cavities, and a tapered waveguide in the center. These were structured on a cantilever, suitable for AFM feedback. Additional to the optimised excitation of SPPs, other advantages were reported. For example, due to the spatial separation of plasmon excitation and the TERS hotspot in the micron range, lower background noise was expected, leading to a higher signal-to-noise ratio. Once more, batch fabrication of such structures for a widespread application is complex and, most likely, not the driving intention for this development.

From the previous discussion one can deduce a kind of conservation of complexity. Simpler, batch fabrication compatible processes lead to the fabrication of less controllable nanostructures, which then require individual monitoring or are not reliable enough for distribution. On the other hand, complex techniques allow for a defined structure creation, which however is too time-consuming, not parallelisable or too expensive for batch fabrication. A technique which is reported to balance both sides is **template stripping**. Here, distinct kinds of nanostructures, suitable for TERS, can be fabricated in massive parallelisation with high reliability [53, 54]. Since this is a main topic of the work at hand, a process description is omitted here and given at an adequate point later. Figure 2.4 shows images of near-identical gold structures fabricated in parallel (top) and an individual structure released for TERS application (bottom). With a stable parallel fabrication of numerous near-identical metal structures, featuring a radius of curvature of some ten nanometres at the tip, and a batch processing compatible release method, this technique could allow for reliable distribution of TERS probes for STM and shear force feedback. Furthermore, integrating the process into cantilever fabrication would also permit the batch manufacturing of TERS probes for contact and non-contact AFM feedback.

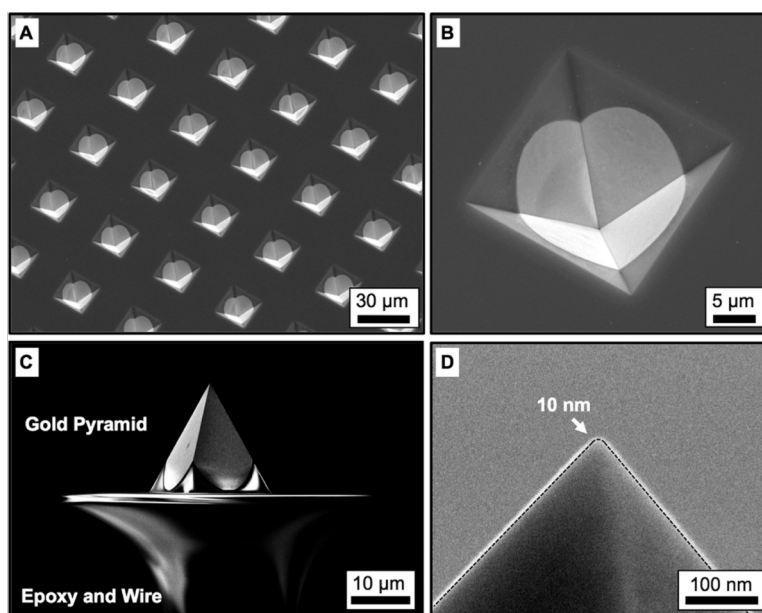


Figure 2.4.: A TERS probe fabricated by template stripping of a gold structure from a pyramidal cavity. Reprinted with permission from [53]. Copyright 2012 American Chemical Society.

## 3. Basic Principles

This chapter covers the physical principles and mathematical concepts of scanning tunnelling microscopy, Raman scattering, plasmonics, a model for tip-enhanced Raman spectroscopy and the finite element method. In the beginning of each chapter, the relevant literature is mentioned that was followed during the derivation.

### 3.1. Scanning tunnelling microscopy

A brief introduction to the principles of scanning tunnelling microscopy (STM) is provided in this section, following the approach of Julian Chen [55].

It is known from basic quantum mechanics that in one dimension a free particle of energy  $E$  and mass  $m$  possesses a non-vanishing probability to be found in a bordering interval of constant potential  $V$  at  $x > 0$ , where  $V > E$  holds true. This is not allowed in classical mechanics and is represented by an exponential decaying wave function inside the potential area.

$$\Psi(x) = \Psi(0) \cdot \exp(-\kappa x)$$

Here,  $\Psi(0)$  denotes the wave function at the border of the potential and  $\kappa$  is given by

$$\kappa = \frac{\sqrt{2m(V - E)}}{\hbar} .$$

If the interval of constant potential  $V$  is finite in size, there is a probability to find the particle on the other side. This effect is known as tunnelling and utilised in STM.

Figure 3.1a shows a schematic of a one-dimensional metal-vacuum-metal tunnel junction in terms of electron energy levels. For simplification, both metals are assumed to be the same material and thus, feature the same work function  $\Phi$ . The variable  $\Phi$  denotes the energy which is needed to remove an electron from the bulk material to the vacuum level.  $\Phi$  is not only material dependant, but also changes with crystal orientation and surface modifications. Electron states up to the Fermi energy  $E_F$  are occupied on both sides, temperature influence is neglected. Furthermore, a negative bias voltage  $U_{bias}$  is applied to the tip, raising the Fermi energy up by  $eU_{bias}$ , where  $e$  is the electron charge. Thus, a net tunnelling from tip to sample is facilitated and a tunnel current can be calculated using the transmission coefficient.

$$I(z) = I_0 \cdot \exp\left(-2 \frac{\sqrt{2m_e \Phi}}{\hbar} z\right) \quad (3.1)$$

Here,  $I_0$  denotes the current when the tip is at the sample surface and  $m_e$  is the electron mass. Since the absolute sample-tip distance is not easily accessible during

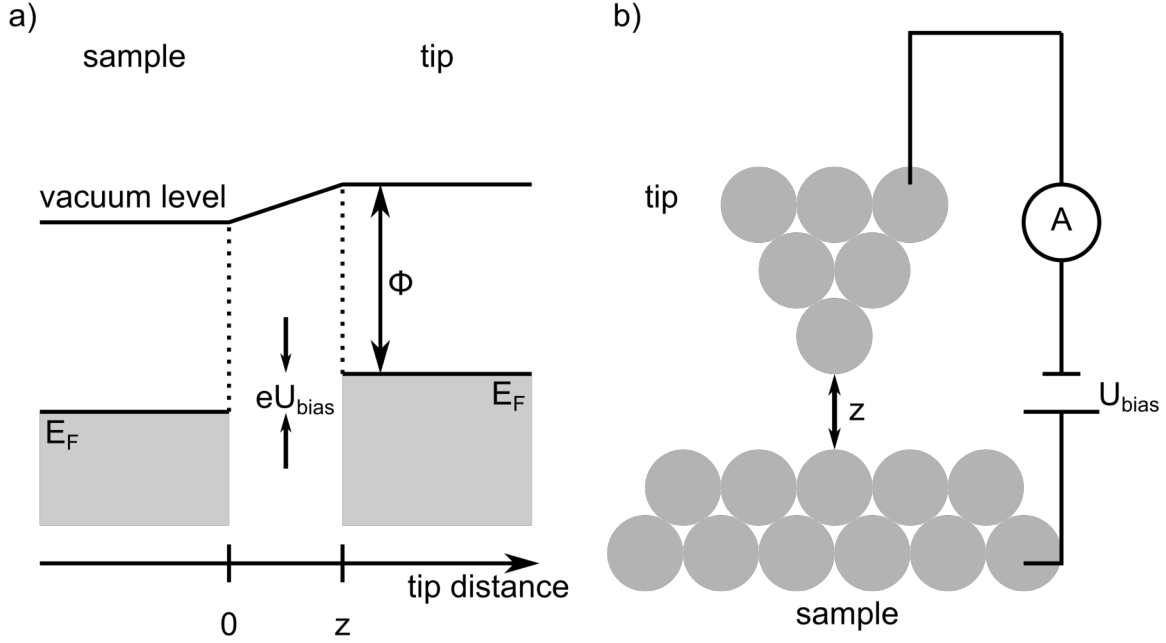


Figure 3.1.: a) Schematic of the tunnel junction in STM. b) Schematic of a STM tip-sample gap with bias and control loop. Figures adapted from [55].

experiments, one can achieve another expression by dividing equation 3.1 by itself for another value of  $z$ , which is the tip-sample distance at the set-point of the closed loop feedback.

$$I(z) = I_{set} \cdot \exp\left(-2\frac{\sqrt{2m_e\Phi}}{\hbar}(z - z_{set})\right) \quad (3.2)$$

In this equation,  $I_{set}$  and  $z_{set}$  denote the tunnel current and the distance at the set-point of the closed loop feedback, respectively. This expression can be used to determine the vacuum energy by measuring  $I(z)$  curves experimentally and fitting for the variable  $\Phi$ .

Figure 3.1b shows a schematic of an ideal STM measurement. A single atom at the very tip of a probe is scanned over a flat surface with closed loop feedback, using the tunnel current at a fixed  $U_{bias}$  to control the tip-sample distance. From equation 3.1, the sensitivity of the tunnel current for a variation of  $z$  can be deduced. Vacuum energies of metals are usually in the range of some eV, e.g. for gold 5.4 eV and for tungsten 4.8 eV. Using these numbers, the constant factor in the exponent

$$\kappa = \frac{\sqrt{2m_e\Phi}}{\hbar}$$

can be calculated and one obtains values between  $10 \text{ nm}^{-1}$  to  $12 \text{ nm}^{-1}$ . Thus, for metals a variation of the tip-sample distance  $\Delta z$  of 0.1 nm yields an increase or decrease of around an order of magnitude in tunnelling current! A reason STM allows for the imaging of individual atoms is this extreme dependency of the tunnel current on the tip-sample distance.

## 3.2. Raman scattering

An overview of the basic principles of Raman scattering is presented in this section, following the approach of Ferraro et al. [56].

The interaction of electromagnetic waves with matter leads to absorption and scattering. Main scattering mechanisms are Rayleigh scattering, Raman scattering and fluorescence (including phosphorescence). In a classical model, the electric field  $\vec{E}$  of a planar, linearly polarised electromagnetic wave at a fixed point can be described by

$$\vec{E} = \vec{E}_0 \cdot \cos(\omega_0 t) \quad . \quad (3.3)$$

Here,  $\vec{E}_0$  denotes the field amplitude,  $\omega_0$  denotes the angular frequency and  $t$  the time. The angular frequency is connected to the frequency  $f_0$  and the wavelength  $\lambda_0$  as usual by the expression

$$\omega_0 = 2\pi \cdot f_0 = 2\pi \cdot \frac{c}{\lambda_0} \quad (3.4)$$

using the speed of light in vacuum  $c$ . If a molecule is excited by an electrical field, an electric dipole moment  $\vec{P}$  is induced, which can be described by using the polarisability  $\alpha$  of the molecule.

$$\vec{P} = \alpha \cdot \vec{E} \quad (3.5)$$

In the simple case of a Raman active, diatomic molecule, a vibration around the equilibrium distance  $q_m$  between the atoms with an angular frequency  $\omega_m$  can be excited.

$$q = q_m \cdot \cos(\omega_m t) \quad (3.6)$$

Now, the fundamental requirement for Raman activity is the premise that the polarisability  $\alpha$  of the molecule is dependent on the atom distance  $q$ . This is equivalent to a non-vanishing linear coefficient in the Taylor series of  $\alpha(q)$ .

$$\alpha(q) = \alpha_0 + \left( \frac{\partial \alpha}{\partial q} \right)_{q_m} \cdot q + \mathcal{O}(q^2) \quad (3.7)$$

Substituting equations 3.3, 3.6 and 3.7 in equation 3.5 yields an expression for the dipole moment as function of  $t$ .

$$\begin{aligned} \vec{P}(t) &= \left( \alpha_0 + \left( \frac{\partial \alpha}{\partial q} \right)_{q_m} \cdot q_m \cos(\omega_m t) \right) \cdot \vec{E}_0 \cos(\omega_0 t) \\ &= \alpha_0 \cdot \vec{E}_0 \cos(\omega_0 t) + \left( \frac{\partial \alpha}{\partial q} \right)_{q_m} \cdot q_m \cdot \vec{E}_0 \cos(\omega_m t) \cos(\omega_0 t) \\ &= \alpha_0 \cdot \vec{E}_0 \cos(\omega_0 t) + \frac{1}{2} \left( \frac{\partial \alpha}{\partial q} \right)_{q_m} \cdot q_m \cdot \vec{E}_0 \cos((\omega_0 - \omega_m) \cdot t) \\ &\quad + \frac{1}{2} \left( \frac{\partial \alpha}{\partial q} \right)_{q_m} \cdot q_m \cdot \vec{E}_0 \cos((\omega_0 + \omega_m) \cdot t) \end{aligned} \quad (3.8)$$

As a result, in equation 3.8 a superposition of dipole oscillations of three different frequencies is found, which can be attributed to different scattering processes. The

first term describes Rayleigh scattering or reflection. An electromagnetic wave with the same frequency as the excitation is emitted. The second term correlates to Raman scattering of an electromagnetic wave with an angular frequency  $\omega_0 - \omega_m$ , also called Stokes scattering. The last term correlates to Raman scattering with an angular frequency of  $\omega_0 + \omega_m$  or anti-Stokes scattering.

Note that in a general description  $\alpha$  becomes a tensor and attributes for the directional dependency of the polarisability. Furthermore, while the classical calculation allows for a direct access to the concept of Raman scattering, several properties are not included in the model, e.g. the experimentally observed difference in intensities for Stokes and anti-Stokes scattering.

In a quantum mechanical picture, Raman scattering can be discussed in terms of energy levels, occupation probabilities and transitions. Figure 3.2 shows the typical visualisation for different scattering processes on molecules. The black lines depict vibrational levels of the electronic ground state (bottom) and an excited electronic state (top). Note that the difference between vibrational levels and electronic states is far higher than depicted and that additional rotational energy levels are present between the vibrational levels. In **Rayleigh** scattering a photon of angular frequency  $\omega_0$  is absorbed and the molecule is excited into a virtual state (dashed line). With a high probability, the molecule relaxes back into the ground state, emitting a photon back with the same angular frequency  $\omega_0$ .

In Stokes Raman scattering (**S Raman**), a photon of angular frequency  $\omega_0$  is absorbed and the molecule is excited into a virtual state. Here, a relaxation of the molecule into a vibrational state occurs and a photon of the reduced angular frequency  $\omega_0 - \omega_m$  is emitted, where  $\Delta E = \hbar\omega_m$  denotes the energy of the excited vibration. Likewise, in anti-Stokes Raman scattering (**A-S Raman**) the molecule is excited not from the ground state, but from an already present vibrational state into a virtual state. Here, relaxation into the ground state occurs by emitting a photon of the angular frequency  $\omega_0 + \omega_m$ , probing the same energy difference, between ground state and vibrational state, as before.

A special case of these two processes described before is resonant Raman scattering (**S & A-S resonant**). Here, an excited electronic state of the molecule matches the excitation energy of the incoming photon. This allows for a more efficient absorption, and thus an increased Raman scattering.

Finally, **fluorescence** is the emission of a broad spectrum of photons of different angular frequencies. In this case, the absorbed photon energy is enough to transition the molecule into the region of an excited electronic state. Then, radiationless relaxation into the vibrational ground state occurs (dashed arrow). From there, radiative transitions into different vibrational states of the electronic ground state can take place. The result is the emission of photons of different energies. In Raman spectroscopy, fluorescence is often undesired and bleaching or confocality is utilised to minimise its signal contribution.

In general, complex molecules feature several atomic bonds and each of them allows for different vibrational modes. Further, some of these modes are Raman active, while others are not. In combination, this often leads to a unique Raman fingerprint for a distinct molecule, which allows to identify an unknown material composition. Also, the occupation probability of the first vibrational state is tem-

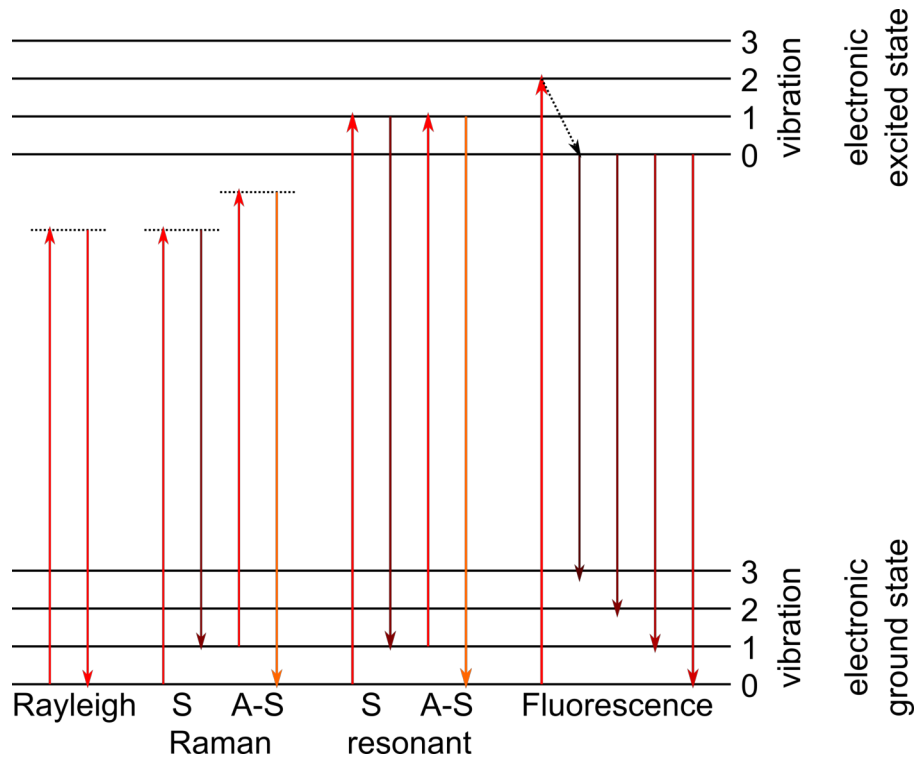


Figure 3.2.: Schematic representation of different photon scattering processes correlated to molecular energy levels and transitions. Figure adapted from [56]

perature dependent, which allows to utilise the relative intensity between a certain Stokes and anti-Stokes band for temperature determination [57].

### 3.3. Plasmonics

A brief introduction to the physics of plasmons is presented following Maier [58]. Briefly, the first section describes plasmons at a metal-insulator interface while the second section covers the formulation of localised plasmons in a metallic sphere. Both of these represent solutions to the macroscopic Maxwell's equations, which constitute the foundations of electromagnetism.

#### Surface plasmon polaritons

As the name already suggests, surface plasmon polaritons (SPP) are quantised electromagnetic waves excited at a metal-dielectric interface. Starting from Maxwell's equations, the wave equation of the electrical field can be deduced

$$\nabla \times \nabla \times \vec{E}(\vec{r}, t) = -\mu_0 \frac{\partial^2 \vec{D}(\vec{r}, t)}{\partial^2 t} \quad (3.9)$$

Next, one assumes a negligible spatial variation of the dielectric function  $\epsilon(\vec{r})$  and a harmonic electrical wave of the form

$$\vec{E}(\vec{r}, t) = \vec{E}(\vec{r}) \cdot \exp(-i\omega t)$$

as solution. This allows to simplify equation 3.9 to the Helmholtz equation, where  $k_0$  is the wave vector in vacuum.

$$\nabla^2 \vec{E} + k_0^2 \epsilon \vec{E} = 0 \quad (3.10)$$

Next, the dielectric function is limited to one dimension by assuming an interface in the  $x$ - $y$ -plane with  $\epsilon(z)$  being only dependant on the height. A cross section of this situation is depicted in Figure 3.3a. The  $x$ -direction is chosen according to the propagation direction of the wave, while the metal-air interface is located at  $z = 0$ . Furthermore, due to homogeneity in  $y$ -direction,  $\vec{E}$  is not dependant on  $y$ . Thus, the spatial part of the wave function transforms to

$$\vec{E}(x, y, z) = \vec{E}(z) \cdot \exp(i\beta x)$$

where  $\beta = k_x$  denotes the propagation constant. With this modification, the Helmholtz equation can be evaluated to

$$\frac{\partial^2 \vec{E}}{\partial^2 z} + (k_0^2 \epsilon - \beta^2) \vec{E} = 0 \quad (3.11)$$

which forms the fundamental equation for wave propagation at interfaces. A similar equation can be derived for the magnetic field  $\vec{H}$ . Further analysis is performed by using the electromagnetic curl equations, which yield a set of six equations and allow to obtain information about the dispersion relation and the spatial field profile in  $z$ -direction. Three of these equations describe propagating transverse-magnetic (TM, p-polarisation) modes, while the remaining three are correlated to transverse-electric (TE, s-polarisation) modes.

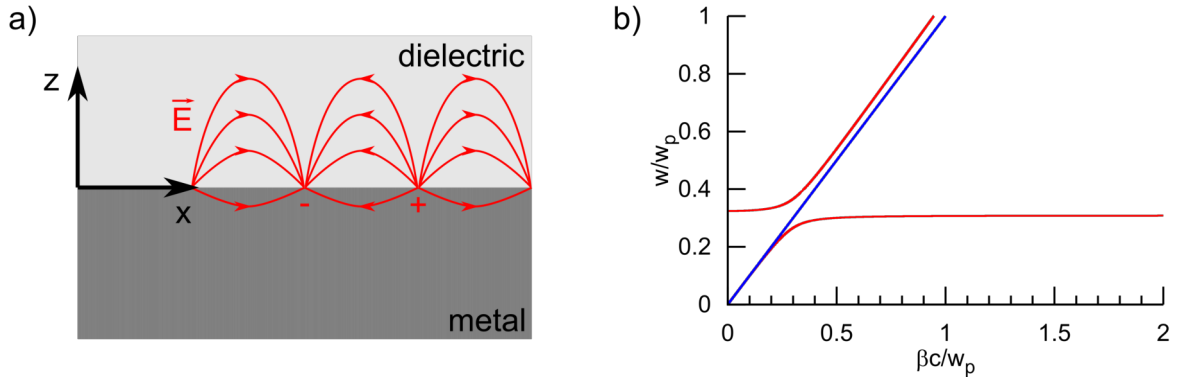


Figure 3.3.: a) Schematic of a metal-dielectric interface with the electrical field for a TM mode. Figure adapted from [58]. b) Dispersion relation of SPPs for a gold-vacuum interface, calculated using a Drude function.

In the case of the interface depicted in Figure 3.3a, the dielectric material at  $z > 0$  is described by the constant dielectric function  $\epsilon_2$  of vacuum with a positive real part. The metal volume at  $z < 0$  however features a frequency dependent dielectric function with  $\text{Re}(\epsilon_1) < 0$  (which defines its metallic character). Using the equations for the TM mode, one finds solutions for  $E_x(z)$ ,  $E_z(z)$  and  $H_y(z)$  in both materials. The electrical field and net charges in the metal are depicted in red. To satisfy the boundary conditions for continuity, one finds an expression which links the wave vectors perpendicular to the interface  $k_{z,1}$ ,  $k_{z,2}$  with the dielectric permittivity.

$$\frac{k_{z,2}}{k_{z,1}} = -\frac{\epsilon_2}{\epsilon_1}$$

The solution demands one of the dielectric functions to yield a negative value. This limits the existence of the solution to interfaces of materials, which feature dielectric functions of different signs, e.g. conductors and insulators.

With the wave equation 3.11 one finds a relation for the propagation constant  $\beta$  and the dielectric functions.

$$\beta = k_0 \sqrt{\frac{\epsilon_1 \epsilon_2}{\epsilon_1 + \epsilon_2}}$$

This equation represents the dispersion relation of SPPs.

Figure 3.3b shows a graph of the real part of the dispersion relation for SPPs (red lines), which were calculated using Drude's function for an air-gold interface and parameters from [59]. The fact that there is no crossing with the respective light line (blue line) explains why an excitation of SPPs requires special techniques. To be precise, an imaginary part of  $\beta$  is also missing, while the light line is completely real. However, this is found to be small in the case of gold. The coupling of light to SPPs, which means to match the wave vector of the excitation to the SPP's wave vector, can be achieved with a prism (Otto- or Kretschmann configuration [12, 13]), by utilising a grating structure, exploiting surface roughness of the metal or using a focused beam.

Finally, note that a solution for a TE mode yields only the trivial solution 0 when applying the boundary conditions.

## Localised surface plasmons

The previous chapter covered the excitation of propagating electromagnetic waves at a metal-insulator interface. Here, the excitation of localised surface plasmons (LSP) is described. Metal particles, with sizes below the wavelength of an external electromagnetic wave (e.g. visible light) can show a resonant behaviour upon excitation. Then, an oscillation of electric charges is driven and strong electrical fields are generated inside and in proximity of the particle surface. In contrast to SPPs, LSPs can be excited without wave vector matching, since the curved surface of the particle itself provides an effective restoring force, allowing for oscillations.

The properties of LSPs on a nano-particle can be investigated by solving the Laplace equation for the potential  $\Phi(\vec{r})$

$$\nabla^2\Phi = 0$$

from which the electrical field can be calculated. For a physical model, a metal particle in the shape of a perfect sphere, located at the origin of the coordinate system, as depicted in Figure 3.4, is investigated. For the radius  $\rho$  of the particle, it is assumed that  $\rho \ll \lambda$  holds true. This allows to consider the phase of the electrical field to be constant over the size of particle, which separates the harmonic time-dependency of the field in the problem. Thus, the Laplace equation can be solved for a constant field and the harmonic oscillation of the latter can be included at the end. The driving electrical field is oriented in  $z$ -direction  $\vec{E} = E_0\hat{z}$ .

The metal features a dielectric function  $\epsilon_1(\omega)$  and the surrounding medium a dielectric constant  $\epsilon_2$ . The spatial vector  $\vec{r}$  and the polar angle  $\theta$  are depicted accordingly.

The azimuthal symmetry of the model allows for a separation of variables, leading to a linear combination of Legendre polynomials  $P_l(\cos\theta)$  as solution. Another consequence of the symmetry is, that  $\Phi$  is only a function of  $|\vec{r}|$  and  $\theta$ . Thus, two separate solutions for the potential inside the sphere volume  $\Phi_{in}$  and outside the sphere volume  $\Phi_{out}$  can be expressed by

$$\begin{aligned}\Phi_{in}(r, \theta) &= \sum_{l=0}^{\infty} A_l \cdot r^l \cdot P_l(\cos\theta) \\ \Phi_{out}(r, \theta) &= \sum_{l=0}^{\infty} \left( B_l \cdot r^l + C_l \cdot r^{-(l+1)} \right) P_l(\cos\theta)\end{aligned}$$

The coefficients can be determined by evaluating the boundary conditions, namely that  $\Phi_{out}(r \rightarrow \infty) = -E_0z$  holds true and that continuity for the tangential and normal electrical field component on the sphere surface at  $r = \rho$  is preserved. Finally, one arrives at the following solution:

$$\Phi_{in}(r, \theta) = -\frac{3\epsilon_2}{\epsilon_1 + 2\epsilon_2} E_0 r \cos\theta \quad (3.12)$$

$$\Phi_{out}(r, \theta) = -E_0 \cdot r \cos\theta + \frac{\epsilon_1 - \epsilon_2}{\epsilon_1 + 2\epsilon_2} E_0 \cdot \rho^3 \frac{\cos\theta}{r^2} \quad (3.13)$$

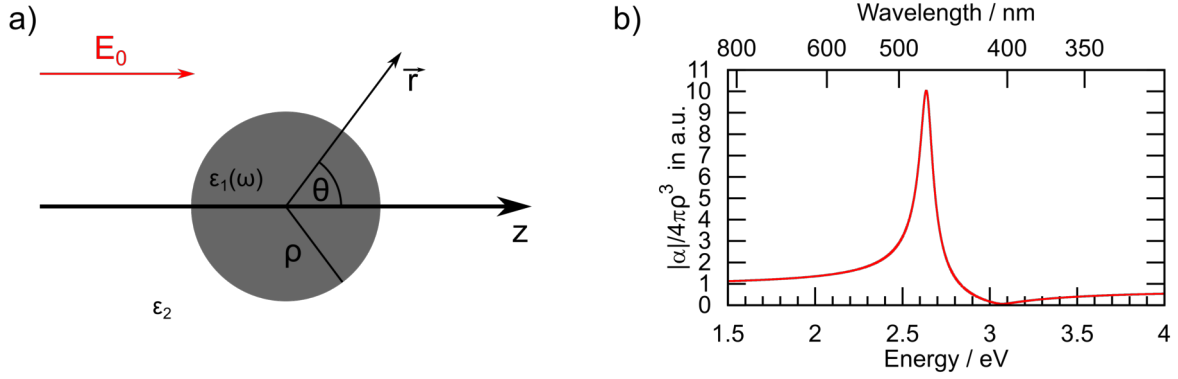


Figure 3.4.: Schematic of a metal particle in an external electrical field. Figure adapted from [58]. b) Calculated modulus of the polarisability of a nano-particle using a Drude function and parameters for gold from [59]

The potential outside the sphere volume (equation 3.13) can be interpreted as a combination of the potential of an external electrical field and the potential of a point dipole with dipole moment  $\vec{p}$  located at the position of the sphere.

$$\Phi_{out}(r, \theta) = -E_0 \cdot r \cos \theta + \frac{\vec{p} \cdot \vec{r}}{4\pi\epsilon_0\epsilon_2 r^3}$$

$$\vec{p} = 4\pi\epsilon_0\epsilon_2\rho^3 \frac{\epsilon_1 - \epsilon_2}{\epsilon_1 + 2\epsilon_2} E_0 \hat{z}$$

Note that the dipole moment increases linearly with  $E_0$ , which is reasonable since the electrical field induces the dipole inside the metal particle. By introducing the polarisability  $\alpha$  of this dipole, defined by

$$\vec{p} = \epsilon_0\epsilon_2\alpha E_0 \hat{z}$$

one finds a final expression, which can be further investigated.

$$\alpha = 4\pi\rho^3 \frac{\epsilon_1 - \epsilon_2}{\epsilon_1 + 2\epsilon_2}$$

Figure 3.4b shows a graph of the absolute value of  $\alpha(\omega)$  for a gold particle in vacuum. The plot was generated by using a Drude dielectric function for  $\epsilon_1(\omega)$  with parameters from Oubre et.al., namely  $\epsilon_\infty = 9.5$ ,  $\omega_p = 8.95$  eV and  $\gamma = 0.07$  eV [59]. As one can see in the plot and already deduce from the formula, a resonance condition for  $\text{Re}(\epsilon_1) = -2\epsilon_2$  exists. However, the absolute value of  $\alpha$  does not diverge, due to the imaginary part of  $\epsilon_1$ , which limits the denominator to a finite value.

The electrical field inside the particle  $\vec{E}_{in}$  can be evaluated by differentiating equation 3.12, which yields the following expression.

$$\vec{E}_{in} = \frac{3\epsilon_2}{\epsilon_1 + 2\epsilon_2} \vec{E} \quad (3.14)$$

Note that the field inside the particle can be larger in magnitude than the exciting external field.

### 3.4. Tip-enhanced Raman scattering

This section comprises a mathematical description of the Raman enhancement factor, which is derived following Wokaun [60]. Afterwards, a mathematical formulation of the tip-sample dependency of the TER signal is given, following the work of Pettinger et al. [61].

Firstly, Raman scattering from a Raman active molecule adsorbed to a metal nanoparticle is investigated. Furthermore, the harmonic oscillation with frequency  $\omega_0$  of the external electrical field is now included. As shown in the previous section, the dipole moment  $\vec{p}(\omega)$  of the particle is proportional to the external electrical field  $\vec{E}(\omega_0)$  and the polarisability  $\alpha(\omega_0)$ . At resonance, the frequency of the oscillation of the dipole moment is also  $\omega_0$ .

$$\vec{p}(\omega_0) \propto \alpha(\omega_0) \vec{E}(\omega_0)$$

This dipole produces an electrical field (which is proportional to its dipole moment  $\vec{p}(\omega)$ ) in the adsorbed molecule. The field leads to a polarisation of the molecule itself and induces the dipole moment of the molecule  $\vec{\mu}$ . Due to the Raman activity of the molecule, its dipole moment includes at least one component  $\vec{\mu}_R$  correlated to the respective Raman frequency  $\omega_R$ .

$$\vec{\mu}_R(\omega_R) \propto \sigma_R \cdot \vec{p}(\omega_0)$$

Here,  $\sigma_R$  denotes the phenomenological Raman polarisability.

This dipole moment, again, produces an electrical field  $\vec{E}_R \propto \vec{\mu}_R$ , which is the Raman signal. Furthermore, it can also utilise the nanoparticle as an antenna. In fact, this process is completely symmetrical to the excitation deduced in the section before. Thus, a dipole moment  $\vec{p}_R$  inside the particle is excited proportional to  $\alpha(\omega_R)$  and  $\vec{E}_R(\omega_R)$ .

$$\begin{aligned} \vec{p}_R &\propto \alpha(\omega_R) \cdot \vec{E}_R \\ &\propto \alpha(\omega_R) \cdot \vec{\mu}_R \\ &\propto \sigma_R \cdot \alpha(\omega_R) \cdot \alpha(\omega_0) \cdot \vec{E}(\omega_0) \end{aligned}$$

Calculating the radiated power of the Raman signal by integrating over the full angle, one finds a relation for the intensity scattered in the case of the molecule being adsorbed to the antenna dipole,  $I(\omega_R)$ , and the intensity scattered by an isolated molecule  $I_{iso}(\omega_R)$ .

$$I(\omega_R) = |f(\omega_R)|^2 \cdot |f(\omega_0)|^2 \cdot I_{iso}(\omega_R)$$

Here,  $f(\omega)$  denotes the enhancement factor due to the particle, which is proportional to  $\alpha(\omega)$ . If the external field and the plasmonic oscillation are resonant to the Raman band, one arrives at an enhancement factor of  $|f(\omega_R)|^4$ . This is the famous prediction for an increase of Raman intensity by the fourth power of the field enhancement when utilising near-field scattering.

Next, the dependency of the TER signal as a function of the tip-sample distance is investigated, using a model as depicted in Figure 3.5. A gold tip, considered as a metal sphere with radius  $R_s$ , and thus treated as a point dipole, is located above a gold surface. The centre of the sphere is located at a distance  $z_0$  above the surface. The origin of the coordinate system is placed below the sphere at the sample surface, marked by a black ring. Note the radial symmetry of the model. The tip is excited by a linearly polarised electrical field  $E$  depicted in red with the respective  $k$ -vector.

To calculate the electrical field, an expression for the electrical potential  $\Phi$  is firstly searched for. Here, the total potential can be separated in a term contributing for the point dipole due to charge separation inside the sphere and a term contributing for the point dipole of the induced mirror charges inside the metal sample. This leads to the following expression, where  $d$  denotes the distance of charge separation and  $e$  the separated charges.

$$\begin{aligned}\Phi &= \Phi_{dipole} + \Phi_{image} \\ &= \left( \frac{e}{\sqrt{x^2 + y^2 + (z_0 - z - d/2)^2}} - \frac{e}{\sqrt{x^2 + y^2 + (z_0 - z + d/2)^2}} \right) \\ &\quad + \left( -\frac{e}{\sqrt{x^2 + y^2 + (z_0 + z - d/2)^2}} + \frac{e}{\sqrt{x^2 + y^2 + (z_0 + z + d/2)^2}} \right)\end{aligned}$$

Evaluating the normal electrical field component by differentiating for  $z$  on the surface  $z = 0$  and normalizing for the external field yields an expression for the position-dependent enhancement factor  $f(x, y)$  on the sample surface.

$$f(x, y) \propto \left( \frac{2z_0 - d}{(x^2 + y^2 + (z_0 - d/2)^2)^{3/2}} - \frac{2z_0 + d}{(x^2 + y^2 + (z_0 + d/2)^2)^{3/2}} \right)$$

As deduced in the section before, the total enhancement of the Raman intensity is proportional to  $f^4$ , if excitation and scattering is treated symmetrically. Thus, for further evaluation of the TERS intensity  $I_{TERS}$ , the enhancement factor to the fourth is integrated over the sample surface.

$$I_{TERS} \propto \int_0^\infty \int_0^\infty f(x, y)^4 dx dy$$

The integral can be evaluated by using a series expansion of  $f(x, y)$  until the fourth order in  $d$ , yielding the  $z$ -dependency for the TERS intensity.

$$I_{TERS} \propto \frac{1}{z_0^{10}} \cdot d^4$$

Substituting  $z_0$  for  $R_s + z$  gives the TERS intensity as function of the tip-sample distance. However, the absolute distance is often not directly accessible in STM measurements. Thus, normalising the TERS intensity for an arbitrary distance  $z$  to the TERS intensity at the distance of the tunnel current set-point  $z_{set}$  yields the final expression.

$$I_{TERS}^{norm} = \frac{I_{TERS}(z)}{I_{TERS}(z_{set})} = \frac{(R + z_{set})^{10}}{(R + z)^{10}} \quad (3.15)$$

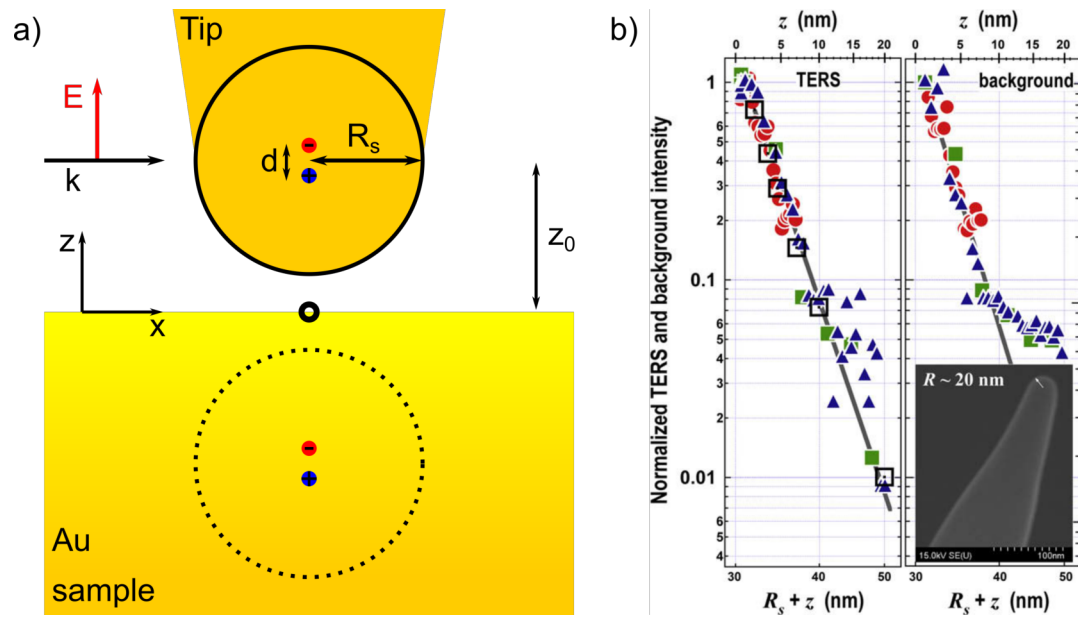


Figure 3.5.: a) Model to calculate the dependency of the TERS intensity from the tip-sample distance, adapted from [61]. b) Graph of the  $z^{-10}$  fit to Raman data and background signal. Note that the Raman signal follows the fit over the whole range, while the background signal converges against a constant noise intensity. Reprinted from [61], Copyright 2009, with permission from Elsevier.

This relation was found to describe experimental data and simulation results reasonably well. Thus, it is also used at a later point to fit experimental data acquired from tip-enhanced luminescence measurements. Here, an additional term is added to equation 3.15 ( $+I_{noise}$ ), accounting for the measured noise at maximum separation. However, note that two degrees of freedom exist, which allow for good fits if both variables are floated. Thus, one can either fix the set point distance  $z_{set}$  to an approximate value, typically for STM in the range of 1 nm, or one can fix the tip radius, which can be measured by SEM. Figure 3.5 shows fits to data of tip-enhanced Raman signals and background signals acquired during experiments. Here, the tip radius was evaluated in advance by SEM imaging.

### 3.5. Finite element method

The final section comprises a brief overview over the basic principles of finite element simulations. Here, Zienkiewicz et al. is followed [62].

The numerical calculation of differential equations while simultaneously satisfying certain boundary conditions provides a direct access to physical solutions, without the need of solving the problem analytically. The finite element method (FEM) follows a pragmatic approach to solve the problem at hand. Firstly, the continuous volume is separated into finite elements (mesh), as the name suggests. These elements are connected by a finite number of nodes. The differential equations are then solved on each element under the boundary condition of continuity to the neighbouring elements at the node points. Finally, this process is iterated until a convergence criterion is met, e.g. a function calculating the mismatch with the solution before yields values below a certain threshold.

In this work, numerical solutions of the wave equation for a finite volume with an external electrical field and a metal structure inside were calculated. The unknown function is the electrical field  $\vec{E}(\vec{r})$ .

In a general mathematical formulation, let  $\vec{u}$  be a set of unknown functions and let  $A_i$  be a set of differential operators, so that

$$\vec{A}(\vec{u}) = \begin{pmatrix} A_1(\vec{u}) \\ A_2(\vec{u}) \\ \dots \\ \dots \end{pmatrix} = 0 \quad (3.16)$$

holds in a domain  $\Omega$ , which can be an area or a volume. Furthermore, it is required that a set of boundary conditions  $B_i$  is met on the boundary  $\Gamma$  of  $\Omega$  by the solution, according to:

$$\vec{B}(\vec{u}) = \begin{pmatrix} B_1(\vec{u}) \\ B_2(\vec{u}) \\ \dots \\ \dots \end{pmatrix} = 0. \quad (3.17)$$

In the finite element calculation, the unknown functions  $\vec{u}$  are now approximated by functions  $\vec{\eta}$ . Each function  $\eta_i$  is composed of a linear combination of shape functions  $N_\alpha^i$  and coefficients  $\tilde{\eta}_\alpha^i$

$$u_i \approx \eta_i = \sum_{\alpha=1}^n \tilde{\eta}_\alpha^i N_\alpha^i \quad (3.18)$$

The shape functions and the discretisation of space can be freely chosen.

Next, the *weak statement* is formulated by introducing test functions  $\vec{v}$  in the volume  $\Omega$  and  $\vec{\hat{v}}$  on  $\Gamma$ . Multiplication with equations 3.16 and 3.17 yields the following expression after integration.

$$\int_{\Omega} \vec{v}^T \vec{A}(\vec{u}) \, d\Omega + \int_{\Gamma} \vec{\hat{v}}^T \vec{B}(\vec{u}) \, d\Gamma = 0 \quad (3.19)$$

The functions  $\vec{v}$  and  $\vec{\hat{v}}$  are usually limited to bounded functions, avoiding a divergence to infinity below the integral. Furthermore, the test functions can freely be chosen and thus, each function  $v_i$  or  $\hat{v}_i$  can be expressed as a linear combination of a finite number of basis functions  $w_\alpha$  or  $\hat{w}_\alpha$  with coefficients of  $\tilde{v}_\alpha$  or  $\tilde{\hat{v}}_\alpha$ , respectively.

$$v_i = \sum_{\alpha=1}^n \tilde{v}_\alpha w_\alpha$$

$$\hat{v}_i = \sum_{\alpha=1}^n \tilde{\hat{v}}_\alpha \hat{w}_\alpha$$

Inserting these expressions together with equation 3.18 into equation 3.19 yields a set of equations to determine the coefficients  $\tilde{\eta}_\alpha^i$  for the approximations of the functions  $\vec{u}$ .

Now, there are various ways to choose the shape functions as well as the test functions. In the *Galerkin method*, the choice  $w_\alpha = N_\alpha$  is made, thus choosing the same functions for expressing the solution and for testing. This also allows to use functions which are almost zero everywhere but in small regions. Then, the integral in equation 3.19 only contributes when neighbouring points are evaluated, thus limiting calculation to such nodes.

Finally, a criterion for convergence of the approximated solutions  $\vec{\eta}$  against the real solutions  $\vec{u}$  is needed. Assuming the shape functions and test functions are locally based polynomials, the criterion of completeness for convergence can be formulated: If the derivative of the  $m$ -th order occurs in the differential operators, a constant value has to be obtained for all polynomial coefficients up to the order  $m$ . Note that this has to hold true especially when the element size tends to 0. However, this criterion is automatically met when complete polynomials up to the order  $m$  are used as basis functions.

Often in physics, not only a static solution is of interest but also the time-dependency or the evolution of the static solution over time is investigated. Although this was not the case in this work, FEM offers methods to achieve such a simulation. One can either calculate the time-domain additionally to the spatial domain, adding one more dimension. On the other hand, one can independently discretise time and solve the static problem with time steps in between.

As final remark, note that most of the detailed calculation is handled by software packages today and the model generation represents the difficulty at hand. Especially the choice of static and periodic boundary conditions, detailed model features, adequate meshing of objects as well as the definition of calculation space and the usage of symmetries are of importance for a model. All these key points together decide whether a physical-reasonable solution can be found in a convenient time or not.

## 4. Materials and Methods

This chapter comprises all materials and the respective manufacturer or supplier as well as all processes utilised to achieve the results of this work. For each process, all relevant, tunable and available parameters are listed to reproduce the processes and achieve the reported outcome. If a parameter of interest is not noted, e.g. pressure during sputter deposition, then there was no measurement tool for this quantity available on the utilised system. Furthermore, note that results for the same process vary between different systems. Due to this, the following recipes are suited for the systems used in the course of this work, and need to be adapted for different systems to achieve the desired outcome. Also, for parameters which were varied during this work, only the optimal value is noted in this chapter, which was found during the experiments.

The first section describes the model generation for a numerical simulation of the probe geometry as well as the experimental configuration, which is later utilised. A finite element method software package is employed to create a stable model in which distinct parameters can be varied and thus their influence evaluated. Particularly challenging was the large structure geometry of several micrometres, which required a well-thought-out meshing to achieve reasonable computation times. Furthermore, the excitation by an electrical field had to be tailored to the model to prohibit a non-physical solution resulting from model limitations.

The second section describes the fabrication of silicon moulds with pyramidal cavities. Later, these moulds were used to release metal structures for TERS probe fabrication. This part of the work was entirely carried out under clean-room conditions using established microfabrication methods and systems.

The third section explains the release of the fabricated metal structures by modifying a standard ball bonding process and adapting it to satisfy the required demands. Also, the manufacturing of an adapter as well as the integration in the utilised SPM is described. Using these processes one can fabricate TERS probes for STM quickly prior to the near-field measurement.

The fourth section comprises all the processes utilised to fabricate polymeric cantilevers featuring pyramidal gold tips. While the STM tips have several essential requirements with respect to the sample of interest, cantilevers allow for a wider range of TERS investigations and are highly requested by application.

The fifth and final section holds all the knowledge to fabricate substrates with a pyramid covered surface by releasing hundreds of metal structures at once. This technique can be employed to achieve a statistical evaluation of the metal structure fabrication as well as to directly fabricate substrates for SERS measurements.

## 4.1. Computational Modelling and Simulation

FEM simulations were performed in collaboration with Dominik Gollmer<sup>1</sup> using the software package COMSOL Multiphysics 5.2. A sphere with a diameter of 8  $\mu\text{m}$  was generated to be used as the volume of calculation, with its centre defined as the origin (0,0,0) of the coordinate system. The refractive index of vacuum  $n_{vac} = 1$  was assigned to the medium inside the sphere. A perfectly matched layer with a thickness of  $\lambda/2$  was placed as a shell around the sphere to handle the calculation of the electrical field at the border.

The structure shape of interest was a four-sided metal pyramid with different orientations relative to the excitation beam. Figure 4.1 shows a technical drawing of the pyramid position with respect to the coordinate system. An upside down pyramid with the tip located at the origin, the center of the sphere, was defined. The pyramid with a square base is completely described by the apex angle  $\alpha$  and the fixed height  $h = 2.7 \mu\text{m}$ . All edges and most importantly the tip were rounded using a fillet with a radius defined as  $r$ . The material and electrical properties of gold, taken from [63], were assigned to the pyramid. The tip was then rotated around the  $z$ -axis by an angle of  $\varphi$  and afterwards around the  $y$  axis by an angle of  $\theta$ .

The parameter set and the standard values which nominally correspond to the experimental set-up configuration, as well as the region of variation noted in brackets, were chosen as follows.

$$\begin{aligned}\varphi &= 0^\circ \quad [0^\circ, \dots, 45^\circ] \\ \theta &= -30^\circ \quad [-30^\circ, \dots, 60^\circ] \\ \alpha &= 70.5^\circ \quad [70.5^\circ, \dots, 10.5^\circ] \\ r &= 25 \text{ nm} \quad [5 \text{ nm}, \dots, 40 \text{ nm}]\end{aligned}$$

For each of the four variation calculations, three of the parameters were kept constant at the standard values and one was varied over the region of interest.

### Electrical field

To simulate plasmonic excitation, an electrical background field  $\vec{E}_b$  was defined as a Gaussian beam profile using the following expression [64].

$$\vec{E}_b = \vec{E}_{b,0} \cdot \underbrace{\frac{\omega_0}{\omega(x)} \cdot \exp\left(-\frac{y^2 + z^2}{\omega(x)^2}\right)}_{\text{term I}} \cdot \underbrace{\exp\left(-ik \cdot \left(x + \frac{y^2 + z^2}{2 \cdot R(x)}\right) + i\eta(x)\right)}_{\text{term II}}$$

In this formula,  $\vec{E}_{b,0}$  denotes the electrical field amplitude of the beam and was defined to yield a linear polarization in the  $z$ -axis (p-polarization) according to

$$\vec{E}_{b,0} = 1 \text{ V m}^{-1} \hat{e}_z.$$

<sup>1</sup>Institute for Applied Physics, University of Tübingen, Germany

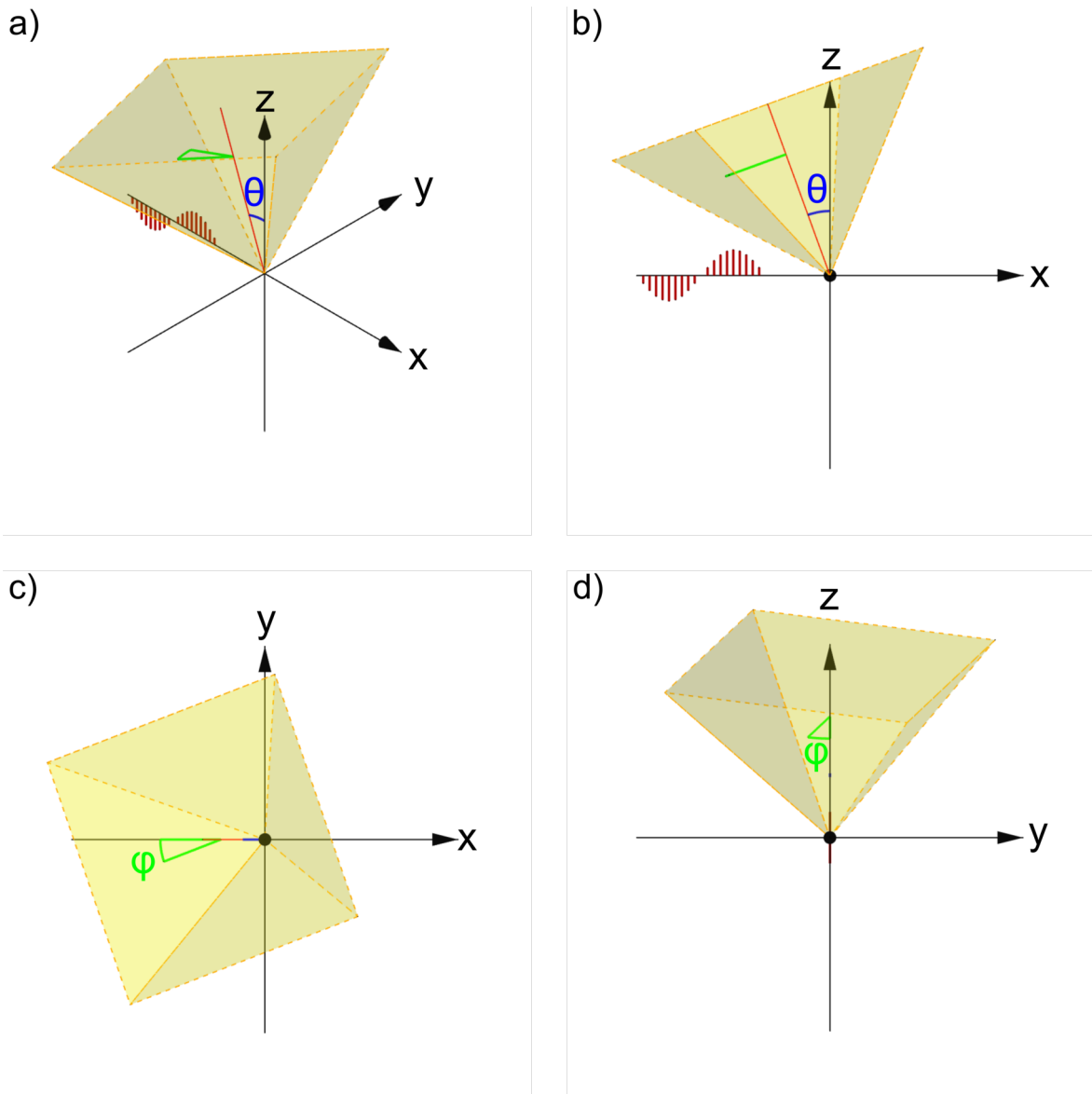


Figure 4.1.: Schematic of the computational model from different angles. The parameters of variation, here  $\theta = -30^\circ$  and  $\varphi = 10^\circ$ , are respectively marked in blue and green. The incident electrical wave is depicted in red. The image a) shows an isometric view, b) shows a projection on the  $x$ - $z$  plane, c) a projection on the  $x$ - $y$  plane and d) a projection on the  $y$ - $z$  plane.

The term  $I$  accounts for the varying waist size, where the function  $\omega(x)$  yields the distance from the beam axis, in the  $y$ - $z$  plane at position  $x$ , at which the field amplitude drops to  $1/e$ .

$$\omega(x) = \omega_0 \cdot \sqrt{1 + \left(\frac{x}{\pi\omega_0^2/\lambda}\right)^2}$$

Here, a value of 500 nm for  $\omega_0$  was chosen, which defines the waist size of the beam

in the focus. Furthermore,  $\lambda$  was set to 633 nm, which corresponds to the utilised laser wavelength in the experiment.

The term  $II$  describes the propagation of a wave essentially in positive  $x$ -direction. Aside from the classical exponent  $-ikx$ , the additional fraction containing the function  $R(x)$  takes into account the curvature of the beam and is given by

$$R(x) = x \left( 1 + \left( \frac{\pi\omega_0^2/\lambda}{x} \right)^2 \right).$$

Finally, the Gouy phase  $\eta(x)$  contributes a phase shift of  $\pi$ , when the beam passes through its focus and is given by

$$\eta(x) = \arctan \left( \frac{x}{\pi\omega_0^2/\lambda} \right).$$

In summary, a Gaussian beam is fully described by  $\vec{E}_{b,0}$ ,  $\lambda$  and  $\omega_0$ . Figure 4.2 shows a two-dimensional projection of the final model with the electrical excitation field. Note that the base of the pyramid, which also possesses sharp, plasmonically active features, is not in proximity to a strong field. The latter has to be dealt with when one uses a planar wave for excitation.

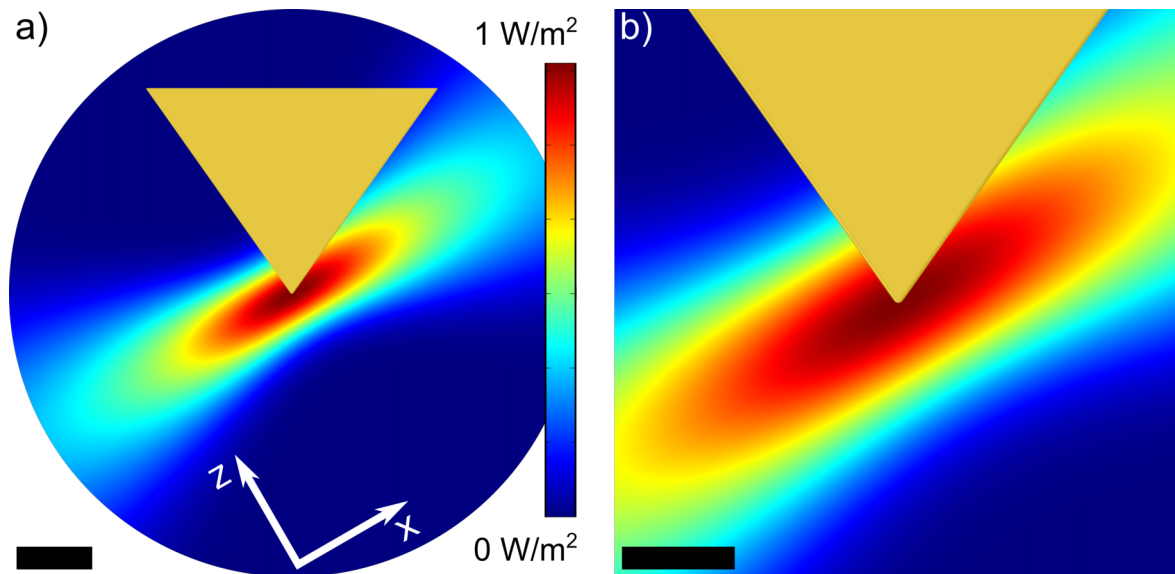


Figure 4.2.: a) Image of the FEM model showing the gold pyramid and the Gaussian beam using the standard parameter set. The electrical field intensity is colour coded (scale bar 1  $\mu\text{m}$ ). b) Magnification of the tip area, showing the confinement of the excitation field. The same colour scale as in a) is used (scale bar 500 nm).

Finally, the stability and convergence of the system was tested by varying parameters which should not influence the result of the calculation, e.g. the pyramid height and the mesh configuration. After guaranteeing that a stable solution is calculated, variations of the different parameters were performed. For evaluation and

comparison, the resulting electrical field was evaluated 2.5 nm below the tip for each parameter set.

## 4.2. Silicon mould fabrication

In this section all materials and process recipes are described that were used to fabricate moulds for the production of TERS probes, cantilevers and SERS substrates.

### 4.2.1. Silicon etching

Anisotropic silicon etching was performed to fabricate cavities with sharp features, which later could be transferred to a metal layer.

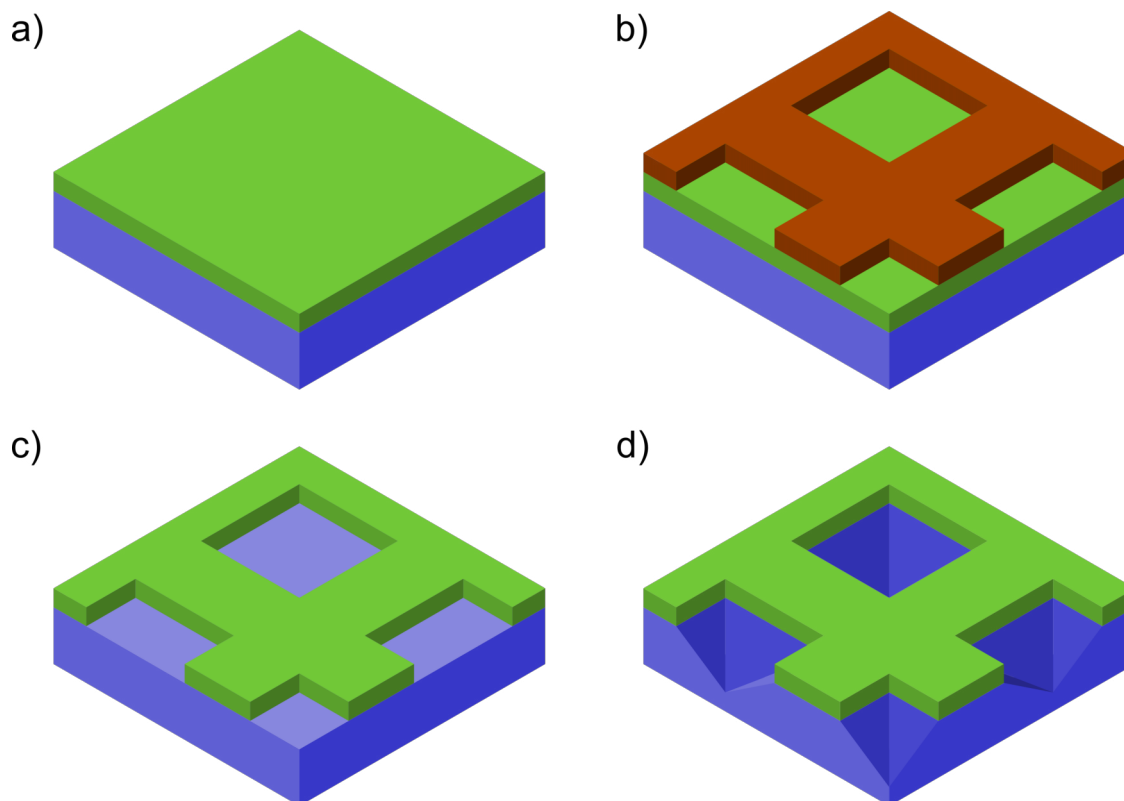


Figure 4.3.: Schematic of the mould fabrication. a) Section of a silicon wafer (blue) with a silicon nitride or silicon oxide mask (green). b) Structured resist layer (brown) on top of the substrate. c) Substrate after dry etching of the mask layer and resist removal. d) Substrate after anisotropic wet etching of silicon in potassium hydroxide solution.

Figure 4.3 depicts a schematic of the fabrication process of silicon moulds, which is explained in detail in the following paragraphs.

#### a) Substrate and mask deposition

A polished 4 inch, phosphorous n-doped cz-silicon wafer (Okmetic Oyj, Finland) with {100} orientation and a thickness of 380  $\mu\text{m}$  served as the substrate. Onto this, a 600 nm thick silicon nitride layer was deposited by PECVD using a PlasmaLab 800 (Oxford Instruments, UK) and the following recipe:

- 1 h heat-up linearly to 350 °C with 200 sccm nitrogen gas flow
- Ten times:
  - 1 min purge with 1000 sccm nitrogen at 1500 mTorr pressure
  - 1 min pump
- 50 min silicon nitride deposition with 15 sccm monosilane, 14 sccm ammonia and 785 sccm nitrogen gas flow. The pressure was set to 1000 mTorr, and it was alternated between 7 s low-frequency plasma with 40 W power and 15 s radio-frequency plasma with 40 W power.
- 3 h cool-down to room temperature

Alternatively, a 1 µm thick silicon oxide layer was deposited by PECVD using a PlasmaLab 800 (Oxford Instruments, UK) and the following recipe:

- 1 h heat-up linearly to 350 °C with 200 sccm nitrogen gas flow
- Ten times:
  - 1 min purge with 1000 sccm nitrogen at 1500 mTorr pressure
  - 1 min pump
- 50 min silicon oxide deposition with 16 sccm monosilane, 1000 sccm nitrous oxide and 784 sccm nitrogen gas flow. The pressure was set to 1000 mTorr, and a radio-frequency plasma with 100 W power was used.
- 3 h cool-down to room temperature

Afterwards, the mask layer was checked for defects and irregularities by optical microscopy before going to the next step.

## **b) Resist mask**

A 2 µm thick positive resist layer of S1818 (Shipley Company LLC, UK) was spin-coated on top of the mask layer using a Gamma-System (SÜSS MicroTec, Germany) and the following recipe:

- Application of 2 ml S1818
- 10 s pre-spin with 500 rpm and 10 steps of acceleration
- 30 s spin with 3500 rpm and 5 steps of acceleration
- 120 s soft bake at 115 °C on a hot plate
- 60 s cool-down on a cool plate at 20 °C

The resist layer was exposed using a MA6 (SÜSS MicroTec, Germany) mask aligner in soft-contact mode. The exposure dose was set to 20 s at 20 mW cm<sup>-2</sup>. The wafer flat was oriented by eye with respect to the vacuum chuck. The latter can be rotated in a controlled way with respect to the mask.

The lithography mask featured several thousand square holes in array formation with various side lengths ranging from 5 µm up to 100 µm and a spacing of at least 50 µm between two squares. Additionally, marker structures as well as lines and spaces for layer thickness measurements with a profilometer were available. The mask was aligned such that one side of the square holes is parallel to the wafer flat.

Development of the resist layer was performed using a Gamma-System (SÜSS MicroTec, Germany) and the following recipe:

- Coat with water
- Coat with AZ 826 MIF (MicroChemicals GmbH, Germany) developer
- Shake for 45 s, rinse with water and spin dry at 3000 rpm for 30 s

##### **c) Dry etching and resist remove**

Dry etching of the mask layers was performed by RIE using a PlasmaLab 800 (Oxford Instruments).

In the case of the silicon nitride mask, dry etching was performed in 12 min using 70 sccm tetrafluoromethane and 6 sccm oxygen gas flow. Pressure was set to 75 mTorr, and a radio-frequency plasma with 280 W power was applied.

In the case of the silicon oxide mask, dry etching was performed in 2 h using 3 sccm tetrafluoromethane gas flow. Pressure was set to 2 mTorr and a radio-frequency plasma with 100 W power was used. Alternatively, dry etching could be performed in 40 min by using 70 sccm tetrafluoromethane and 6 sccm oxygen gas flow. Here, the pressure was set to 75 mTorr, and a radio-frequency plasma with 280 W power was applied.

The resist removal was performed in acetone with 30 min of ultrasonic treatment. Afterwards, the wafer was rinsed with a copious amount of isopropanol and dried by blowing with nitrogen.

##### **d) Silicon etching**

Silicon wet etching was performed in a fume hood using a beaker with 2 l of 45% potassium hydroxide in water. The beaker was placed on a hotplate which features precise temperature control and magnetic stirring. The etching solution was heated up to 60 °C 3 h in advance under constant stirring.

The wafer was fixed in a purpose-built vacuum holder, sealing the backside with a glass disk. Therefore, only the structured front side is exposed to the etchant. The etching was performed for 6 h at 60 °C and under constant stirring.

The etching process was stopped by placing the vacuum holder with the wafer in 2% hydrochloric acid in water for 1 h. Afterwards, the substrate was rinsed with a copious amount of deionised water and dried by blowing with nitrogen.

Single crystalline silicon etch rates in potassium hydroxide are dependent on the crystal orientation of the exposed surface. Surfaces with {100} and {110} orientation are etched with rates of around 15  $\mu\text{m h}^{-1}$  and 25  $\mu\text{m h}^{-1}$ , respectively, for 45% KOH in water at 60 °C [65]. On the other hand, surfaces with {111} orientation are practically stable against this etchant. Thus, for a {100} orientated wafer, finite mask openings result in the generation of pyramids or wedges during etching, while {110} oriented wafers can be used to etch trenches.

There are several models to explain the nature of the anisotropic etching behaviour. One finds a different number of dangling bonds on the surfaces of different crystal faces in a silicon unit cell. For the {111} direction, only a single dangling bond is exposed while for the {100} direction and the {110} direction more bonds are exposed. In this case, more dangling bonds are expected to increase the etch rate. Likewise, the number of backbonds differs for different crystal faces. The {111} plane features three backbonds while the {100} plane only possesses two backbonds. Here, more backbonds are expected to lower the etch rate, however, the difference of orders of magnitude in the etch rate for the {111} direction and the {110} direction cannot be explained, since both feature three backbonds. Another model discusses

the etch rates with respect to the step-free energy of the different crystal planes [66]. Etching dominantly occurs at defects or steps on the crystal surface and the {111} plane is found to be the smoothest, while the {100} plane and {110} plane are considerably rougher.

Although different origins of the anisotropy are discussed, one can measure the etch rate of a distinct surface as a function of the etching temperature at a fixed etchant concentration, which allows to fit the Arrhenius equation. As a result, one finds numbers for the activation energy of the chemical reaction, which were determined to be 0.59 eV for the {100} plane, 0.6 eV for the {110} plane and 0.7 eV for the {111} plane (42 % KOH in water) [65].

#### 4.2.2. Oxidation and Metallization

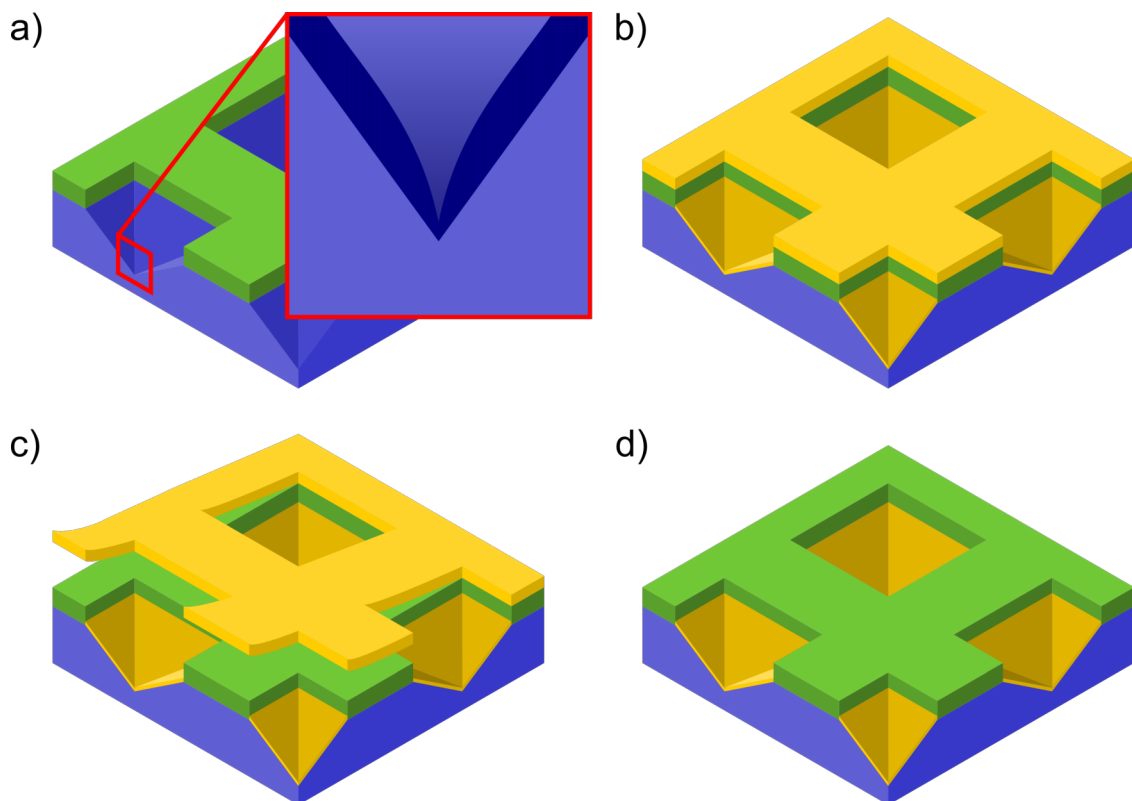


Figure 4.4.: Schematic of the structure fabrication. a) Section of a substrate after oxidation. b) Substrate after metallization with a gold layer. c) Lift-off of the gold layer everywhere but inside the pits. d) Section of the final substrate.

Figure 4.4 shows a schematic of the fabrication process for the gold structures using the fabricated silicon mould. The individual steps are explained in detail in the following paragraphs.

##### **a) Oxidation**

Oxidation of the substrate was performed using a FRH 200/500/1200 (Linn High Term GmbH, Germany) tube furnace and the following recipe:

- 1 h heat-up linearly to 900 °C with 200 sccm nitrogen gas flow
- Holding 900 °C with 200 sccm oxygen gas flow for 9 h 26 min (yielding 107 nm oxide growth on {111} silicon surfaces)
- 3 h cool-down with 200 sccm nitrogen gas flow
- Cool-down to room temperature without further gas flow

The oxidation time was varied with respect to the desired oxide thickness during the experiments.

##### **b) Metallization**

A metallisation with a 2 µm thick gold layer was performed by PVD using a Z500 system (Leybold AG, Germany) and the following sputter parameters:

- Pump to  $5 \times 10^{-5}$  mbar, fill the condensation trap with 2l of liquid nitrogen and pump to  $1 \times 10^{-5}$  mbar
- 5 min static sputtering with 120 sccm argon gas flow and a radio-frequency plasma with 1000 W power

Alternatively, a metallisation with a 280 nm thick gold layer was performed by PVD using a Balzers system and the following thermal evaporation parameters:

- Pump to  $3 \times 10^{-6}$  mbar and start water cooling
- Oscillating crystal tooling factor: 180
- Fine deposition with a rate of  $0.2 \text{ \AA s}^{-1}$  until a thickness of 20 nm is achieved
- Deposition with a rate of  $2 \text{ \AA s}^{-1}$  until a thickness of 280 nm is achieved

##### **c) Gold lift-off**

To lift-off the gold layer everywhere but inside the pits, it was grabbed at the corner of the substrate and pulled off using tweezers. This allowed to remove the gold layer from the substrate surface in one piece. It was possible to carefully blow remaining residues off the substrate using nitrogen.

An alternative way was to immerse the substrate in a solution of 2 % hydrofluoric acid in water for around 1 h. After lift-off, the substrate was rinsed with deionised water. Ultrasonic treatment had to be avoided, due to the fact that it led to an uncontrolled full or partial detachment of structures, and damaged shapes.

Additionally, in the case of a silicon oxide mask it was possible to immerse the substrate in a solution of 2 % potassium hydroxide in water for around 1 h. After lift-off, the substrate was rinsed with deionised water. Ultrasonic treatment, like before, had to be avoided.

### 4.3. Fabrication of STM TERS probes

Probes for TERS were fabricated by utilising the manufactured substrates and releasing the metal pyramid structures during a ball bonding step. While still connected to the bonder and oriented in a defined way, the probes were glued to an adapter piece which could directly be integrated in the SPM.

#### 4.3.1. Bonding and Release

Figure 4.5a shows an overview image of the utilised Model 4124 Universal Ball Bonder (Kulicke & Soffa Germany GmbH, Germany) and a magnification of the bonding mechanism, which was adapted for release of the metal structures. The system was turned on 30 min in advance, and the stage temperature was set to 150 °C. The substrate containing the gold pyramids, diced down to 2 cm · 2 cm, was fixed by one of the clamps to the heated sample stage. For the bonding step the following parameters were chosen:

- Gold wire thickness 20 µm, clamp closed
- Arc discharge 4 (corresponding to a ball size of 60 µm)
- Step 1: search height 10, force 5 (corresponding to 0.8 N), time 1, power 1
- Loop 0, so that the tip is resting on the surface after the bonding step 1

After placing the sample stage under the bonding position, search step 1 was started by pressing and keeping the trigger pressed. By reducing the search height manually, the bond ball was approached to the substrate surface. Figure 4.5b shows a schematic of the align and bonding procedure. After moving the bond ball in close proximity of a cavity containing a metal structure, the lateral position was optically controlled through a microscope and adjusted by the fine positioning control. By releasing the trigger button, the bonding was performed and the tip rested on the surface due to the low loop height setting. Next, the bonder was re-set, which resulted in the closing of the wire clamp and a straight upward retraction of the capillary, the ball and the bonded metal structure. Finally, the clamp was opened and around 10 mm of gold wire were pushed through the capillary with tweezers, resulting in the tip hanging downwards below the capillary. At this step, the tip was either directly taken out with tweezers, by cutting the gold wire with fine scissors, for further analysis or glued to an adapter piece and cut out for usage in the SPM.

#### 4.3.2. Adapter pieces and glueing

Adapter pieces were fabricated out of 100 µm thick 18 Cr 9 Ni steel foil (Hoffmann Group, Germany) by laser ablation. A CAD drawing of the adapter is depicted in Figure 4.6a, which was cut out of the steel foil using a ProtoLaser (LPKF, Germany) and the following parameters:

- 8 W laser power at 50 kHz laser frequency
- Scan field of 10 mm · 15 mm
- Mark speed of 500 mm s<sup>-1</sup>

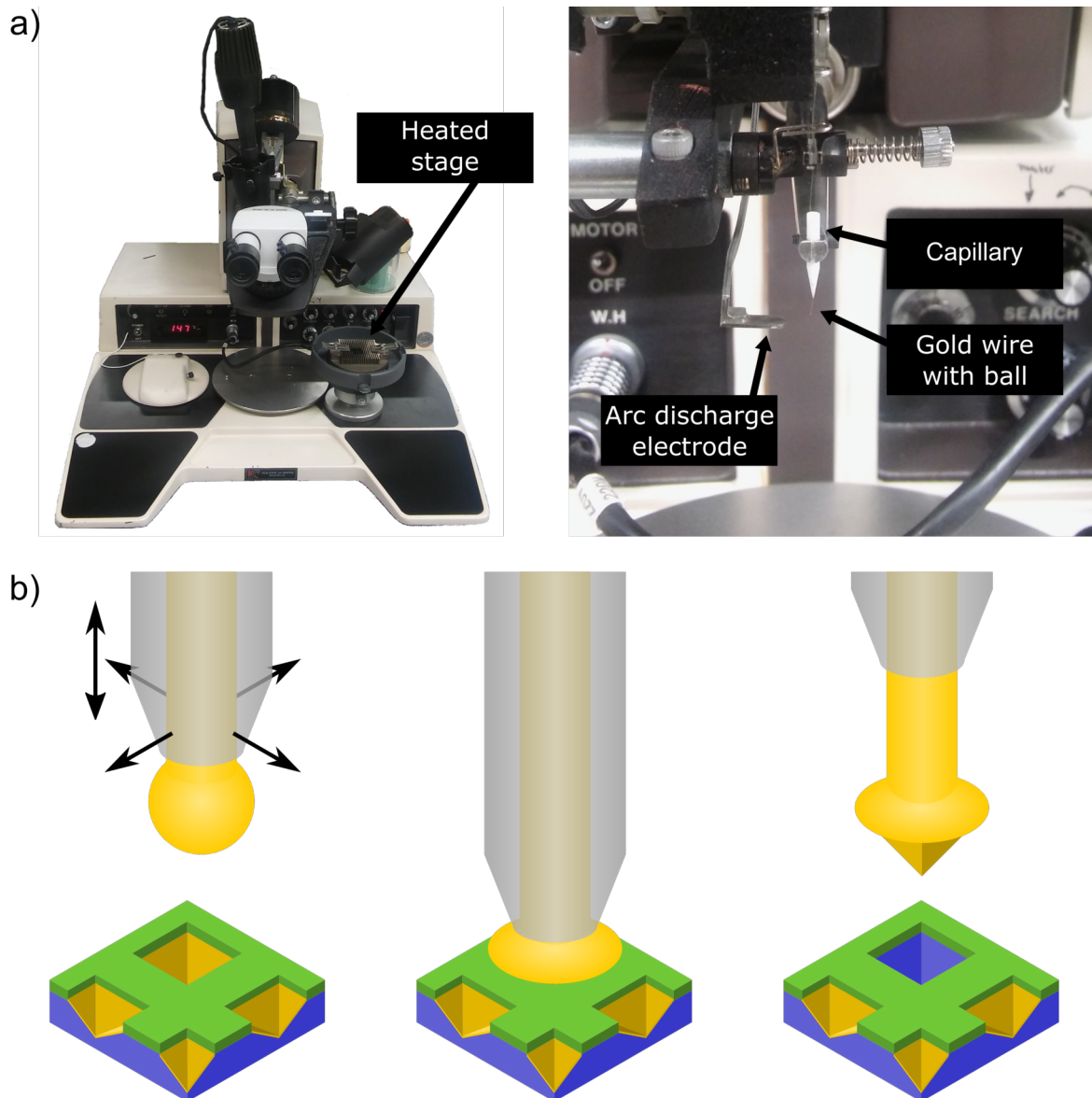


Figure 4.5.: a) Image of the Kulicke and Soffa Ball Bonder. b) Schematic of the bonding and release process.

- Start and end move of 20  $\mu\text{m}$
- 40 repetitions

The cut-out steel pieces were bent two times at  $45^\circ$  around the cut lines on the beam. Afterwards, the adapters were fixed in a helping hand<sup>2</sup> and adjusted to the bonded tip resting under the bonder capillary. A drop of silver glue was deposited on the v-shape area at the very end of the adapter piece, and a connection to the gold wire with the tip was made. Figure 4.6b shows a schematic of the configuration during the attachment of the adapter piece. After letting the adhesive dry for 15 min the gold wire was cut and the final adapter with probe could be stored or mounted

<sup>2</sup>A highly adjustable jig attached to a weighted base.

in the SPM for STM and TERS measurements.

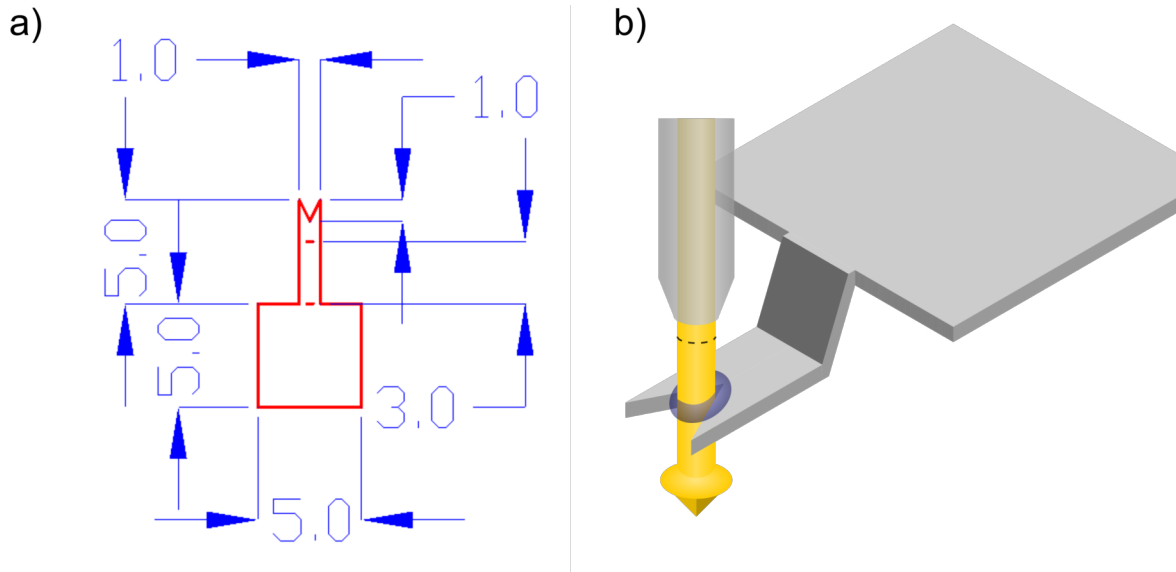


Figure 4.6.: a) CAD drawing of the adapter piece with dimensions in mm. The two  $300\ \mu\text{m}$  cuts on the beam were included to facilitate a bending of  $45^\circ$  at these lines. b) Schematic representation of the glueing configuration while the tips are still connected to the bonder. The adapter is depicted in grey, the adhesive in blue and the gold wire with the tip in yellow. After drying, the wire was cut at the dotted line.

### 4.3.3. Tungsten STM probe fabrication

A 300  $\mu\text{m}$  thick tungsten wire was used to fabricate standard probes for STM measurements for comparison. To fabricate a sharp tip, around 50 mm of wire were fixed with pliers, and side cutters were joined at an angle of  $45^\circ$ . Figure 4.7a shows a schematic of the fabrication process. While constantly pulling with the pliers the force on the side cutters was steadily increased, resulting in notching of the tungsten wire. At some point, the clamped piece of the wire could be ripped off, resulting in a sharp tip at the broken constriction.

Figure 4.7b shows a SEM image of a prepared STM probe. The cut area as well as the ripped area are visible. The wire with the tip was immediately mounted in the SPM cartridge and used for STM measurements.

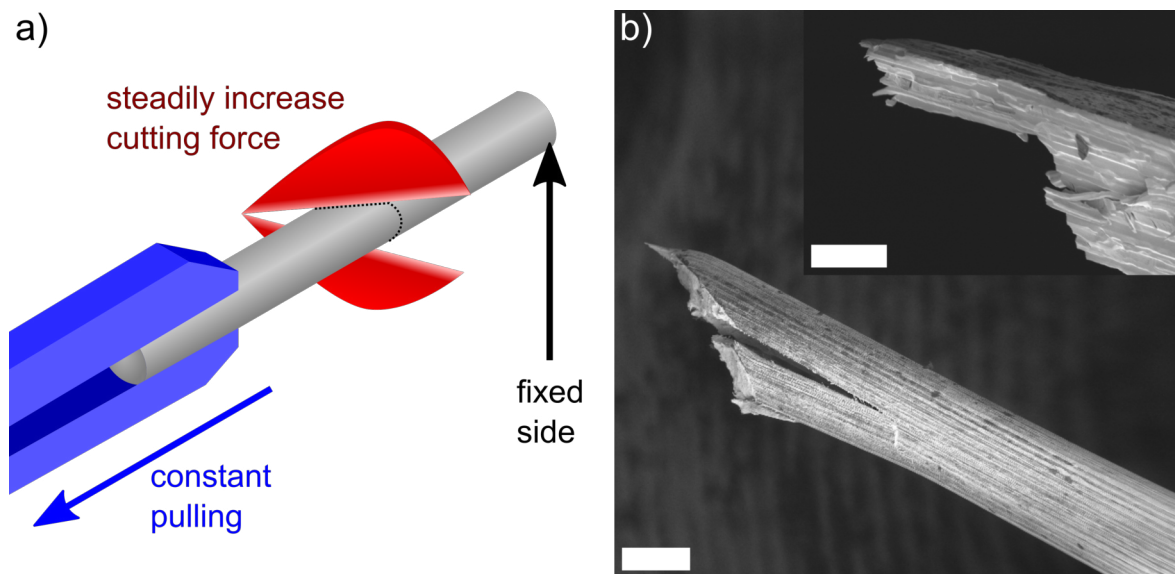


Figure 4.7.: a) Schematic drawing of the fabrication process for tungsten STM probes. The pliers are drawn in blue, the side cutters are drawn in red. b) SEM image of a fabricated tungsten STM probe (scale bar 200  $\mu\text{m}$ ). The insert shows a close-up of the very tip (scale bar 5  $\mu\text{m}$ ).

## 4.4. Fabrication of TERS cantilevers

In another fabrication process, the metallised moulds were utilised to manufacture cantilevers for contact mode AFM. Therefore, polymeric cantilever beams were structured on the wafer scale by lithography using negative resist. The cantilever chip was likewise fabricated out of polymer by lithography, using a two-layer spin-coat process to form a remarkably thick resist structure. Finally, the cantilevers were released one by one and could directly be mounted in the SPM.

### 4.4.1. Structuring of the cantilevers

Figure 4.8 shows a schematic of the developed process which is described in detail in the following paragraphs.

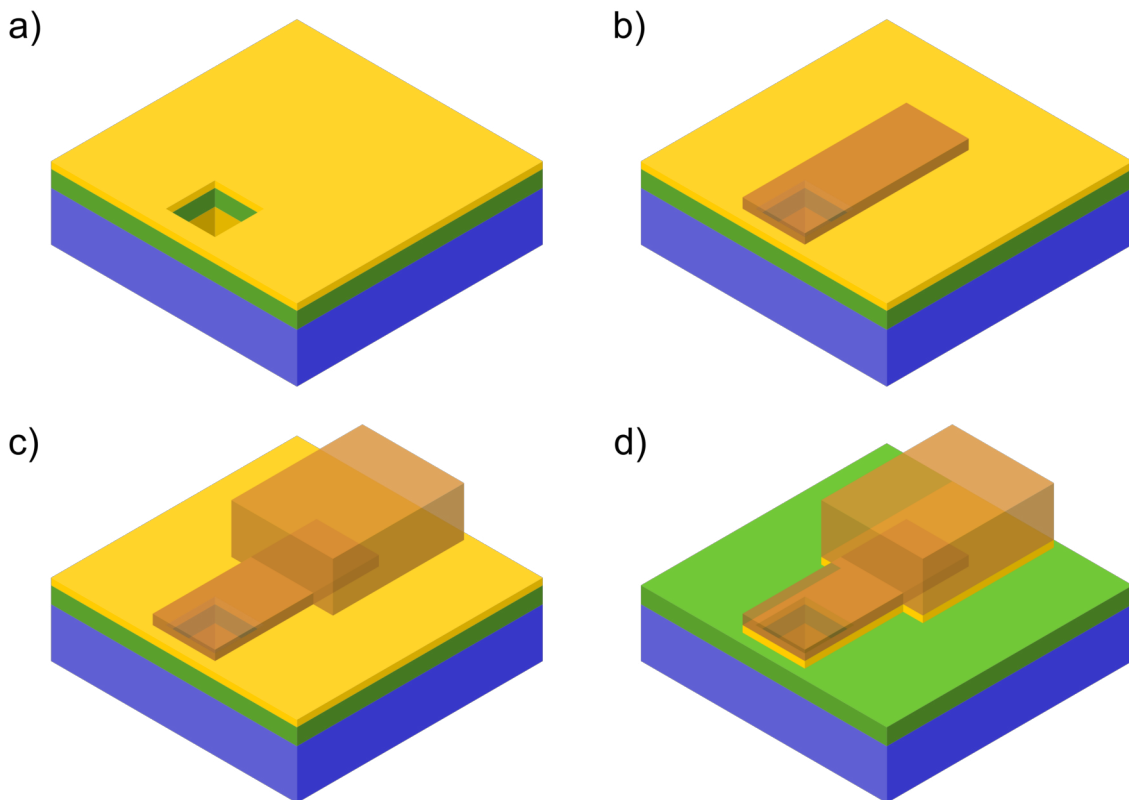


Figure 4.8.: Schematic of the cantilever fabrication. a) A mould substrate is fabricated as described before and metallised with a gold / chromium layer. b) A thin layer of SU-8 3005 resist is spin-coated and structured to form the cantilever beam. c) A thick layer of SU-8 50 resist is spin-coated and structured to form the cantilever chip. d) The exposed gold / chromium layer is removed by etching, and the cantilevers are ready to be released.

##### **a) Metallisation of the moulds**

A mould was prepared as described before, featuring square base cavities with side lengths of 40  $\mu\text{m}$  and a 5.5 mm / 3.3 mm grid spacing. Metallisation with a 100 nm thick gold layer followed by a 10 nm thick chromium adhesion layer was performed by PVD using a Z500 system (Leybold AG, Germany) and the following sputter parameters:

- Pump to  $5 \times 10^{-5}$  mbar, fill the condensation trap with 2l of liquid nitrogen and pump to  $1 \times 10^{-6}$  mbar
- 1 min dynamic gold sputtering with 120 sccm argon gas flow and a radio-frequency plasma with 1000 W power
- 1 min dynamic chromium sputtering with 120 sccm argon gas flow and a radio-frequency plasma with 1000 W power

##### **b) Fabrication of the cantilever beams**

Directly after sputtering, when the surface energy was still high, a thin layer of SU-8 3005 (MicroChem Corp., MA USA) was spin-coated using a Convac 1001 spin-coater and the following recipe:

- Dispense 5 ml of SU-8 3005
- 10 s pre-spin with 500 rpm and 5 steps of acceleration
- 30 s spin with 1000 rpm and 1 step of acceleration
- 5 min soft bake at 95  $^{\circ}\text{C}$  on a hot plate
- 5 min cool down on a cool plate at 20  $^{\circ}\text{C}$

The resist layer was exposed using a mask aligner MA6 (SÜSS MicroTec, Germany) in soft-contact mode. The exposure dose was set to 60 s at 12  $\text{mW cm}^{-2}$  using an optical i-line filter. The utilised lithography mask featured rectangular cantilever beams with dimensions of 310  $\mu\text{m} \cdot 100 \mu\text{m}$ .

Afterwards, a post-exposure bake for 1 min at 65  $^{\circ}\text{C}$ , followed by 3 min at 95  $^{\circ}\text{C}$  was performed on a hot plate. The substrate was cooled down and developed in acetone for 1 min, rinsed with a copious amount of isopropyl alcohol and blown dry with nitrogen.

##### **c) Fabrication of the cantilever chips**

Before the next step, the substrate was treated by an oxygen plasma to increase the adhesion between the present thin SU-8 layer and the following thick coating. Therefore, the substrate was processed in a Piccolo plasma system (Plasma Electronic GmbH, Germany) with a 60 s plasma using 100 sccm oxygen gas flow, a pressure of 2000 mPa and a radio-frequency power of 100 W.

Directly after, a 700  $\mu\text{m}$  thick layer of SU-8 50 (MicroChem Corp., MA USA) was spin coated using a Convac 1001 spin coater and the following recipe:

- Dispense 10 ml of SU-8 50
- 10 s pre-spin with 500 rpm and 5 steps of acceleration

- 30 s spin with 1000 rpm and 1 step of acceleration
- 10 min soft bake at 65 °C on a hot plate with open cover
- Dispense 10 ml of SU-8 50
- 10 s pre-spin with 500 rpm and 5 steps of acceleration
- 30 s spin with 1000 rpm and 1 step of acceleration
- 15 min soft bake at 65 °C on a hot plate with open cover
- Dispense 10 ml of SU-8 50
- 10 s pre-spin with 500 rpm and a 5 step ramp
- 30 s spin with 1000 rpm and a 1 step ramp
- 20 min soft bake at 65 °C on a hot plate with open cover, followed by 90 min at 95 °C on a hot plate with open cover

Spin-coating in two-steps is necessary, due to the fact that such a thickness cannot be achieved with a reasonable quality in a single spin-coat step. The resist layer was exposed using a mask aligner MA6 (SÜSS MicroTec, Germany) in soft-contact mode. The exposure dose was set to 180 s at 12 mW cm<sup>-2</sup> using an optical i-line filter. The utilised lithography mask featured rectangular cantilever chips with dimensions of 3.5 mm · 1.5 mm.

Afterwards, a post-exposure bake for 1 min at 65 °C, followed by 20 min at 95 °C was performed on a hot plate. The substrate was cooled down and developed in acetone for 10 min, rinsed with a copious amount of isopropyl alcohol and blown dry with nitrogen.

#### **d) Removal of excess metal**

In the final step, the excess metal not covered by resist on the wafer was removed by ion etching. The substrate was processed in a Z401 RIE system (Leybold AG, Germany) using the following recipe:

- Pump to base pressure of  $2 \times 10^{-4}$  mbar
- Set the argon flow to 50 sccm and the throttle valve to 100 %
- 20 min of etching using a radio-frequency plasma with a power of 100 W

The finished wafer was stored under clean-room conditions until the cantilevers were released.

#### 4.4.2. Release of the cantilevers

The cantilever structures were fabricated on an adhesive chromium layer, while the adhesion between the underlying gold and silicon mould is relatively weak. Due to this, no special treatment was necessary to lift-off the cantilevers from the mould.

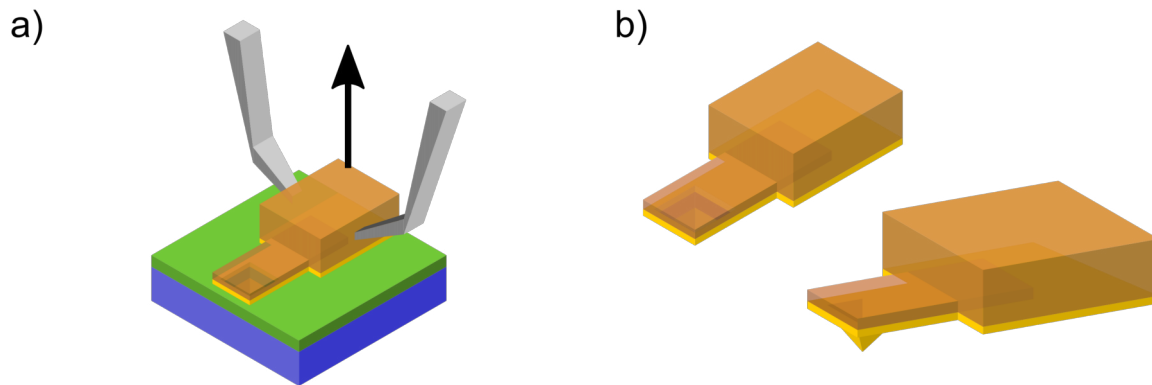


Figure 4.9.: Schematic of a) the cantilever release and b) the final cantilever from different perspectives.

Figure 4.9a shows a schematic of the release procedure. A single cantilever was grabbed with tweezers and lifted off in a straight upward motion from the substrate. Figure 4.9b shows a drawing of the final structures from different perspectives. The fabricated cantilevers featured a relatively short beam, due to the material being polymeric and thus offering a low spring constant compared to inorganic materials. Furthermore, the pyramidal gold structure featuring a large apex angle and serving as tip was located at the very end of the beam.

The released cantilevers were stored in a reverse position with the tip facing upwards in a standard cantilever box. The latter could be sealed and offered a silicone surface inside to which the cantilever chip sticks. For measurements, the fabricated cantilevers could be directly mounted in the same way as commercially available cantilevers, due to being designed with the same geometric dimensions.

## 4.5. Fabrication of SERS substrates

SERS substrates were fabricated by bonding an array of hundreds of metal structures, residing inside moulds, to a glass substrate and releasing them all at once.

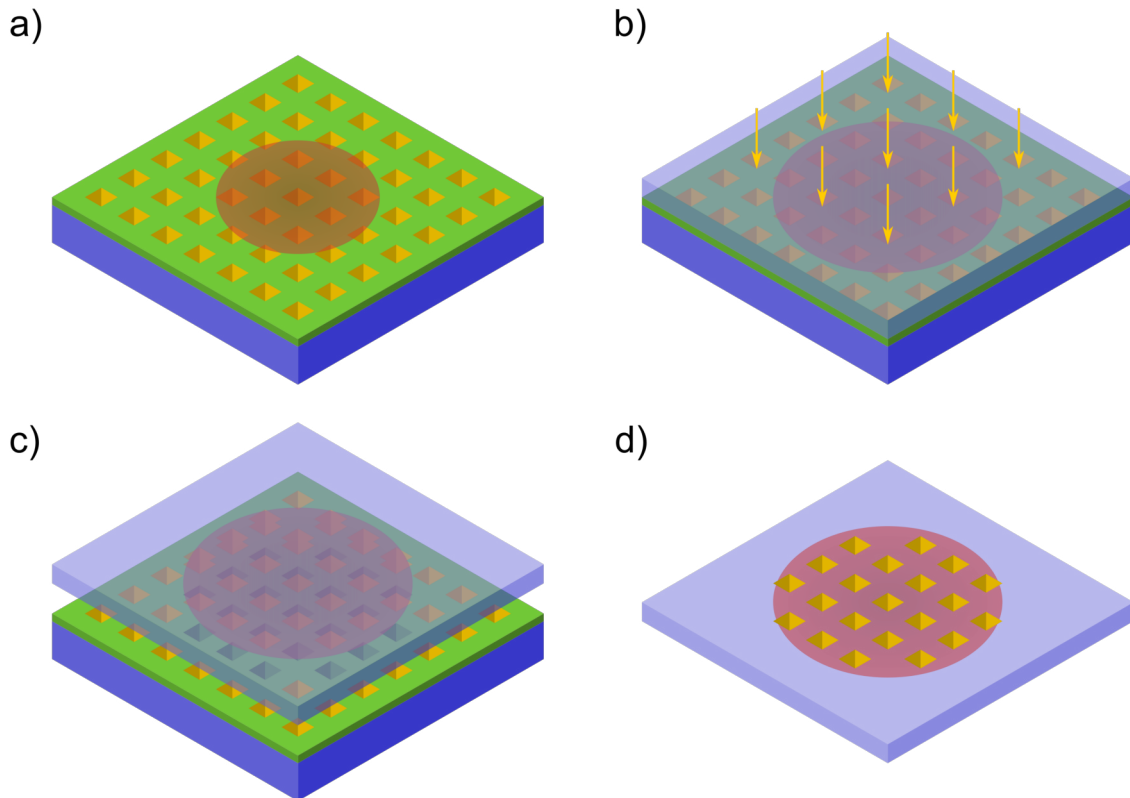


Figure 4.10.: Schematic of the SERS substrate fabrication process. a) A mould was prepared and metallised as described before. A droplet of adhesive was dispensed on top of some structures. b) A float glass substrate was pressed on top of the region with the adhesive. Curing was performed by UV light through the transparent substrate. c) The float glass substrate was released in a straight upward motion. d) The bonded metal structures on top of the glass could be used for SERS experiments.

Figure 4.10 depicts a schematic of the fabrication process for SERS substrates based on a moulding process, which is explained in detail in the following paragraphs.

### a) Mould preparation and adhesive

A mould was fabricated and metallised with a 100 nm thick gold layer as described before. The metal lift-off was performed in the same way. Afterwards, a 3 min air plasma treatment was performed using a PLASMAclean4 system (ILMVAC GmbH, Germany). Then, 100  $\mu$ l of Photobond 4436 adhesive (DELO Industrie Klebstoffe GmbH & Co. KGaA, Germany) was dispensed onto the substrate, covering several  $\text{mm}^2$  of metal structures.

##### **b) Bonding and curing**

A 1 mm thick float glass substrate was treated for 3 min in an air plasma using a PLASMAclean4 system (ILMVAC GmbH, Germany). Then, the glass was pressed onto the adhesive-coated mould substrate area and fixed with clamps. Next, curing of the adhesive was performed with an UV lamp for 3 min through the glass substrate.

##### **c) Release of the substrate**

For release, the clamps were removed and the substrates were separated keeping them as parallel as possible. It was helpful to separate the substrates starting at the edges and to pull the glass off afterwards.

##### **d) SERS substrate**

The finished glass slide featured several hundreds of gold pyramids on its surface. The substrate was stored in a sealed box until application or was directly coated with a solution of interest for SERS measurements.

## 4.6. Sample fabrication

Several samples for STM and TERS measurements were prepared. The following section contains all information about the substrates and includes a description of the processes to repeat the preparation.

### 4.6.1. Gold on silicon

(8 mm)<sup>2</sup> sized polished {100} silicon wafer pieces were coated with a 250 nm thick gold layer by PVD using a Z500 system (Leybold AG, Germany) and the following sputter parameters:

- Pump to  $5 \times 10^{-5}$  mbar, fill the condensation trap with nitrogen and pump to  $1 \times 10^{-6}$  mbar.
- 2.5 min dynamic gold sputtering with 120 sccm argon gas flow and a radio-frequency plasma with 1000 W power.

Directly after this, the samples were glued to a metal holder with silver conductor paste (Ferro Corporation, USA) so that they could be mounted on the SPM's piezoelectric stage. Furthermore, the conductor paste was used to create an electrical contact from the gold surface to the metal piece over two edges. This allowed to apply a bias voltage to the sample during SPM measurements, vital for scanning tunnelling microscopy.

### 4.6.2. Malachite green isothiocyanate (MGITC) samples

Malachite green isothiocyanate is a dye molecule, depicted in Figure 4.11. It is commonly applied as staining agent in biology and it is of particular interest for TERS due to its resonance at around 630 nm, which overlaps with the typical excitation wavelength of 633 nm when using gold probes. Furthermore, surfaces can easily be functionalised with MGITC solutions and its Raman signal yields sharp, distinct bands.

Malachite green isothiocyanate powder with a molecular weight of  $346.5 \text{ g mol}^{-1}$  (Sigma-Aldrich Chemie GmbH, Germany) was used to mix differently concentrated solutions. A stock solution with a concentration of  $10^{-3} \text{ mol l}^{-1}$  was prepared by mixing 17.3 mg of MGITC powder in 50 ml of analytical grade ethanol Emsure (Merck KGaA, Germany). A vortexer was utilised to speed up dissolution, and 10 min of ultrasonic treatment were added to ensure proper mixing.

A MGITC solution with a concentration of  $10^{-5} \text{ mol l}^{-1}$  was fabricated by mixing 100  $\mu\text{l}$  of the stock solution with 10 ml of analytical grade ethanol. A vortexer was used to ensure proper mixing. Another MGITC solution with a concentration of  $10^{-7} \text{ mol l}^{-1}$  was fabricated by mixing 100  $\mu\text{l}$  of the  $10^{-5} \text{ mol l}^{-1}$  concentrated solution with 10 ml of analytical grade ethanol. Again, a vortexer was used to ensure proper mixing.

As substrates, gold coated silicon pieces fabricated as described before were utilised.

The samples were glued to a metal holder with silver conductor paste (Ferro, Ohio USA) so that they could be mounted on the SPM's piezoelectric stage. Again, the conductor paste was also used to create an electrical contact from the gold surface to the metal piece over two edges.

Afterwards, the samples were treated in an air plasma using a plasma cleaner PDC-002 (Harrick Plasma, New York USA) for 2 min to make the surfaces hydrophilic and thus promote wetting of the substrates with liquids.

The samples were put on a hotplate at 30 °C in a fume hood. After 1 min, 10 µl of diluted MGITC solution was dispensed with a pipette on the surface. After 2 min, the dried samples were removed from the hotplate and stored under dry, clean conditions until the Raman and TERS measurements.

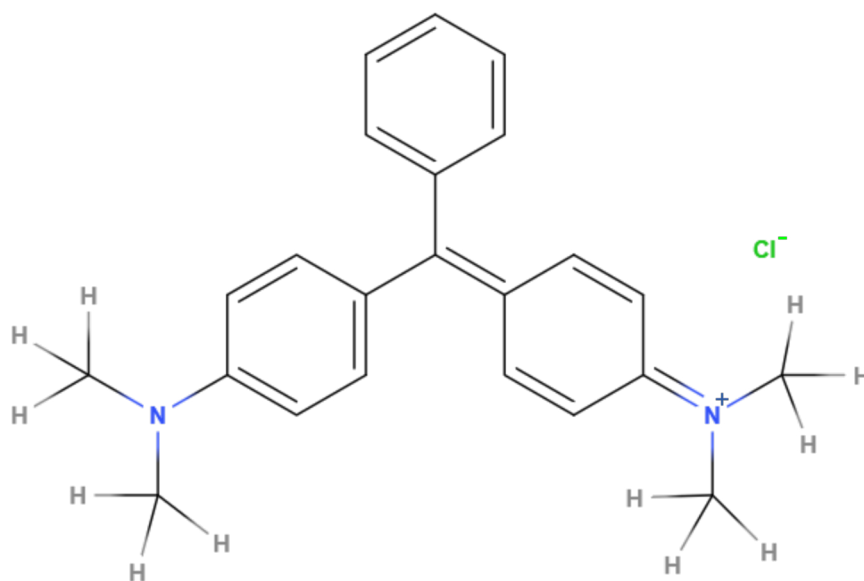


Figure 4.11.: Molecular formula of MGITC, drawn using <http://molview.org>.

#### 4.6.3. Amorphous carbon samples

Amorphous carbon was applied as a test sample due to its compatibility to sputter processes. Thus, ultra-thin layers could be structured, which allowed to investigate the sensitivity of TERS. Furthermore, STM compatibility was expected and amorphous carbon is Raman active, although it only yields a broad band signal.

As substrates, gold coated silicon pieces fabricated as described before were utilised. A carbon layer was deposited by PVD using a sputter coater 108auto (Cressington Scientific Instruments Ltd., UK) and a carbon target (Goodfellow, Germany). The sputtering was performed with the following recipe:

- Pump to  $3 \times 10^{-2}$  mbar
- Flush the chamber two times with argon
- Open the leak valve and sputter with 80 mA current for the desired time

The samples were glued to a metal holder with silver conductor paste (Ferro, Ohio USA) so that they could be mounted on the SPM's piezoelectric stage. Again, the conductor paste was also used to create an electrical contact from the gold surface to the metal piece over two edges.

#### 4.6.4. Thin PEDOT:PSS coating

PEDOT:PSS is a composite consisting out of an electrically conductive polymer (PEDOT) doped with anions (PSS). Its molecular formula is depicted in Figure 4.12. This material was utilised as a test sample due to its Raman activity and compatibility to STM feedback, as it combines sharp bands with chemically stable and immobilised molecules. Furthermore, it could be applied in thin layers by spin-coating and could be structured by (electron beam) lithography techniques.

A silicon sample coated with a 25 nm PEDOT:PSS layer was fabricated by Dominik Gollmer<sup>3</sup>. Firstly, a 5 mm · 5 mm squared silicon piece was coated with a 3 nm thick titanium adhesion layer followed by a 50 nm thick gold layer. Afterwards, a 1.1 % PEDOT:PSS in water solution (Sigma-Aldrich Chemie GmbH, Germany) was spin-coated. The pre-spin was done at 2600 rpm for 6 s, followed by spinning at 5000 rpm for 60 s. Finally, the substrate was baked at 150 °C for 1 h. The layer thickness was determined by using a profilometer and measuring across a scratch.

The samples were glued to a metal holder with silver conductor paste (Ferro, Ohio USA) so they could be mounted on the SPM's piezoelectric stage. Again, the conductor paste was also used to create an electrical contact from the gold surface to the metal piece over two edges.

---

<sup>3</sup>Institute for Applied Physics, University of Tübingen, Germany

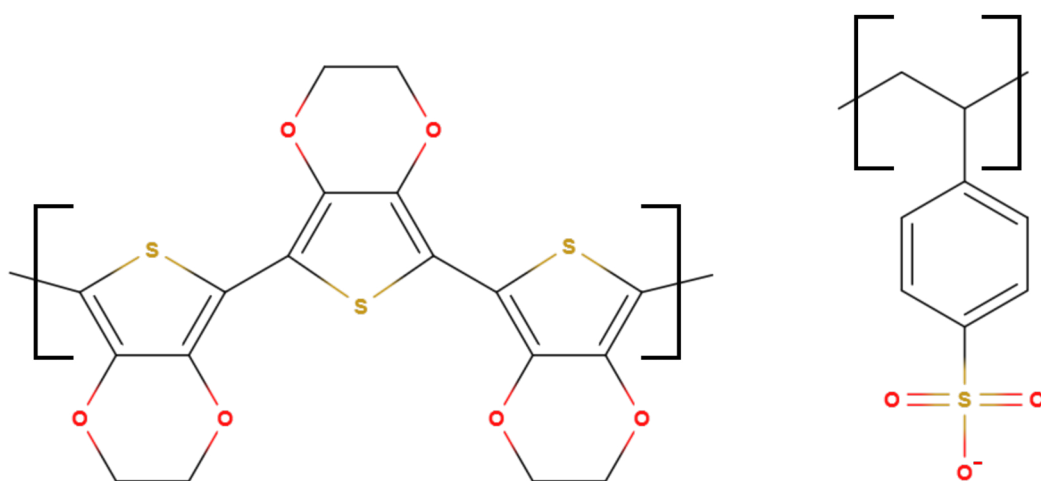


Figure 4.12.: Molecular formula of PEDOT:PSS, drawn using <http://molview.org>. The left molecule chain depicts the PEDOT, the right molecule chain depicts the PSS.

## 5. Experimental set-up

This chapter comprises a description of the experimental set-ups utilised for SPM, Raman and TERS measurements. The first section describes the Raman spectrometer with the optical excitation and signal collection path. The second section briefly characterises the Raman spectrometer and discusses the measurement configuration. The third section presents the utilised SPM and measurement conditions. The fourth and final section comprises a description of the Raman to SPM coupling set-up, needed for TERS experiments, and critical information.

### 5.1. Raman set-up

A commercially available inVia Raman system (Renishaw GmbH, Germany) was utilised for all Raman related measurements during this work. Figure 5.1 shows a schematic of the optical path as well as a labelled image of the spectrometer. The set-up is explained in detail in the following paragraph. Note that the parts within the orange frame are located inside the spectrometer casing, while the other parts were set up on an optical bench.

Two different lasers were available for excitation. A helium neon gas *laser 1* with a wavelength of 633 nm and a nominal output power of 16 mW as well as a frequency doubled Nd:YAG solid-state *laser 2* with a wavelength of 532 nm and a nominal output power of 100 mW were installed. The laser power could be adjusted in increments of 100 %, 50 %, 10 %, 5 % etcetera. Two fixed mirrors *M1* and *M2* were utilised to couple the corresponding laser into the Raman spectrometer casing. All measurements in this work were conducted using the 633 nm laser, due to the material choice of gold for TERS tip fabrication.

A first mirror *M3* could be steered mechanically and was used in combination with a retractable *pinhole* to adjust the incoming laser beam onto the optical axis of the set-up for maximum intensity and resolution. Afterwards, the pinhole was retracted to minimise losses of the excitation power.

Next, two mirrors *M4* and *M5* allowed to deflect the laser through different combinations of  $\lambda/4$  plates, which could turn the polarisation of the laser beam by 90° with respect to the standard linear polarization or could yield circularly polarised light.

Afterwards, the mirror *M6* was used to deflect the beam to the integrated microscope (Leica Microsystems GmbH, Germany). Furthermore, a semi-transparent mirror could be chosen to additionally couple in an optical path of a camera *Cam* that allowed imaging of the sample. The mirror *M6* is set to full reflection during measurement and could also be retracted to allow for an external optical path, which is described in the section covering Raman SPM coupling for TERS. The microscope

## 5. Experimental set-up

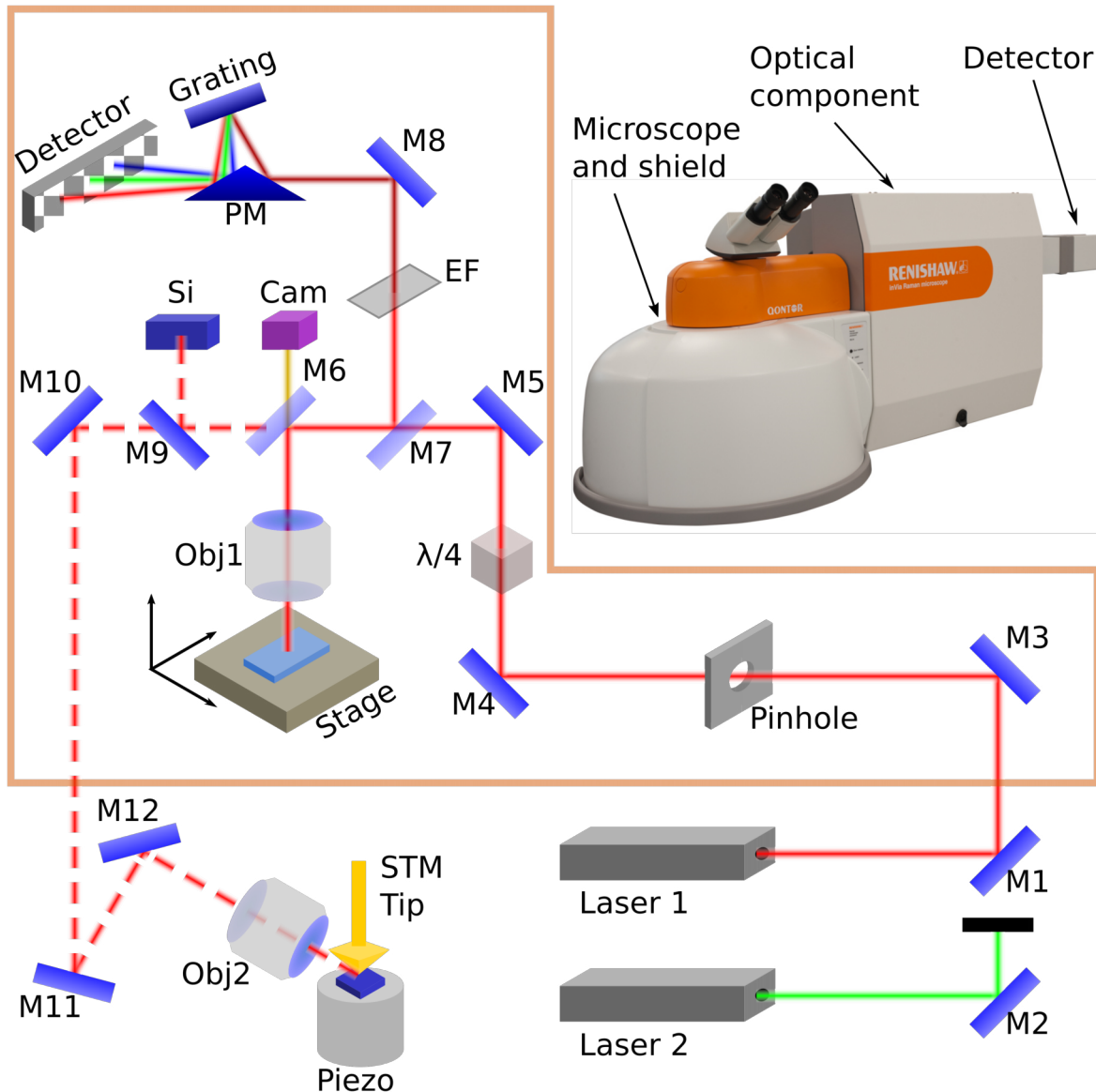


Figure 5.1.: Optical path used in the Raman system and for TERS experiments. The parts within the orange frame are located inside the inVia casing. The photograph shows the Raman system with a description (picture taken from [www.renishaw.de](http://www.renishaw.de)).

featured four different objectives *Obj1* with 5x, 10x, 50x and 100x magnification. The microscope's *x-y-z stage* could be operated by hand, with a controller and software controlled for 2D and 3D Raman imaging.

The signal collection took place in reflection mode using the same objective *Obj1* and mirror *M6* as for excitation, but with a deflection by the semi-transparent mirror *M7* sending the beam into the detection path. There, an edge filter *EF* was utilised to filter out the excitation wavelength. Another mirror *M8* was used to deflect the beam onto a prism mirror *PM*. This guided the beam onto a deflection *grating* which was used for spectral splitting. The resulting spectral components were diffracted

back to the mirror prism and from there finally deflected onto the CCD *detector*. The latter was cooled by a Peltier element to  $-70^{\circ}\text{C}$  for reduced thermal noise. Four different gratings with  $600\text{ lmm}^{-1}$ ,  $1200\text{ lmm}^{-1}$ ,  $1800\text{ lmm}^{-1}$  and  $2400\text{ lmm}^{-1}$  were available. However, all experiments were conducted using the  $1800\text{ lmm}^{-1}$  grating, which provided the best compromise of spectral range and resolution.

Furthermore, by retracting mirror *M6* and using mirror *M9* the beam could be deflected onto an inbuilt silicon reference sample. Also, a controllable slit aperture was available to allow for confocal imaging, which increases the depth resolution for 3D Raman imaging.

## 5.2. Raman characterisation and measurements

Signal collection from the inbuilt silicon substrate's Raman peak at  $520\text{ cm}^{-1}$  for 1 s using the highest laser power was utilised for a daily one-point calibration of the detector. The effective laser power on a sample for the red  $633\text{ nm}$  laser was measured using an optical power meter (Thorlabs GmbH, Germany) to be  $13.3\text{ mW}$  in the case of the standard Raman path and  $13.9\text{ mW}$  for the TERS path. For the green  $532\text{ nm}$  laser, effective power values of  $76.5\text{ mW}$  for the standard Raman path and  $79.3\text{ mW}$  for the TERS path were measured. All Raman and TERS measurements were performed using an acquisition time of 1 s and accumulating signal counts for the desired time.

Standard Raman measurements were performed using solely the red laser, especially since a comparison to TERS measurements was often pursued. For comparison experiments, the excitation power was set to the same value as in the respective TERS measurement. For 2D Raman mapping, the highest possible laser power, at which the sample did not degrade or was otherwise changed, was evaluated in advance.

TERS measurements were performed using solely the red laser with a power setting of up to 10 %, yielding an effective power of  $1.4\text{ mW}$  on the tip. The option of confocal microscopy was not utilised. Polarisation of the laser was always set in-plane to the sample surface normal and the *k*-vector of the laser beam (p-polarised).

## 5.3. SPM set-up and measurements

SPM measurements were performed using a commercially available Innova system (Bruker Corporation, US) shown in the picture in Figure 5.2a. The system consisted of a heavy base, containing the electronics and providing damping against vibrations. Furthermore, a movable top-side microscope was available to image the sample and SPM tip from above. The main component of the SPM microscope was the sample scanner and the detachable SPM head, which holds the probe and the feedback optoelectronics.

Figure 5.2b shows a schematic of the scanner components. The SPM head was placed on three stepper motors, which were used for roughly approaching the tip to the sample surface. Furthermore, a mechanism was available to move the head

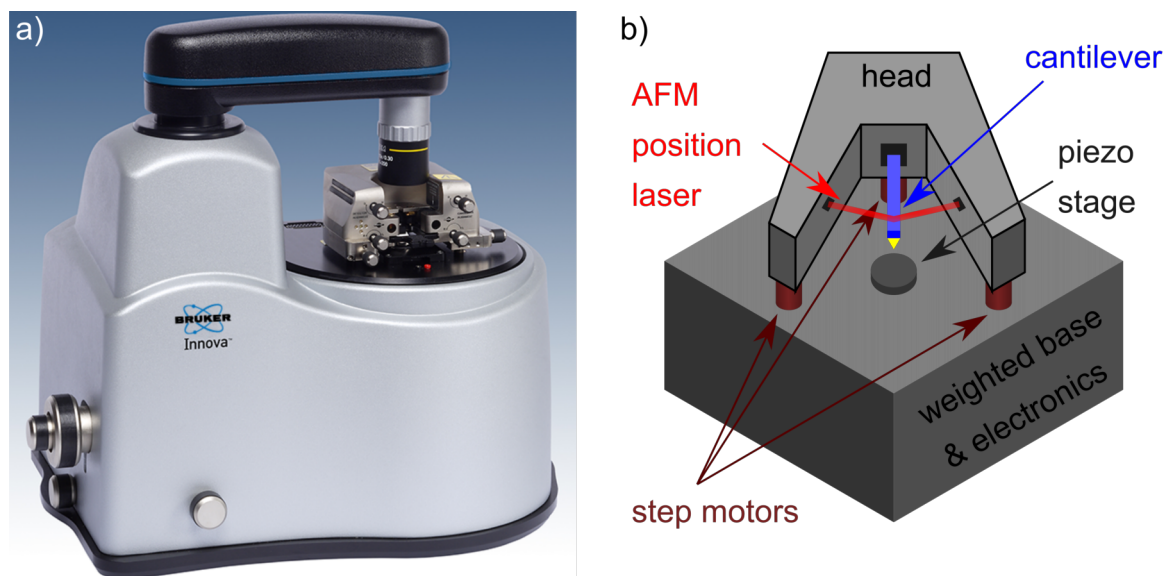


Figure 5.2.: a) Photograph of the Bruker Innova SPM (picture taken from the instruction manual by Bruker Corporation). b) Schematic of the main components: SPM head, step motors and piezo stage.

in  $x$ - and  $y$ -direction for lateral tip positioning on the sample. One of three different kinds of adapters was inserted into the SPM head for operation as STM, contact or non-contact AFM, respectively. The STM adapter featured a holder for up to 500  $\mu\text{m}$  thick wires as well as a possibility to fix the tip adapters, fabricated in this work, in a conductive arrangement. The AFM adapters featured a clamp for cantilevers with and without a piezoelectric vibration generator for non-contact and contact AFM, respectively. Furthermore, the SPM head contained an adjustable laser diode and an adjustable four-quadrant photodiode for cantilever feedback. Two different kinds of SPM heads were available offering either a broadband red laser (600 nm to 700 nm) or an infra-red laser (850 nm) to monitor the cantilever position. The latter was used for all TERS experiments in this work to prevent overlap with the Raman excitation laser and disturbance of the signal collection.

The samples were usually glued in a conductive way to a round metal holder. This holder could be placed on the magnetic sample stage, which is located on a piezoelectric tube. Two different voltage calibrations were available for the piezoelectric tube: a large area 100  $\mu\text{m}$  · 100  $\mu\text{m}$  range calibration and a small area 20  $\mu\text{m}$  · 20  $\mu\text{m}$  calibration. All TERS measurements were performed using the finer calibration table.

Typical STM parameters for gold samples, as were most often used in this work, were 0.5 V to 1 V bias, with the sample positively charged, and a tunnel current set point of 1 nA. Here, PID control was usually set to 1.0/0.1/0 and then optimised for imaging topography with the piezo's  $z$ -value. Scan speeds were kept below 500  $\text{nm s}^{-1}$ . Approach parameters were chosen to the finest possible setting after the tip was approached by hand below a distance of 50  $\mu\text{m}$ . This could be easily achieved, because the tip could be followed visually using the TERS coupling objective and the Raman spectrometer's camera.

A typical contact AFM feedback set point was 1 V difference between the upper and lower quadrants of the photodiode. Here, PID control was usually set to 1.0/0.5/0 and then optimised for imaging topography with the piezo's  $z$ -value. Scan speeds were kept below  $1 \mu\text{m s}^{-1}$ . Approach parameters were likewise chosen to the finest possible setting after the tip was approached by hand below a distance of  $50 \mu\text{m}$ .

Scan fields for TERS imaging were standardised to  $1.28 \mu\text{m}$ , yielding a pixel size of  $5 \text{ nm}$  using a value of 256 symmetrically for the number of points and lines. The SPM offered a mountable cover to shield against acoustic vibrations, which was particularly useful to shield against stray light from the room during TERS measurements and thus always employed in this kind of experiments. SPM images were evaluated using the software WSxM 5.0 [67]. Linear levelling and  $z$  rescaling proved to be sufficient for image post-processing due to the small scan field size of  $1.28 \mu\text{m}$ . No smoothing or other editing was performed.

## 5.4. Raman-SPM coupling for TERS

The coupling between the Raman spectrometer and the SPM was achieved by deflecting the beam along an external path onto the SPM probe. Figure 5.1 shows this coupling schematically with a dashed laser beam. Mirrors  $M10$ ,  $M11$  and  $M12$  were used in combination with a long range objective  $Obj2$  (Mitutoyo GmbH, Germany) to focus the laser beam onto the SPM tip. The objective was specified with a magnification of 50x, a focal length  $f = 200 \text{ mm}$  and a numerical aperture  $NA = 0.42$ . Note that the mirror  $M12$  together with the objective could be moved in  $x$ -,  $y$ - and  $z$ -direction without disturbing the optical path. With a first generation stage, the objective motion happened in a Cartesian space while with a second generation stage, replaced halfway throughout this work, the  $z$ -axis was changed to be along the objective direction.

Figure 5.3a shows an image of the SPM with the approached TERS objective. The schematic in Figure 5.3b shows the configuration from the side for TERS with STM and AFM feedback. In STM mode the tip was approached perpendicularly to the sample surface. Thus, together with the angle of  $30^\circ$  between the surface and the objective the classical TERS angle of  $60^\circ$  between tip axis and excitation was achieved. In the case of AFM feedback an additional system-specific angle of  $30^\circ$  had to be considered. This led to an angle of  $30^\circ$  between tip axis and excitation for classical cantilevers with vertical tips and thus, to restricted optical access.

TERS point measurements were performed by following a self-developed procedure. After setting up the Raman spectrometer and approaching a probe to the sample, the Raman laser was focused on the very tip of the probe using the camera image. Then, continuous Raman spectra acquisition was started and the laser was moved slowly in  $x$ - and  $y$ -direction without visual feedback. After TER signals were found, a fine variation of the  $z$ -axis was used to increase the signal further. If no TER signal was found, the camera was turned back on and the adjustment was repeated from the beginning.

TERS mapping was conducted by first acquiring an SPM image and defining the

## 5. Experimental set-up

area of interest. A MatLab script was used to coordinate SPM movement and spectrum acquisition. Briefly, it was possible to move the SPM tip to each  $n$ th pixel in  $x$ -direction and to each  $m$ th pixel in  $y$ -direction of the SPM image and acquire a TER spectrum. Thus, the resolution was technically limited to the SPM image resolution. After adjusting the laser and maximising the TER signal as described before, the automatic mapping was started.

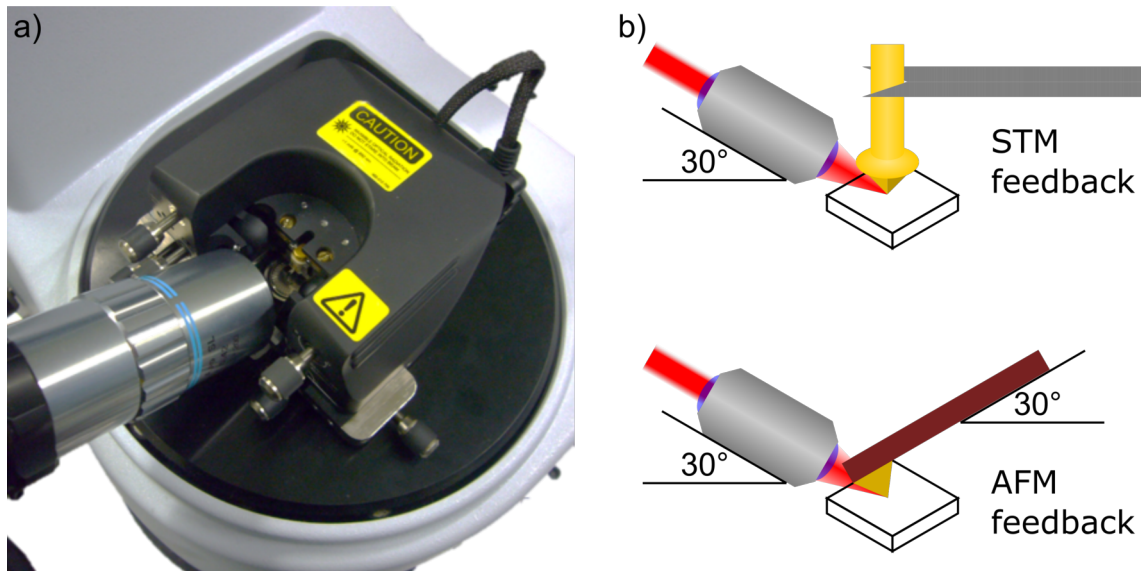


Figure 5.3.: a) Photograph of the TERS coupling into the SPM. b) Schematic of the TERS excitation from the side for STM and AFM feedback.

## 6. Results and Discussion

The following chapter comprises the presentation, description and discussion of the achieved results. Similar to the previous chapters, the results are arranged into sections with respect to the thematic focuses of the thesis. Each section starts with a discussion of relevant literature and continues with the findings of this work. Finally, if possible the results are compared to literature and published work.

The first section comprises the results of the computational simulation. For this purpose, the field enhancement at a tip was calculated for different conditions and the resulting near-field was evaluated to understand its correlation to the structure's geometrical properties and the excitation direction. This knowledge was later critical for the process development and evaluation.

The second section comprises the fabrication of silicon moulds, which were utilised for all TERS structure productions by template stripping. Here, smooth-surfaced, inverse pyramidal templates of different sizes with sharp geometrical features were realised. Furthermore, the surface energy was reduced by oxidation to sharpen the features further and facilitate moulding.

The following two sections cover the fabrication of STM TERS probes and all the measurements performed to evaluate these tips. Briefly, the fabricated moulds were metallised, and a process was developed to release single structures in a controlled way. The structures were conductively connected and could be directly utilised as STM probes when bonded to a specifically designed adapter. These probes were applied to acquire STM images, TER signals from few molecules of malachite green, TER signals from ultra-thin carbon layers and to analyse a thin PEDOT-PSS layer.

Next, the following section presents the realisation of AFM TERS cantilevers, using the template stripping technique, as well as first TERS measurements achieved with such probes. For this purpose, cantilever beams and chips were structured out of a remarkably thick polymer layer and released together with the moulded metal structure. The relatively soft cantilevers could then be utilised for AFM measurements and TER signal collection.

The final section contains information about the fabrication of SERS substrates utilising template stripping. Briefly, an array of moulded metal structures was released at once from the mould and covered with malachite green molecules. TER signals could then be measured at the hotspots when molecules were present.

Some of the results presented in this chapter have already been published in the form of conference contributions and articles [68, 69].

## 6.1. Computational Modelling and Simulation

Numerical modelling with a finite element method (FEM) of the plasmonic properties of structures is an established method to learn about the characteristics of TERS probes and to optimise the fabrication process as well as the experimental conditions. Before the results of the calculations are presented, different investigations of other groups, which are closely related to this work, are discussed.

Micic et al. reported a 3D FEM calculation solving Maxwell's equations in the frequency domain in the framework of the application of TERS on biological sample systems [70]. One of the calculations performed dealt with the model of a conical silver cantilever tip in close proximity to a silver nanoparticle using a planar wave with a wavelength of 810 nm for excitation. It was observed that the critical factors for maximum field enhancement  $|E|/|E_0|$  were a small gap distance between tip and particle as well as a laser excitation directly from the side. More precisely, maximum enhancement appeared with a laser polarisation parallel to the tip's long axis and a  $k$ -vector perpendicular to the tip's long axis. One could achieve orders of magnitude higher field enhancement by optimising these two parameters. Furthermore, they also note that the nanoparticle size as well as the tip apex angle only influence the electrical field enhancement  $|E|/|E_0|$  by a factor of below two.

FEM simulations for a conical gold tip in proximity to a dielectric surface in air and water were performed by Downes et al. [71]. They reported that the enhanced electrical field is extremely localised for a tip with a radius of 20 nm and p-polarised excitation. This translated to a lateral resolution in the range of 1 nm for tip-enhanced Raman experiments. A red shift for aqueous environments was noted. The electrical field enhancement was found to be in the order of  $10^3$  for a 1 nm gap, yielding an enhancement in the order of  $10^{12}$  for elastic scattering, which would allow for especially short Raman signal acquisition times. Thus, it was concluded that molecular resolution and high speed Raman imaging with a gap below 4 nm should be possible for such a system.

A 3D finite difference time domain calculation was performed by Roth et al. [72]. In this work a conical gold tip at a distance  $d$  above a gold substrate, which was excited from the side with a p-polarised laser of 633 nm wavelength under a polar angle  $\theta$ , was modelled. Maxwell's equations were solved by discretising space as well as time and using a Drude dielectric function to describe the optical properties of the tip. Variations of  $d$  and  $\theta$  were performed. It was reported that the  $E_z$  component of the locally enhanced electrical field dominated the  $E_x$  component for each simulated case. Furthermore, the gap distance had a strong influence on the result, and the field enhancement dropped drastically with increasing  $d$ . On the other hand, the influence of  $\theta$  was only minor, and an optimum value for maximum field enhancement of  $45^\circ$  was reported. Finally, by exciting the tip using a laser pulse with a finite spectral width and evaluating the near-field response using a Fourier transform the plasmon-resonance modes of the tip could be investigated. Here, several resonance modes were visible converging against a wavelength of 194.3 nm, below which the optical frequencies would exceed the plasma frequency of gold.

A study to investigate the TER signal dependency on the excitation laser's polarisation was performed by Ossikovski et al. [73]. A closed analytical model, known

from SERS calculations, which can be solved numerically was reported, and a quantitative comparison of the results to experimental TERS measurements of phonon bands in crystalline silicon was made. It was noted that an adequate quantitative model is of particular importance for investigations of intrinsic stress in silicon and molecular detection.

A closely related TERS study to the work at hand was contributed by Johnson et al. using a FEM simulation [53]. They calculated the backward radiation efficiency for pyramidal gold tips as a function of the tip's apex angle in a transmission TERS set-up. An increase of an order of magnitude for a tip apex angle of  $70^\circ$  in comparison to an apex angle of  $15^\circ$  was reported. Thus, they concluded that for transmission set-ups pyramidal tips show superior TERS performance.

In summary, each one of the discussed works presented a calculation model tailored to address the questions at hand. While some of the acquired knowledge is certainly true for similar systems, e.g. the fact that the field enhancement in TERS is facilitated by a small gap distance between tip and metal substrate, the exact influence of a parameter for a distinct system stays unclear. For this reason, it was necessary to develop a calculation model tailored to the tip geometry and excitation conditions which were dealt with in the course of this work.

The aim of the calculation model in this work was to investigate the influence of the incident direction of the excitation laser beam on the tip. This was of particular interest, because the azimuthal angle  $\varphi$  and polar angle  $\theta$  could not be controlled in an absolutely precise way during tip fabrication and in the experimental set-up. Furthermore, it was important to receive information about the influence of the tip radius and the tip apex angle on the TERS performance. The latter was of significance to estimate how far the geometrical properties had to be optimised before finalising the fabrication.

Figure 6.1 shows the resulting absolute electrical field  $|E|$  for a calculation using the standard geometrical parameter set of  $\varphi = 0^\circ$ ,  $\theta = -30^\circ$ ,  $\alpha = 70.5^\circ$  and  $r = 25$  nm. In this configuration, a high electrical field at the apex of the tip was generated. With the standard parameter set, a maximum field enhancement of a factor of 4.65 in 2.5 nm distance to the tip gold surface with respect to the excitation could be evaluated. More importantly, no field excitation at the base of the pyramid or artificial scattering effects from the borders of the calculation volume were observed. This supports the conclusion that a model yielding physically reasonable solutions was generated. Due to the high electrical field around the tip of the pyramid, the excitation beam is hardly visible in the colour scaling. Although using a different excitation, the calculated field distribution resembles similar results already reported in [70] for related structures.

The graphs depicted in Figure 6.2 show the results for the variation of the four different parameters. After each calculation, the modulus of the electrical near-field was evaluated 2.5 nm below the tip and normalised to the modulus of the excitation field strength in the focus of the laser spot  $|E_0| = 1 \text{ V m}^{-1}$ .

On the upper left the results for the variation of the azimuthal angle  $\varphi$  are presented. Here, an angle of  $0^\circ$  corresponds to the situation that the  $k$ -vector of the excitation wave is in-plane to a vector perpendicular to a pyramid face and a vector along the pyramid height axis. On the other hand, an angle of  $45^\circ$  corresponds to

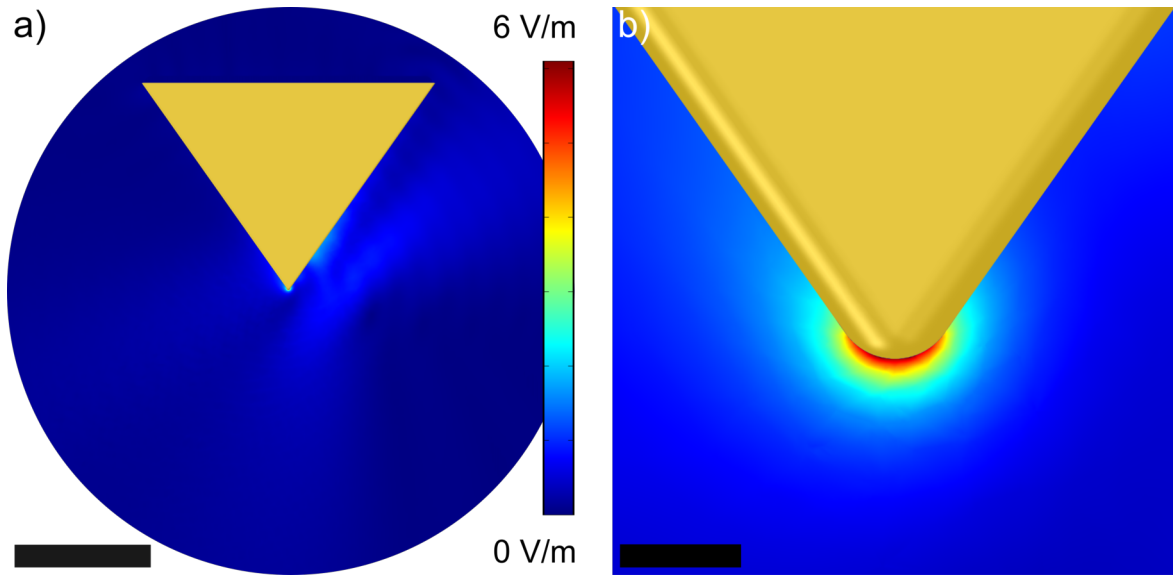


Figure 6.1.: a) Results for the simulation of a pyramidal tip using the standard parameter set of  $(\varphi, \theta, \alpha, r)$  (scale bar  $2 \mu\text{m}$ ). b) Magnification of the tip area (scale bar  $50 \text{ nm}$ ). In both cases the modulus of the electrical field is depicted by the colour scale from a).

the  $k$ -vector being in-plane to a vector parallel to a pyramid edge and a vector along the pyramid height axis (see chapter 4 section 4.1). For the field enhancement as a function of  $\varphi$  a near-monotonic decreasing relationship was found. This is supposed to originate from the specific geometrical planes of the different surface curvatures of the tip to the excitation. For  $\varphi = 45^\circ$  the electrical wave could couple directly to the forwards facing pyramid edge, reducing the near-field at the very tip. Another aspect could be the increase in reflection due to the inclined incidence on the flat surfaces. Yet, the effect of the azimuthal angle on the electrical near-field is limited. The enhancement factor varies in the range of 3.7 to 4.7.

The upper right panel of Figure 6.2 depicts the results for the variation of the polar angle  $\theta$ . An angle of  $-30^\circ$  refers to the configuration that the pyramid's symmetry axis is tilted in the direction of the incoming beam, while an angle of  $40^\circ$  represents the situation, that the pyramid's symmetry axis is tilted away from the incoming beam (see chapter 4 section 4.1). Interestingly, a maximum for the field enhancement was not found for  $\theta = 0^\circ$ , which could correspond to a localised surface plasmon or dipole mode as found in [72]. Instead, a maximum field enhancement for a coupling under an angle of  $-10^\circ$  was found, which is again supposed to correlate with the specific geometry of the tip. Hence, for a precise model a simple dipole approximation is insufficient and a more detailed description needed. However, in the relevant range of  $\theta$  from  $-30^\circ$  to  $10^\circ$ , which could be reliably achieved in the experiment, the absolute influence of the polar angle on the field enhancement is relatively small and varies below a fraction of  $\pm 10\%$ .

In the lower left panel the results for a variation of the apex angle  $\alpha$  of the tip are depicted. For the range of  $\alpha$  which was realised during this work, namely from  $70.5^\circ$  to around  $35^\circ$  depending on oxidation time, a near-constant, strong field enhance-

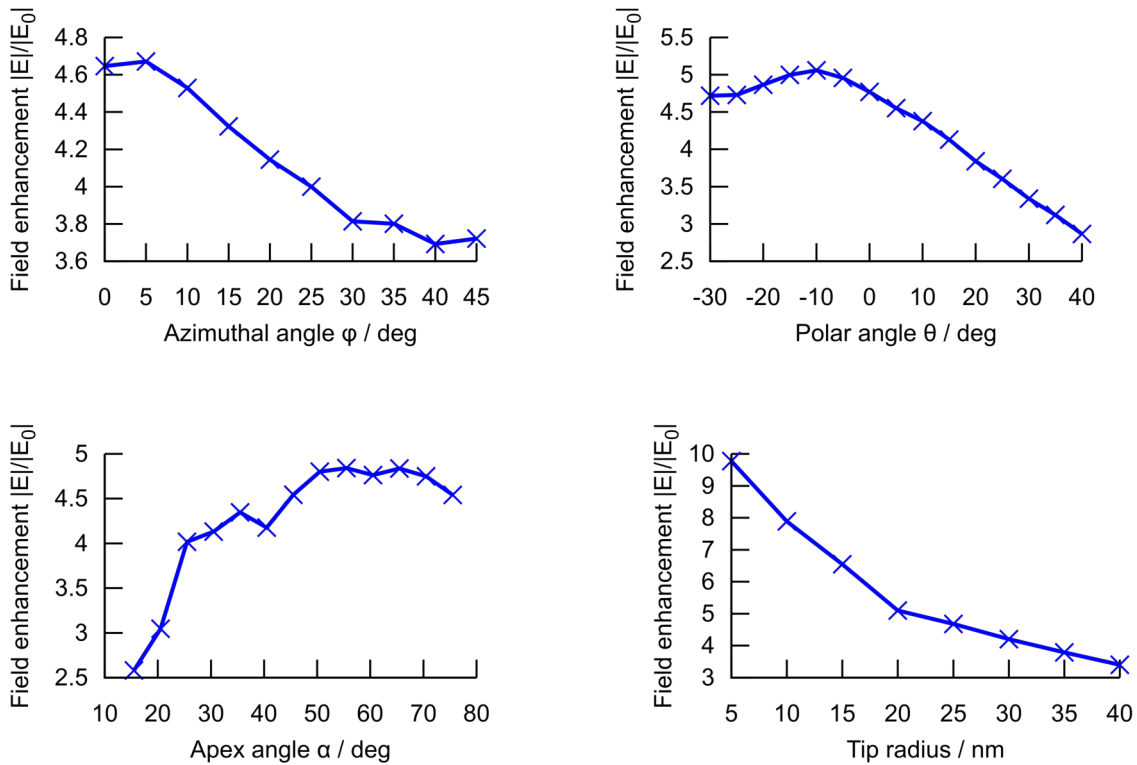


Figure 6.2.: Resulting field enhancement 2.5 nm below the tip for variations of the different parameters  $\varphi$ ,  $\theta$ ,  $\alpha$  and  $r$ . Attention should be paid to the differently scaled  $y$ -axes.

ment was found in the calculation. In contrast to the three other parameters, distinct features are visible in the graph. More precisely, at least one sharp decrease for the field enhancement was found at an apex angle of  $40.5^\circ$ , however, more calculation points are needed to verify this. It is supposed that this could originate from shifts of the structure's plasmon-resonances as a function of  $\alpha$ , which were investigated in literature [72] as a function of the apex radius by employing a time-domain calculation. Surprisingly, for angles below a value of around  $35^\circ$  a sharp drop in the field enhancement was found. The effect could be related to the effective reduction of gold volume and surface in the beam spot. Simply, this relates to a reduction of the available electrons for plasmonic excitation. A similar observation was also reported in [70] and is subject to present discussions and research. Yet, beside the field enhancement of the tip another important characteristic for TERS probes is the spatial confinement of the electrical field, which translates to lateral resolution. Therefore, a sharp tip might still be beneficial, although it comes at the price of lower signal intensity.

Finally, in the lower right panel of Figure 6.2 the results for a variation of the tip radius are depicted. The graph reflects the expected behaviour, a monotonically decreasing function for larger tip radii. Firstly, smaller tip radii correlate to greater curvatures and thus stronger coupling. Secondly, a smaller tip radius confines the electrical field and yields increased field density, often referred to as lightning-rod

effect [74]. Following from this evaluation, the tip radius was found to be the most influential parameter for the electrical field enhancement, yielding a factor of close to 10 for the electrical field enhancement, and thus around four orders of magnitude higher signal intensity for TERS. Again, a sharp tip is not only beneficial for absolute field enhancement, but also needed for spatial resolution.

So far, only the free tip was modelled, yielding a field enhancement originating supposedly from the excitation of LSP and SPP modes. In a next simulation, a large gold sphere was introduced and located at 5 nm distance below the tip. Due to its small curvature, local field enhancement just by the sphere itself was negligible. Figure 6.3 shows the results for these simulation conditions. In this case, the field enhancement between the two structures was found to be a factor of 4 to 6 higher compared to the free tip. Furthermore, a stronger spatial confinement of the electrical field as compared to the free tip was found. It could be interpreted that a new gap-mode is excited, which is dominating in this configuration. Hence, in terms of Raman signal intensity an additional factor of over 600 could be expected for the enhancement compared to the free tip, when imaging in proximity to a gold surface (as is the case in STM feedback).

Next, variations of the parameters  $\varphi$ ,  $\theta$ ,  $\alpha$  and  $r$  were performed as before for the tip alone. Figure 6.4 shows the calculated results for the field enhancement 2.5 nm below the tip. In general, all four curves show a similar shape as before in the simulation without the extended sphere below. While not only the shape is preserved, also the ratios between the maximum and minimum values are comparable. On the other hand, in all graphs the absolute enhancement is around a factor of 4 to 6

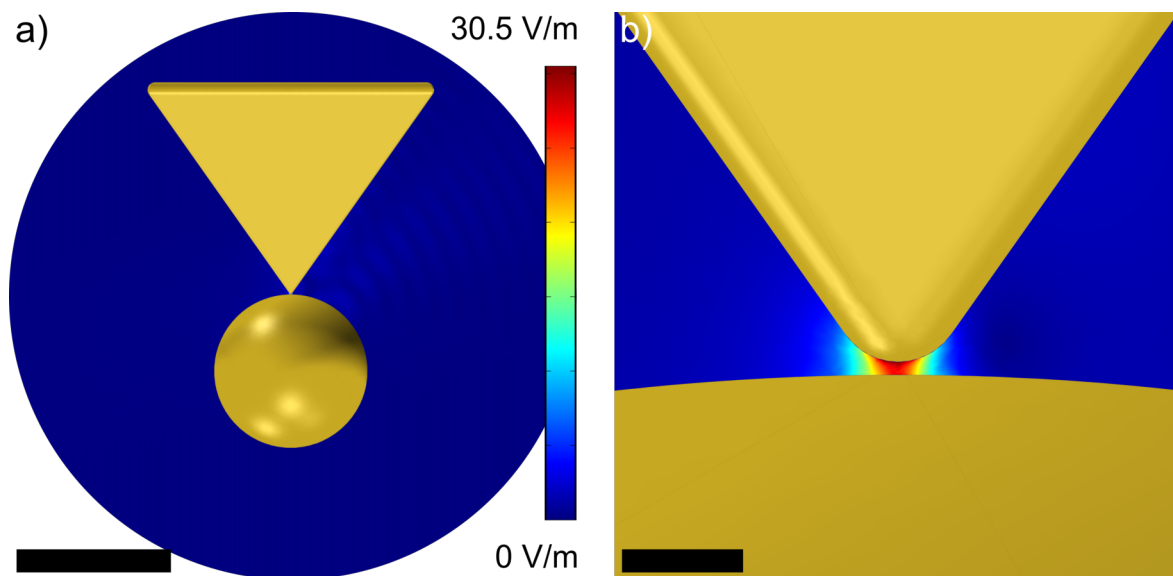


Figure 6.3.: a) Results for the combination of a pyramidal tip using the standard parameter set ( $\varphi$ ,  $\theta$ ,  $\alpha$ ,  $r$ ) and a 2  $\mu\text{m}$  diameter gold sphere located with a 5 nm gap below the tip (scale bar 2  $\mu\text{m}$ ). b) Magnification of the gap area (scale bar 50 nm). In both cases the modulus of the electrical field is depicted by the colour scale from a).

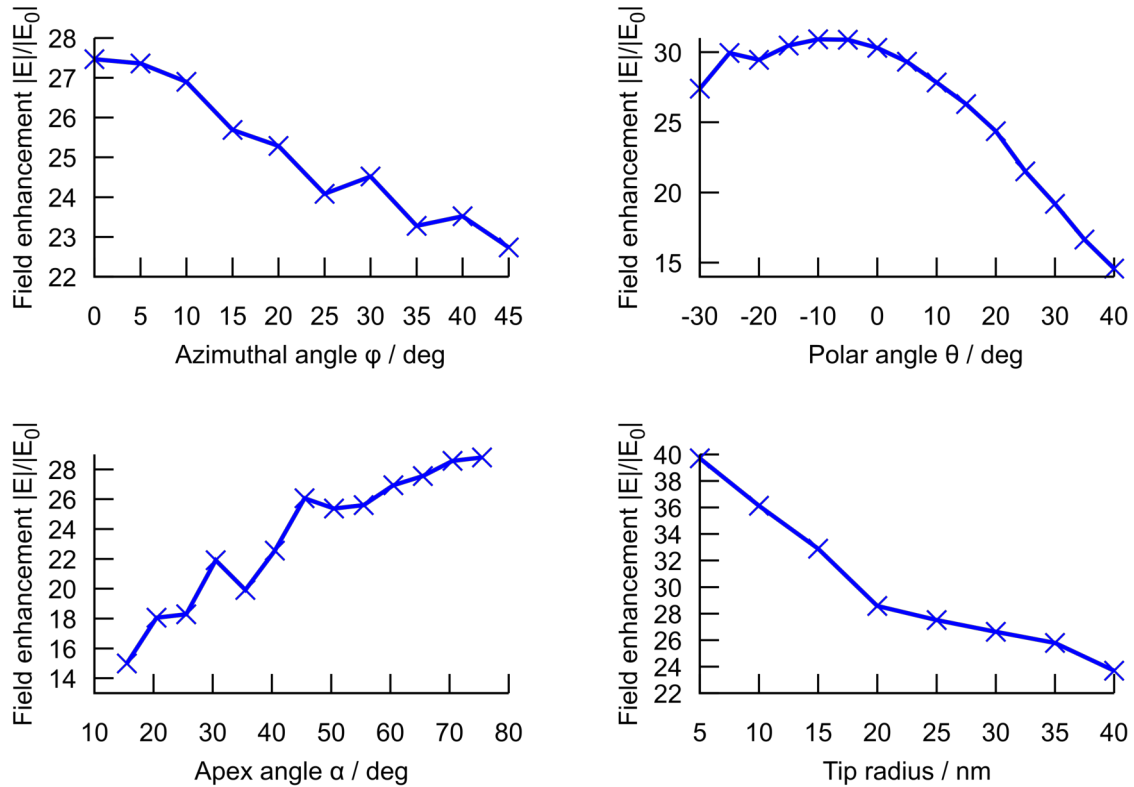


Figure 6.4.: Resulting field enhancement in the middle between a gold tip and a  $2\ \mu\text{m}$  gold sphere, separated by a distance of 5 nm, for variations of the different parameters  $\varphi$ ,  $\theta$ ,  $\alpha$  and  $r$ . Attention should be paid to the differently scaled  $y$ -axes.

higher than in the case treated before. Furthermore, in the graphs for the variation of  $\varphi$  and  $\theta$  several features are visible, which were not observed before. However, a finer binning of the variation steps would be necessary to reveal the detailed shapes and investigate their origins.

As a result, it was concluded that the higher enhancement originates from the excitation of plasmons in the metal tip and sphere, yielding a gap-mode and an amplification of the near-fields between the two metal structures. Surprisingly, this mode cannot be treated independently of the shape of the pyramidal tip, since the field enhancement shows a similar dependency on the varied parameters as in the case of the free tip. Thus, the stronger field enhancement with the gap-mode might not be interpreted as an additional plasmon mode, but as a modification of the previously observed LSP and SPP excitations. The available free (mirror) charges in the metal sphere could allow for an amplification of these excitations, while preserving the dependencies on the tip geometry and excitation conditions.

In summary, the plasmonic excitation of a pyramidal gold tip by an Gaussian p-polarised laser beam was modelled and simulated successfully. The dependency of the hotspot excitation strength on different parameters was investigated and revealed the tip radius to be the most influential one. Interestingly, small tip apex

angles were found to be only beneficial for TERS up to a certain degree, and a steep drop in field enhancement is found for angles below  $30^\circ$ . The excitation angles  $\varphi$  and  $\theta$  were found to have optimum values, which should be adjusted during the experiment as accurately as possible. Most interestingly, with the presence of a metal surface below the tip the parameter dependency was found to be preserved, although field enhancements of a factor of 4 to 6 higher than before were found. It was concluded that the previously observed near-field excitation was drastically enhanced due to the available free charges in the metal sphere surface, which could be excited comparable to mirror charges. /Note that only one parameter was varied at once, while the others were kept at the standard value. Thus, a change of several parameters at once could yield far stronger modification of the field enhancement than evaluated in the case at hand.

## 6.2. Silicon mould fabrication

The fabrication of high quality master substrates is the fundamental requirement for all moulding processes. Achieving defect-free structures and surfaces allows to replicate shapes of high congruence to the projected geometry, especially when features with the size of some ten nanometres are moulded. In this work, single crystalline silicon wafers were utilised to create master substrates, which offer best possible reproducibility and control. Furthermore, silicon technology is well-established, and a high amount of standard processes are available. In the following, several closely related articles are discussed.

In 1993, Hegener et al. [75] proposed a method to fabricate exceptionally smooth metal surfaces and coined the term *template stripping* for this technique. A freshly cleaved mica substrate, which thus featured an atomically flat surface, was used as master substrate. Onto the mica, a thin layer of gold was evaporated by PVD. After this, the gold layer could be released by either mechanical or chemical stripping. Finally, STM measurements revealed that areas of up to  $(25\ \mu\text{m})^2$  size with a surface roughness of below  $3\ \text{\AA}$  were achieved.

Two decades later, template stripping found wide application for the fabrication of plasmonic structures [76]. The technique not only allowed to reproduce nanometre features in metal, but also to preserve smooth surfaces crucial for plasmon propagation. Mould fabrication reported by Nagpal et al. [77] as well as Im and Oh [54] utilised wet etching of silicon in potassium hydroxide to fabricate pyramidal cavities or wedged trenches. Furthermore, the formation of smooth surfaces combined with oxidation to achieve a further sharpening of the as-formed angles was reported. The mould could be metallised by standard metal evaporation processes, and arrays of structures could be peeled off by glueing a support substrate on top using an adhesive. Additionally, it was also possible to target and release single structures using a glueing step.

Recently, Hu et al. [78] reported a newly developed fabrication strategy for plasmonic nanostructures on flexible substrates utilising a special form of template stripping. In this work, aluminium foil coated with a gold layer was pressed against a silicon mould, structured by wet etching, and then covered by a glass slide. Afterwards, a  $0.7\ \text{GW cm}^{-2}$  pulsed laser was utilised to evaporate and ionise a sacrificial graphite layer on the backside of the aluminium foil. The expanding gas pressed the aluminium foil into the mould and thereby generated a replication of the structure in the gold layer. After separation, SERS measurements were successfully conducted using the fabricated gold structures.

### 6.2.1. Wet etching of pyramidal cavities in silicon

Anisotropic wet etching in potassium hydroxide was applied to structure the wafer substrate in this work. Thus, possible mask layers which are commonly used in such processes consist of silicon nitride or silicon dioxide. Besides their high compatibility to silicon surfaces with respect to adhesion and stress, both offer good resistance against potassium hydroxide and a defect-free layer deposition, and could be routinely structured by dry etching. However, the exact properties of both mask layers

strongly depend on the fabrication methods (PECVD, thermal oxidation, sputtering) and process parameters.

In the case of silicon nitride it was not possible to measure an etch rate for the etching conditions utilised in this work. However, it was observed that a 50 nm thick mask layer is not suitable and breaks down after around 30 min etching in potassium hydroxide, resulting in undefined etching over the whole substrate. This indicates that for such a thickness the layer was not completely closed, and underetching through defects resulted in a lift-off of the mask. Silicon nitride layers with 200 nm thickness and more were observed to be highly stable, and no defects occurred during etching for 6 h in 45 % KOH at 60 °C. For process compatibility with the local infrastructure, an established clean-room process for PECVD of a silicon nitride layer with a thickness of 600 nm was chosen for this mask material.

In the case of silicon oxide the etch rate was measured to  $(80 \pm 8) \text{ nm h}^{-1}$ . To ensure a successful masking, the layer thickness for the silicon oxide deposition was chosen to be twice the calculated value of the etched thickness during processing, using the following considerations. The largest structures with square bases of  $100 \mu\text{m} \cdot 100 \mu\text{m}$  yielded pyramidal cavities with self-limiting depths of  $35.3 \mu\text{m}$ . With respect to the silicon etch rate, which was measured to  $(15.1 \pm 0.1) \mu\text{m h}^{-1}$ , an etching time of 6 h is roughly three times longer than needed. However, since the cavities consist of stable {111} crystal sides, profound overetching allows to secure the formation of sharp, defect-free pyramidal shapes, while the depth does no further change after the inverse pyramid is formed. Thus, a thickness of  $1 \mu\text{m}$  was chosen for the silicon oxide mask layer and an etching time of 6 h.

Figure 6.5a shows a SEM image of a structured silicon nitride mask and the cavity after etching the underlying silicon in potassium hydroxide. The precipitation of residues on the freshly generated silicon surfaces was observed, as shown with higher magnification in the SEM image in Figure 6.5b. It was important to ensure that no masking of the silicon surface by the residues during wet etch took place, which could lead to defects and rough silicon surfaces. Furthermore, there are reports of residue formation of all kinds during silicon etching available [65], and the most closely related investigation that was found reported the precipitation of iron oxide when etching cavities in silicon [80]. An EDS analysis shown in Figure 6.5c yielded signals of a high content of iron as well as low amounts of copper from the residues. The oxygen signal originates presumably from oxidation states of the two metals because the spectrum was taken directly after wet etching and the formation of natural silicon oxide would have required more time.

With this knowledge, the substrates were immersed in 2 % hydrochloric acid in water for 2 h after etching, after which clean and smooth silicon surfaces, as depicted in Figure 6.5d, were achieved.

To investigate the correct formation of cavities, especially the tip features, SEM imaging in combination with FIB milling was utilised. Figure 6.6 shows an image of an etched cavity sliced open by a milled trench, and a high magnification image of the very tip. A  $1 \mu\text{m}$  thick layer of platinum was deposited in advance to avoid re-deposition artefacts on the surface of interest due to FIB milling. The geometrical properties of the structure were measured on several consecutive SEM images taken during FIB slicing of the very tip, and the error was calculated using

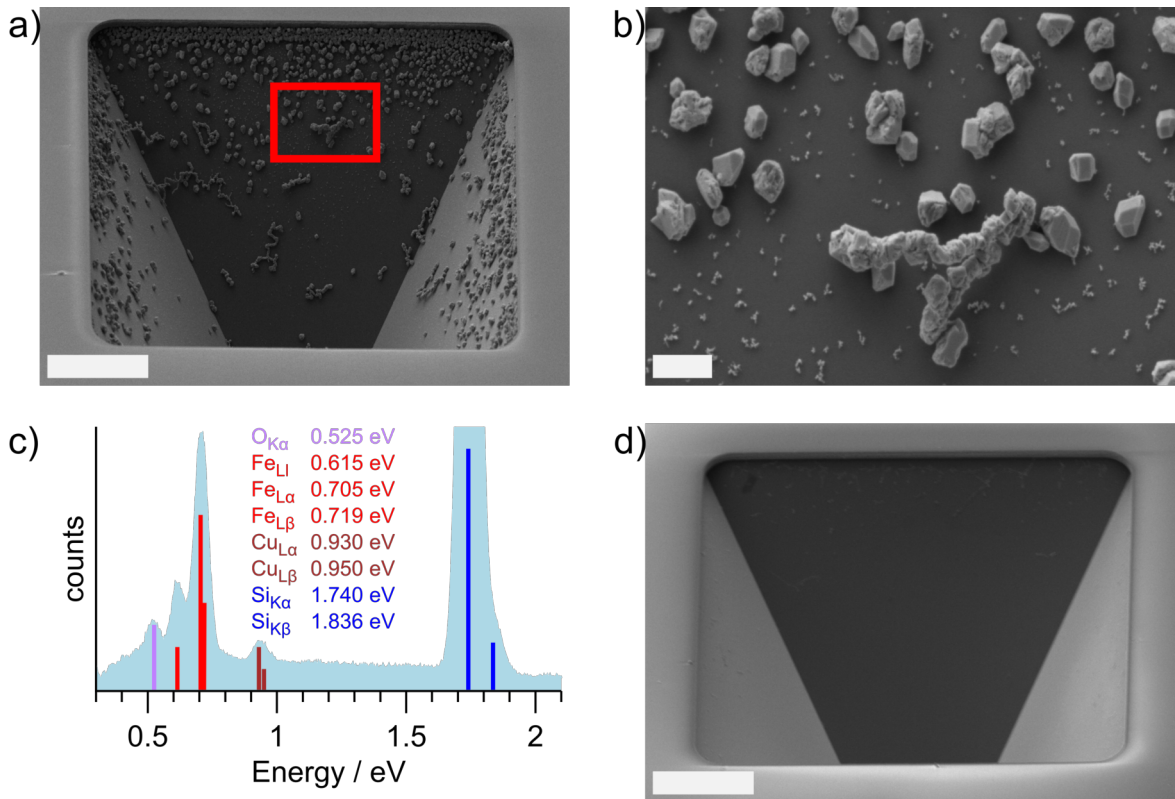


Figure 6.5.: a) Tilted SEM image of a silicon cavity after wet etching with visible residues on the surface (scale bar 10  $\mu\text{m}$ ). b) Tilted SEM image of the area marked in red in a). Residues show crystalline structure, and no masking defects of the silicon during etching are visible (scale bar 1  $\mu\text{m}$ ). c) EDS spectrum of the marked area in a) taken at 5 keV electron energy. The large silicon signal is truncated. X-Ray energies taken from [79]. d) Tilted SEM image of the etched cavity after treatment with 2% hydrochloric acid for 2 h (scale bar 10  $\mu\text{m}$ ).

the variance. The tip radius was measured to  $(24 \pm 4)$  nm and the angle was measured to  $(70.4 \pm 0.9)^\circ$  in accordance with the silicon lattice angle of  $70.5^\circ$ . Moulding this shape by a gold layer to yield a tip, without further oxidation, could have been already sufficient for TERS measurements.

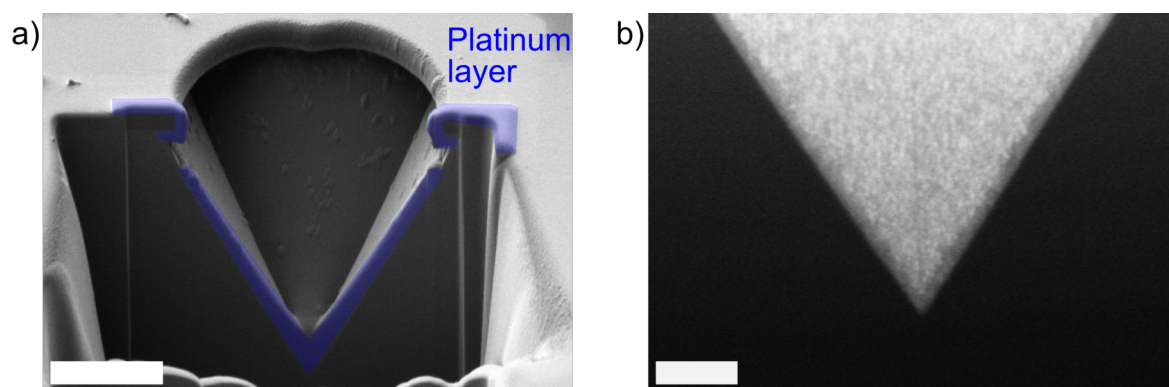


Figure 6.6.: a) A SEM overview image of the milled cavity showing the remains of the deposited platinum protection layer (scale bar 10  $\mu\text{m}$ ). b) High magnification SEM image of the very tip showing a tip angle of  $70.5^\circ$  and a sharp, nanoscale mould (scale bar 200 nm).

### 6.2.2. Oxidation and Metallisation

The oxidation of the fabricated silicon moulds served several purposes. Firstly, through oxidation a sharpening of the very tip in the cavity was expected [54, 81]. The reason for this is that silicon oxidises homogeneously over flat surfaces but depletes in regions of sharp features. Secondly, an oxidised silicon surface presented a defined state of the mould. After a wet etch step natural oxidation starts to occur and, depending on the time until further fabrication, the silicon surface changes. By oxidising of a defined amount of silicon, effects of natural oxidation can be neglected for far longer time spans. Finally, since it was planned to release metal structures from the mould, silicon oxide offers a lower surface energy than silicon and due to this lower adhesion forces.

A series of substrates was prepared and the oxidation time was varied to investigate the influence of the oxide thickness on the cavity geometry. Table 6.2.2 lists the various oxidation times as well as the calculated oxide thickness according to the Deal-Grove model [82]. This model describes the oxidation of a surface and takes into account the diffusion of oxygen into the bulk material, the diffusion through an existing oxide layer and the chemical reaction with the material. Further, the silicon volume expands during oxidation and the original surface plane is shifted outward, with 44 % of the generated silicon oxide being below and 56 % above the former silicon surface plane. The Deal-Grove model describes the oxidation of single crystalline silicon adequately, especially for oxide thicknesses above 25 nm, where no correction term is needed. Additionally, a ratio of 56 % of the total oxide thickness is calculated, which corresponds to the oxide thickness over the former silicon surface.

Oxidation time in h:mm	oxide thickness in nm	oxide above original surface in nm
1 : 02	18	10
2 : 24	36	20
3 : 55	54	30
5 : 36	71	40
9 : 26	107	60

Table 6.1.: Calculated oxidation time using the Deal-Grove model for a {111} silicon surface, an oxidation temperature of 900 °C, a dry oxidation process and a starting natural oxide thickness of 25 Å.

In the next step, a 5 µm thick gold layer was deposited with a deposition rate of  $(414 \pm 13) \text{ nm min}^{-1}$  with respect to a planar surface. It was found that peeling the gold layer off with tweezers, starting from one corner of the substrate, was the safest way to prepare the structures for release. This worked extremely well in the case of a silicon nitride mask, due to the large undercut formation of around 600 nm during the silicon wet etch. Lifting the gold layer off in 2 % hydrofluoric acid solution, as reported in [54], or in 2 % potassium hydroxide solution (limited to the case of a silicon oxide mask) was also possible. However, it was observed that during a wet lift-off the solutions infiltrated also in between the structures and the mould, etching

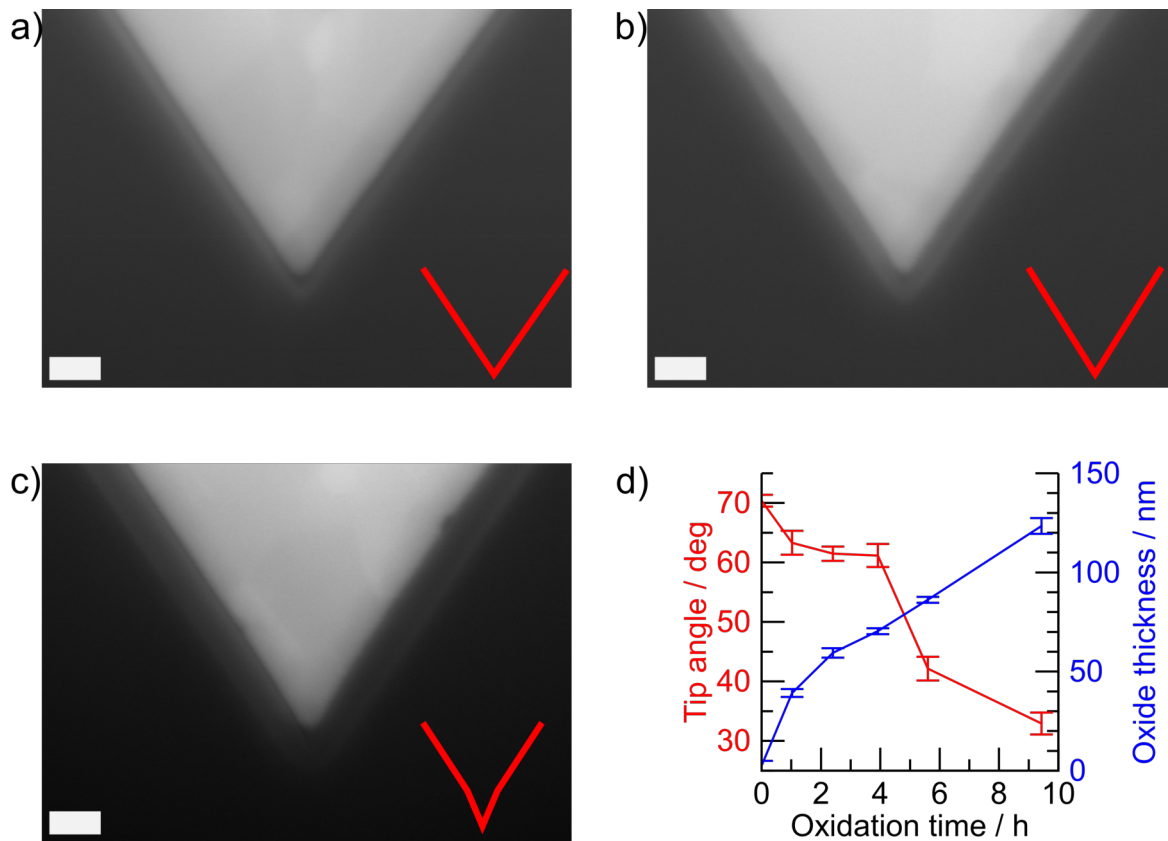


Figure 6.7.: Tilt-corrected FIB-SEM cross sections of the gold layer inside the moulds for three different oxidation times: a) 1 h 2 min, b) 5 h 36 min, c) 9 h 26 min. The red lines represent the respective measured oxide surface, scale bar 200 nm. d) Graph of the measured angle of the mould at the very tip for different oxidation times in red (left axis) and the measured total oxidation thickness in blue (right axis).

a small gap which could lead to mechanical damage of the structures.

Once more combined FIB-SEM analysis was utilised to investigate the actual oxide thickness, the effect of oxide sharpening as well as the quality of the metallisation before release. Figures 6.7a-c show FIB-SEM cross sections of gold structures inside the mould for different oxidation times. The oxide is visible due to material and charge contrast and can be distinguished from the darker silicon and the bright gold. The measured oxide thicknesses are depicted in Figure 6.7d and were found to be around 15 nm to 20 nm higher than the calculated values. This could originate from a wrong assumption for the starting oxide thickness in the calculation or the mismatch of the Deal-Grove model for thin layers. Further, the influence of the furnace is unknown, especially the time needed to flush out the oxygen after the oxidation and during the cooling down. However, the measured values were regarded as a future calibration curve for the furnace.

In addition, the images allowed to measure the tip angle, which was sharper than the standard silicon angle of  $70.5^\circ$  between  $\{111\}$  planes. It was observed that by oxidation an angle of  $63.3^\circ$  for the thinnest oxide to an angle of  $32.9^\circ$  for the thickest

oxide was achieved, see Figure 6.7d. Especially for the thicker oxide layers it was monitored that a strong sharpening of the mould occurred.

Furthermore, it was observed that the cross section of the polycrystalline gold shows crystalline areas in the range of  $1 \mu\text{m}^2$ . Often a single crystalline area at the very tip could be determined, which is beneficial to plasmonic activity. It was already observed that nanoparticles, which were thermally annealed to increase the crystalline domains and decrease the amount of grain boundaries, showed an improved LSP resonance [83]. Although the same study noted a decrease of SERS activity, the latter could be correlated with the surface roughness, which represented the origin of hotspots, vital for SERS, and was decreased due to thermal treatment. It was noted that a reduction of grain boundaries led to reduced damping and this improved the dielectric properties.

In this work, the large crystalline area formation could be attributed to the sputter process parameters, which yielded gold atoms with high energy and thus high surface mobility, which increased their probability to arrange themselves in a crystal lattice. Finally the gold layer visually featured a smooth coverage of the whole mould. Yet, the existence of holes or defects at the very tip was regularly observed, as depicted in Figure 6.8a. The reason for this could be the high deposition rate of the sputter process, which plugged the mould before the sharp features at the end were filled-out. Yet, it was already possible to recognise gold structures with tip features in the range of some ten nanometres, even with incomplete filling.

An oxidised mould was metallised by gold evaporation instead of sputtering to obtain additional insight in the hole or defect formation. During the evaporation process, the deposition rate was intentionally kept at a low value of  $0.2 \text{ \AA s}^{-1}$  until 20 nm were deposited. Such deposition parameters were also reported in [54]. Afterwards, the remaining gold was evaporated at a higher rate of  $2 \text{ \AA s}^{-1}$ . Figure 6.8b shows a cross section of the resulting metal structure. One could immediately recognise a filling of the mould until the very tip without holes or defects. On the other hand, the deposited gold layer showed a smaller crystal size in comparison to the sputtered gold layer, depicted and amplified in Figure 6.8a, and thicker layers could have only been achieved by either modifying the evaporation system or trying to sputter more gold on top in a second process afterwards. The latter would also have required to add some additional adhesion metal, like chromium or titanium. Thus, to keep the process batch fabrication compatible and to utilise the large crystalline domain formation, sputter deposition was kept as the method of choice.

Measuring the exact tip radius within reasonable errors could not be achieved at this stage of the fabrication process due to not being able to recognise when the cross-section including the lowest point of the tip was reached during milling. FIB-SEM analytics is a limiting factor, since the milling increment is in the range of 20 nm, which was expected to be in the range of the tip radius itself. Also, the necessarily low electron energy of 1 keV for imaging limited the lateral resolution of the SEM during FIB milling. For these reasons, the exact tip radii resulting from the different oxidation conditions were measured later, after the release of the structures.

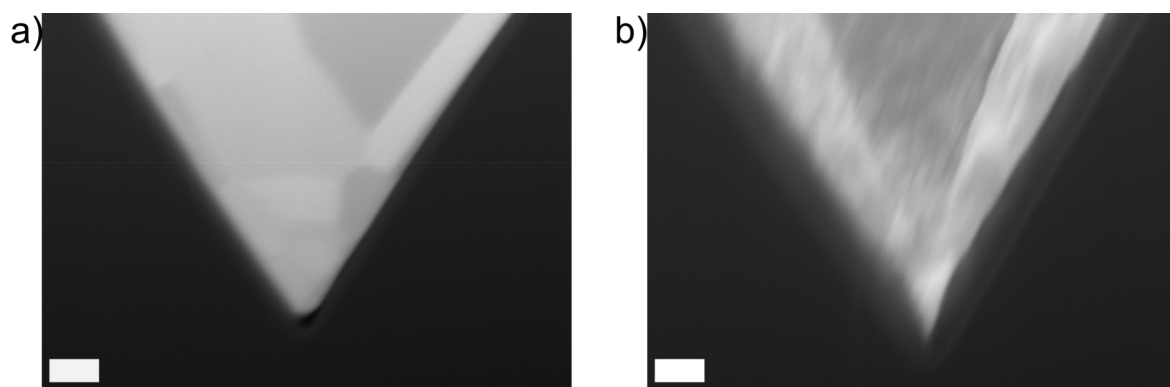


Figure 6.8.: a) Sputtered gold, note the cavity due to incomplete filling at the tip and the large crystalline areas in comparison. (scale bar 200 nm). b) Evaporated gold showing complete filling of the mould, but lower layer thickness and crystallinity were achieved (scale bar 200 nm).

## 6.3. Fabrication of STM TERS probes

In this section the results of the structure release and the analytical characterisation of the final STM TERS tips are described and discussed. A process for damage-free release is necessary to utilise single moulded structures as SPM probes. The practical extraction of metal microstructures with features in the nanometre range was the challenging task at hand. Furthermore, reproducibility and stability of the process were vital for batch fabrication. After release, the tips had to be attached to a SPM-compatible adapter or should be directly usable in SPM set-ups.

Bonding of plasmonically active structure to wires for SPM application was already reported by Kalkbrenner et al. [47]. For this purpose, a diluted solution containing 50 nm to 100 nm large gold particles was spin-coated on a substrate to yield a coverage below a monolayer. After imaging with confocal microscopy, a polyethylenimine covered optical fibre was approached to a single particle with shear force feedback until adhesion was achieved. The wire with the particle was then applied as a SNOM probe to image a structured aluminium film with a lateral resolution of around 100 nm.

A process to bond and form a self-similar trimer chain of gold particles on a quartz tip was reported by Höppener et al. [44]. Briefly, gold nanoparticles were dispersed on a substrate, imaged in shear force feedback with a quartz tip, and then a single particle was picked up by the tip. Repeated functionalisation with linker molecules of the tip and pick-up processes allowed to stack three particles of 80 nm, 40 nm and 20 nm while the linker molecules prevented metallic contact in between. Using the fabricated antennnas, strong near-field fluorescence images of single molecules could be recorded, supporting the theory of cascaded field enhancement for such kinds of structures.

Highly related to the present work, bonding of pyramidal metal structures to a wire and subsequent release was reported by Johnson et al. [53]. Single metal structures could be released from a mould by approaching them with a droplet of adhesive at the end of a tungsten wire utilising a micrometre stage for position control. After drying, the glued structure could be released damage-free in a straight upward motion, and the probes could be then directly used in shear force microscopy and therefore in TERS. Thus, high resolution near-field fluorescence images of immobilised Atto 647N dye molecules were recorded. Later, Jose et al. [84] reported an improvement of this process using a conductive adhesive. These tips were used in an aqueous environment and could immobilise single 190 nm sized particles as well as single-walled carbon nanotubes by dielectrophoretic trapping in the enhanced electrical near-field.

### 6.3.1. Bonding and Release

In this work, a bonding process utilising a ball bonder to release and electrically contact the pyramidal gold structures in one step was developed. The idea resulted from the thoughts that a ball bonder's movement takes place in a straight vertical line with respect to the substrate surface, that a metal-metal bond provides electrical contact as well as mechanical stability, that high reproducibility can be achieved, and

that a gold ball is the ideal structure to connect to a pyramidal cavity.

The tunable parameters of this process were the bonding force, ball size, substrate temperature, bonding time and ultrasound strength. Of these variables, the bonding force was found to be the most critical parameter of the process. It was observed that a too high force impressed the bond ball fully into the pyramid and damaged the side walls as well as the tip. A too low bond force caused insufficient adhesion, which either was not enough to release the structure afterwards or resulted in partial bonding and an undefined release, which was found to not guarantee a damage-free tip. It was found that for bonding balls with diameters of 80  $\mu\text{m}$  or 100  $\mu\text{m}$  targeting moulds with side lengths of 40  $\mu\text{m}$  or 60  $\mu\text{m}$ , respectively, a force of 0.8 N allowed for a consistent and reproducible release process. Following from this, the ball size was always chosen to be larger than the lateral diagonal of the targeted mould, ensuring maximal bond contact to the metal structure.

A higher substrate temperature was found to support gold-gold bonding, while the temperature was always kept below 250  $^{\circ}\text{C}$  to avoid any bond formation between structures and mould, especially silicon-gold alloy formation. The latter is reported to melt at around 360  $^{\circ}\text{C}$  [85] while gold atom diffusion might occur before. However, such high temperatures were not needed since successful bonding was already achieved with mould temperatures between 150  $^{\circ}\text{C}$  and 250  $^{\circ}\text{C}$ .

The ultrasonic treatment during bonding was kept to a minimum level with respect to power and duration, since the application of ultrasound during wet release of the gold layer resulted in defects of the gold tips.

With utilisation of the bonder set-up for structure release, cycle times of around 10 s were easily achieved, including ball formation, lateral alignment, the bonding step and separation. Such durations are far lower than for processes relying on bonding with liquid adhesives, which usually take several minutes or tens of minutes for curing. Furthermore, vertical release and high orientation of the structures on the support wire were inherently ensured by the process. Finally, excellent electrical conductivity between wire and tip was another given feature.

It was found that glueing the tips to an SPM adapter piece was the most practical way to proceed while the bonded structure was still attached to the continuous bonder wire. Utilising a helping hand<sup>1</sup> allowed for precisely positioning the adapter piece relative to the wire with the structure. In advance, a droplet of fast-curing silver glue was deposited on the adapter's v-shape, as it can be seen in Figure 6.9a. After drying, the gold wire was cut by scissors, and the final STM TERS probe was released from the jig. Figure 6.9a shows an optical image of a released structure bonded to a wire and attached to the adapter plate. In Figure 6.9b a magnification of the attached wire is depicted, in which the pyramidal tip below the bonding ball can be seen.

Also, 40  $\mu\text{m}$  based pyramidal metal structures were bonded and released for analytical characterisation, allowing for reasonable FIB milling times. These structures on wires were not attached to an adapter piece, but directly glued to SEM stub holders using adhesive carbon discs.

---

<sup>1</sup>A highly adjustable jig attached to a weighted base.

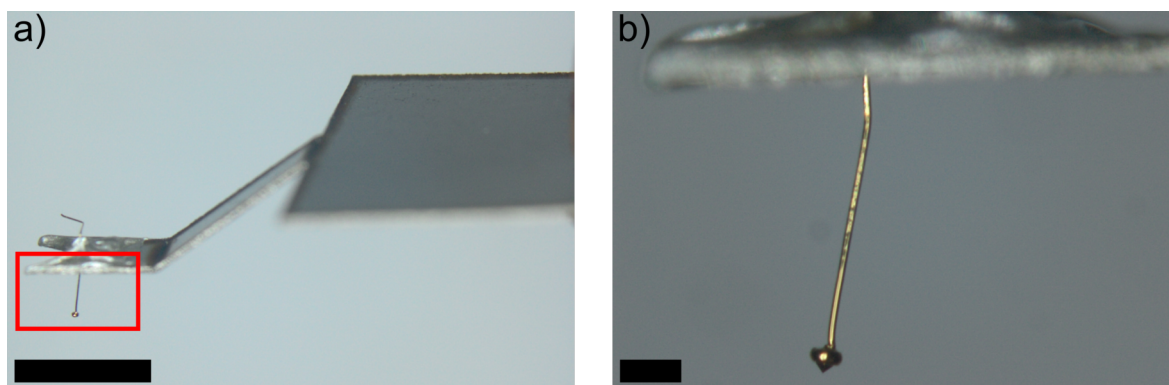


Figure 6.9.: a) Stereo light microscopy image of the front part of a SPM adapter piece with an attached TERS tip (scale bar 2 mm). b) Magnification of the area marked in red in image a) (scale bar 200  $\mu\text{m}$ ).

### 6.3.2. Analytical Characterisation

The geometrical features of the produced TERS tips were evaluated by SEM imaging. In particular, the correlation between the oxidation thickness and the tip apex radius was of interest. Furthermore, the surface topography and the defect rate of the bonding process were investigated.

For this purpose, the probes fabricated for analytic characterisation were mounted in an SEM, and the whole stage was tilted by  $54^\circ$ . Subsequently, by rotating the sample holder, at least one position could be found at which the electron beam is parallel to the pyramid base and the flat bond ball surface. Figure 6.10a shows a SEM image acquired from one of the tips in this position. A maximum possible electron energy of 30 keV and a magnification of  $10^5\times$  were chosen to achieve high resolution imaging of the tip apex. In total, ten tips each for an oxidation time of 3 h 55 min, 5 h 36 min and 9 h 26 min were analysed.

Figure 6.10b and c show typical high magnification images of tip apexes for the thinnest oxidation and the thickest oxidation, respectively. While in the first case only a tip radius of around 80 nm is achieved, the second image shows a tip with a radius below 20 nm. Furthermore, in both images smooth metal surfaces on the pyramid sides can be found, while the edges show a rougher structure. This is assumed to be the consequence of the oxide sharpening, which not only happened at the tip, but also in the edges of the mould. Interestingly, no apex angles of the structures in the range of  $30^\circ$  were observed as described in [54]. However, as mentioned earlier, this is correlated to the metal deposition process, where an incomplete filling of the mould was observed. Still, good TERS performance from such probes is expected, especially when considering the results from the computational simulation, where extremely sharp apex angles were found to be less favourable for tip enhancement than larger apex angles. Consequently, the structures fabricated here with small apex radii and large apex angles might be the favourable geometry for field enhancement. As a side note, carbon deposition was observed during SEM imaging, e.g. visible as a bright veil over the structure in Figure 6.10c. This deposition did not interfere with SEM measurements, however, TERS application of such

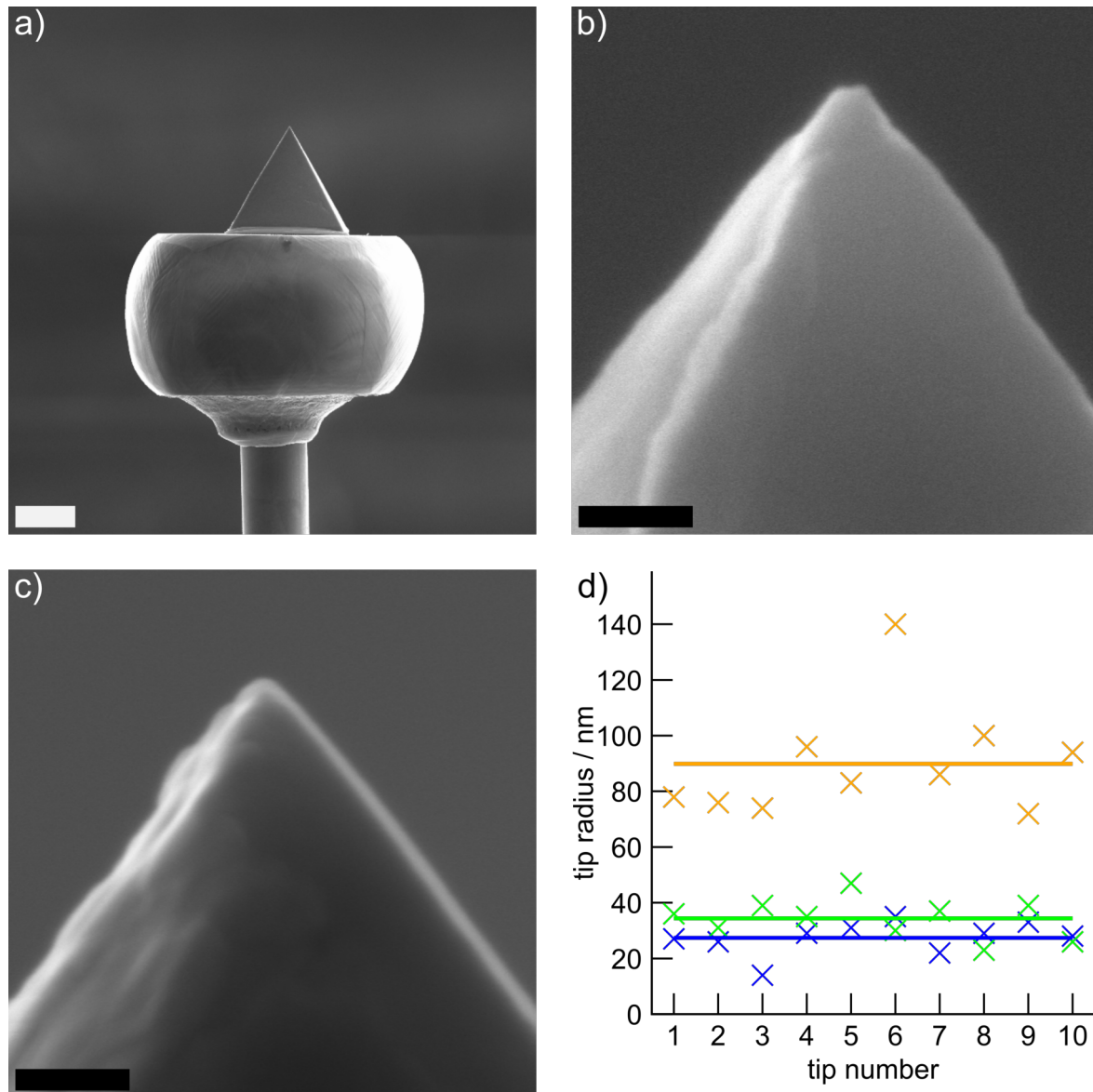


Figure 6.10.: a) SEM image of a bonded pyramidal tip aligned perpendicular to the electron beam for tip radius measurement (scale bar  $20\ \mu\text{m}$ ). b) High magnification image of a pyramidal tip released from a mould with a thinner oxidation layer (scale bar  $200\ \text{nm}$ ). c) High magnification image of a pyramidal tip released from a mould with a thicker oxidation layer (scale bar  $200\ \text{nm}$ ). d) Measured tip radii for three sets of tips fabricated from differently oxidised moulds. The blue data corresponds to an oxide thickness of  $121\ \text{nm}$ , the green data to  $86\ \text{nm}$  and the yellow data to  $70\ \text{nm}$ .

contaminated structures after imaging should not be considered.

Figure 6.10d shows the measurement results of the tip radius for the three different sets of mould oxidation. Clearly, the thicker oxide mould yielded sharper tips compared to the thinner oxide. Moulds with the thickest oxidation yielded an aver-

age tip radius of  $(27 \pm 6)$  nm, slightly better than for the second thickest oxide where an average radius of  $(34 \pm 7)$  nm was realised. The thinner oxide led to an average radius of  $(90 \pm 19)$  nm. Comparable to the mould angles observed in the chapter before, the two thickest oxidations were found to clearly yield a sharper tip radius. This result allows to conclude that not the total oxide thickness, but the achieved cavity angle by oxidation sharpening was the deciding factor for the formation of sharp tips, even when a sputter metal deposition process was used.

Considering the fact that 19 out of 20 tips for the two thicker oxides yielded tip radii below 40 nm, a highly reproducible process to fabricate eligible structures for TERS was found. Furthermore, all 30 investigated tips showed a successfully moulded pyramidal structure and an intact bond to the wire, which further strengthened confidence in the release process.

However, from time to time during this work defective tips were observed. Yet, this was always already visible in light microscopy. One of the most common defects was an indented or damaged tip on the scale of some ten micrometres, which was accounted to handling mistakes. The second common defect was an incomplete bonding to the gold wire, which could be avoided after optimisation of the bonding parameters.

Finally, Figure 6.11 shows a FIB-SEM analysis of a bonded tip. In this case, a  $40 \mu\text{m}$  based pyramid was bonded to work with reasonable FIB milling times. Slicing was stopped as soon as half of the tip was removed. The SEM images were taken utilising an in-lens secondary electron detector to achieve higher topography contrast.

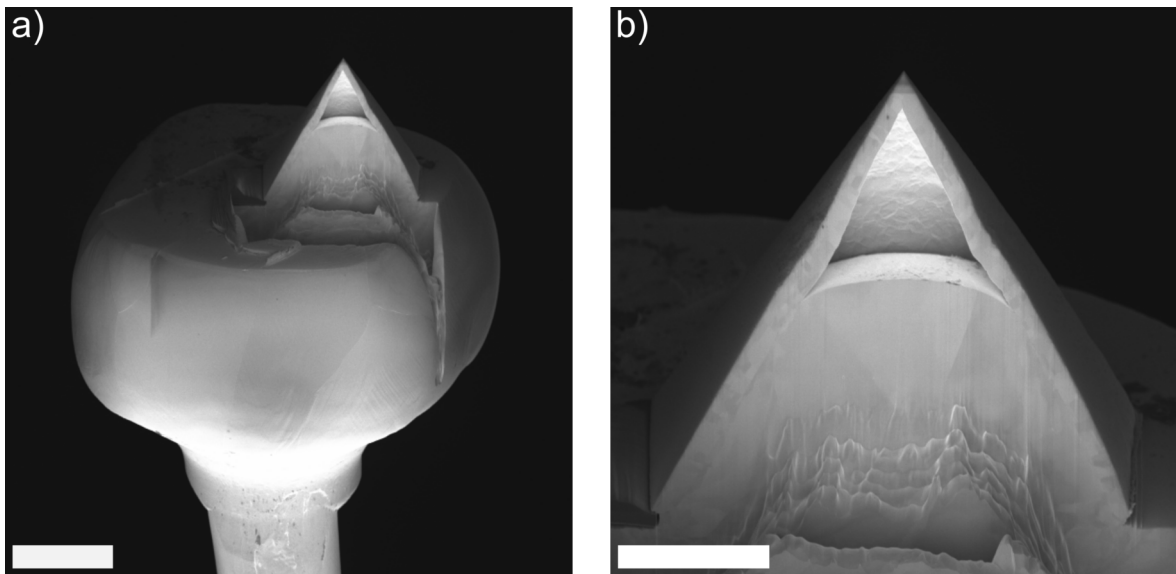


Figure 6.11.: a) SEM image of a FIB sliced pyramid released by ball bonding. An in-lens detector was used for increased topography contrast (scale bar  $20 \mu\text{m}$ ). b) Higher magnification image of the tip structure showing the gold pressed into the cavity, the metal-metal interface as well as the hollow pyramid volume in the upper third and the sharp tip (scale bar  $10 \mu\text{m}$ ).

It was observed that for metal structures of this size, two thirds of the pyramid height were filled with material from the gold ball during bonding. In general, this formed a gold-gold interface in close contact and explained the high mechanical stability and electric conductivity. A hollow part of the pyramidal structure in the upper half is clearly visible in the magnification image. Despite this weakness, no structural damage occurred during release, although the wall thickness of the pyramid is in the range of only 1  $\mu\text{m}$ . Once more, smooth surfaces on the outside of the structure were observed, in contrast to the surfaces inside the pyramid, which resembled the typical topography of sputtered gold.

## 6.4. Scanning tunnelling microscopy and tip-enhanced Raman spectroscopy

This section comprises the measurements performed with the fabricated STM TERS probes. Besides the investigation of interesting samples and sample-related questions, these measurements also served the characterisation of the tips. In the beginning, their STM properties were investigated on plain gold samples, followed by first tip-enhanced luminescence measurements. Next, the fabricated probes were applied to analyse samples covered by randomly distributed dye molecules and to investigate ultra-thin carbon layers. Finally, TERS measurement on nanometre thin PEDOT:PSS layers were performed to obtain insight into the layer homogeneity on the nano-scale. Before the results are presented, several related works performed by others are discussed.

Tip-enhanced Raman measurements using scanning tunnelling microscopy feedback for tip positioning were already performed for different sample materials and probe types. In 2002 and 2004, Pettinger et al. [86, 87] published results for measurements using electrochemically etched silver or gold tips. Strong TER signals from few molecules of nonresonant  $\text{CN}^-$  and resonant Brilliant cresyl blue on gold surfaces were reported [86]. Interestingly, for  $\text{CN}^-$  two bands were collected during TERS measurements. Previous knowledge from SERS measurements allowed to differentiate these into one mode corresponding to the adsorption on gold and the other to the adsorption on silver. This allowed to conclude that an adsorption of  $\text{CN}^-$  to the TERS tip occurred, underlining the difficulties of investigations on few molecules which are not immobilised. Furthermore, contrast factors, the ratio between the raw near-field and far-field signal, of 4 to 16 were calculated, neglecting the smaller excitation volume in TERS. Also, TERS measurements on resonant malachite green isothiocyanate using gold tips were performed [87]. An accelerated bleaching behaviour of the molecules during TERS was observed, which was attributed to the strong electrical field occurring below the tip. On the other hand, the intensity decrease during bleaching was used to evaluate the field enhancement factor by fitting a time constant, which is inversely proportional to the laser intensity. The ratio between far-field and near-field bleaching allowed to estimate a field enhancement factor  $g$  of 33, yielding an enhancement factor in the order of  $10^6$  for the Raman signal.

In 2012, Jiang et al. reported UHV-STM TERS measurements on adsorbed copper phthalocyanine (CuPc) layers on crystalline gold [88]. Although the utilised silver tip showed a tip radius of 130 nm, the experimental set-up allowed a precise positioning of the laser spot in the gap between tip and sample, leading to molecular resolution in TERS. The molecular TER spectra could be correlated to eight different vibrational modes of CuPc using density functional theory calculations. Furthermore, due to the highly defined sample composition and experimental set-up, an enhancement factor in the order of  $10^5$  was calculated, including a consideration of the excitation beam shape.

A study on the molecular resolution of TERS on  $\text{H}_2\text{TBPP}$  was performed in 2013 by Zhang et al. [89]. It was reported that spectral matching [90] of the tip to the

molecule is the critical factor for TERS intensity and that a smaller gap distance is further increasing the signal. Therefore, the nano-cavity plasmon profile is monitored by photo-luminescence excitation. In a low temperature UHV set-up, isolated single molecules were identified by STM measurements, and TERS spectra from different segments of the molecule could be acquired. Furthermore, spectra acquired from flat-lying and tilted single molecules were correlated to the matching FDT calculations.

Recently, Jiang et al. reported an UHV-STM TERS investigation of monolayers consisting of adsorbed PPDI<sup>2</sup> molecules on crystalline gold surfaces [91]. A separation of the monolayer into an ordered and a diffusion phase could clearly be imaged in STM and again resolved by TERS mapping with a spatial resolution of 4 nm. The reason for this was reported to be the molecular orientation dependant Raman signal of PPDI, which was calculated in time-dependant density functional theory simulations. The ordered phase was found to consist out of flat molecules parallel to the surface, while in the diffusion phase the molecules were oriented perpendicular to the surface, yielding a stronger signal. It was noted, that the defined direction of the electrical near-field between tip and sample, perpendicular to the surface, allowed for this observation.

### 6.4.1. STM imaging of a sputtered gold surface

Before diving into tip-enhanced Raman spectroscopy experiments, it should be ensured that the utilised probe is working properly in the chosen scanning feedback mode. This is especially important when unconventional SPM probes are fabricated and used, as it is the case in this work. Proper SPM imaging of the sample surface is of vital importance to guarantee that the tip is not damaged during scanning and that the tip-enhanced Raman spectroscopy results can be correlated to the sample surface.

Therefore, the first experiment was to apply the pyramidal probes to clean gold surfaces fabricated by sputter deposition, which is known to yield a surface with a roughness in the nanometre range. The images acquired with the probes were then compared to images acquired using a standard tungsten STM probe and to SEM images.

The scanning field size was chosen to be  $(1.28 \mu\text{m})^2$ , resulting in a  $(5 \text{ nm})^2$  pixel size when using 256 scan points and lines. The reason for this scan field size was the fact that STM is limited to smaller scan speeds than other SPM feedback modes, due to the extreme proximity of the tip to the surface. Furthermore, with an anticipated TERS resolution of some 10 nm, a scan in the micron range provided a typical section for further experiments.

Figure 6.12a and b shows typical STM scans from different surface positions acquired with one of the fabricated probes, and with a standard tungsten probe, respectively. In both cases, one can identify the surface topography of the gold layer, showing round-shaped grains in the range of 20 nm. A calculation of the root mean square roughness  $R$  yielded comparable values of  $R^{Au} = 1.9 \text{ nm}$  for the measure-

---

<sup>2</sup>N-N'-bis(2,6-diisopropylphenyl)-1,7-(4'-t-butylphenoxy)perylene-3,4:9,10-bis(dicarboximide)

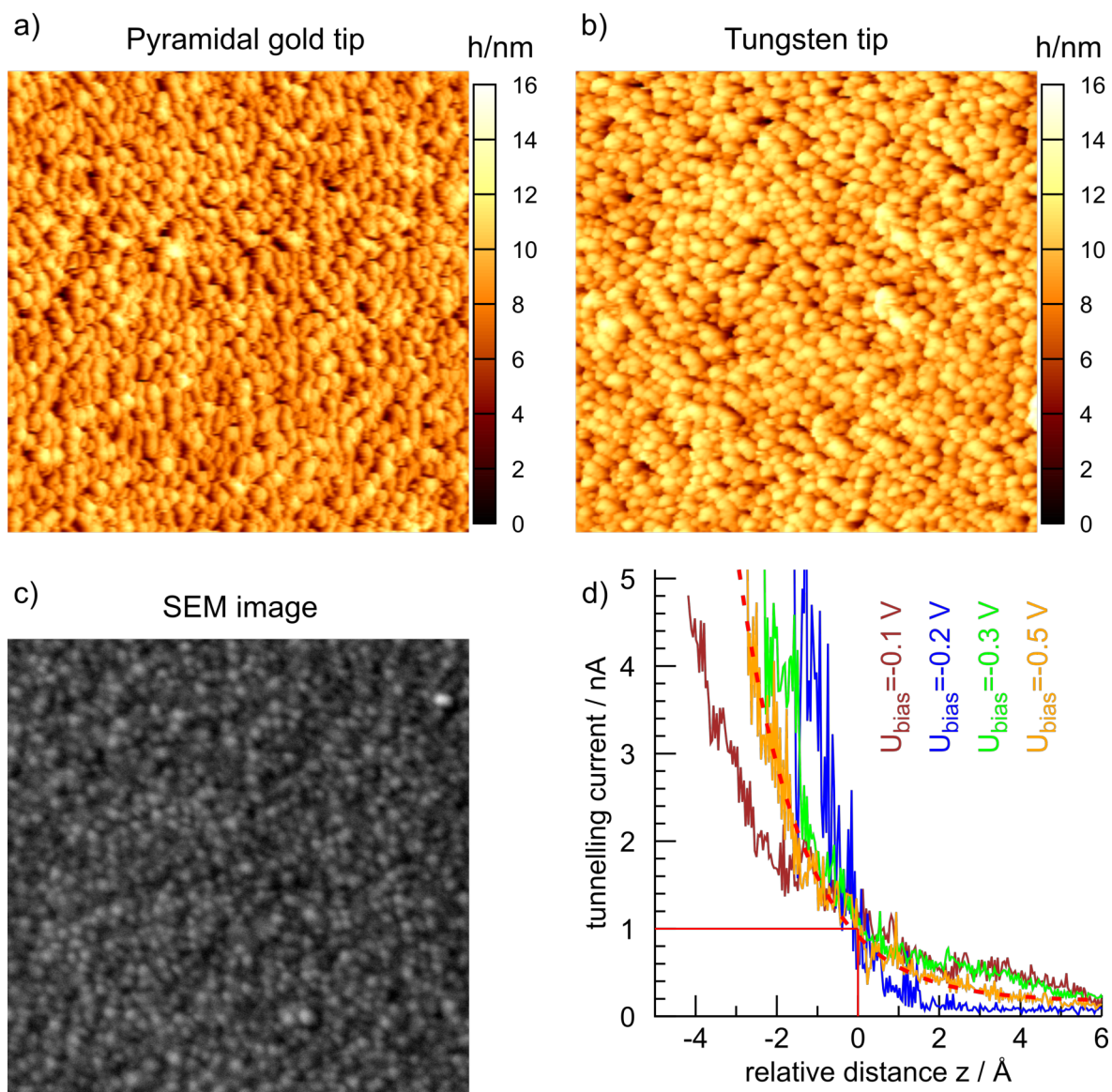


Figure 6.12.: a) STM image of a sputtered gold surface acquired with a fabricated pyramidal gold probe. b) Typical STM image of the same surface acquired with a standard tungsten probe. c) SEM image of the same surface. d) Typical tunnelling currents measured with the fabricated probes for different bias voltages. The dotted red line corresponds to a fit for calculation of the work function. Image sizes of a), b) and c) are  $(1.28 \mu\text{m})^2$ .

ment with the gold tip and  $R^W = 1.7 \text{ nm}$  for the measurement with the tungsten tip, respectively.

It was found that the tungsten tips could be operated with scan speeds of up to  $1.5 \mu\text{m s}^{-1}$  when using a PID setting of 2/0.1/0 and yielded high quality images. On the other hand, the fabricated gold probes required lower scan speeds of below  $500 \text{ nm s}^{-1}$  and an optimal PID setting of 2/0.5/0 for good imaging. Both the lower

scan speed and the higher integral contribution to the feedback control could be attributed to the thin gold wire to which the tips were attached. Although a sample scanner set-up is utilised, the low stiffness of the wire allows for small lateral deflections of the tip due to adhesion to the surface (water meniscus, van-der-Waals forces) when high scan speeds are employed. Slower scanning and a higher integral contribution to the PID feedback control prevented and smoothed out such deflections. On the other hand, the thicker and thus stiffer tungsten wire could be operated with a stronger proportional feedback control and thus higher scan speeds.

Figure 6.12c shows a control image taken from a different position by SEM, which confirmed that the imaged surface resembled the actual sample surface. Note that while the SEM image showed clearly round-shaped structures, both STM images tended to display more oval shapes. This could be attributed to drifting during the STM scans, which was facilitated by the long scan time, which was a consequence of the large scan area and the slow scan speeds. Here, an improvement is typically made by utilising an advanced stabilisation for the SPM, a controlled atmosphere or even UHV during scanning, and flat surfaced samples, which would allow for higher scan speeds. Yet, such a set-up was not available and would limit application of STM TERS to an even smaller set of samples.

Last, Figure 6.12d shows tunnel currents measured with a negatively biased pyramidal gold tip as a function of the perpendicular distance from its set point (tunnel current 1 nA, marked by a red line) for different voltages. These were performed with an approach speed of  $5 \text{ \AA s}^{-1}$  and a threshold of 5 nA, at which retraction was started. Retraction curves are not shown, but these displayed the characteristic hysteresis behaviour due to adhesion forces. For this experiment, it was found that bias voltages of 0.3 V and more led to stable, error-free approach curves. This value is higher than usual bias values reported in literature, which range down to 0.05 V. However, such values mostly correspond to samples of single crystalline gold surfaces and often UHV conditions, which allow for a more stable experimental closed-loop feedback and thus, smaller gap distances. For further analysis, the electron work function  $\Phi$  was calculated by fitting equation 3.2 (chapter 3 section 3.1) to seven curves measured with different tips and bias voltages below  $-0.3 \text{ V}$  at different points. As a result, values in the range of  $\Phi = 0.40 \text{ eV}$  were determined, which is an order of magnitude lower than the literature values of  $\Phi_{Au} = 5.10 \text{ eV}$  to  $6.16 \text{ eV}$  [92, 93]. However, these values usually correspond to calculation models of single crystalline gold surfaces in ultra-high vacuum with extremely low or no impurities at all. It is well known that surface roughness or single sharp features, as it was the case for the gold tips in this experiment, lower the local work function significantly. A deviation of the local work function of an order of magnitude from the bulk work function is in agreement with observations by others [94].

In summary, the fabricated tips were found to work reliably in STM feedback. Imaging of surfaces with features below 20 nm was achieved. In contrast to more specialised experimental set-ups, higher bias voltages and slower scan speeds were required. Yet, local work functions of the tips could be measured reproducibly and yielded anticipated results. A determination of the final achievable topography res-

olution is an open task, which has to be performed in the future and requires a suitable reference sample. However, the resolution was found to be at least in the range of the expected lateral TERS resolution, which was anticipated to be some ten nanometres. Thus, this should already allow for a meaningful correlation of surface topography and chemical information.

### 6.4.2. Near-field measurements on gold

After the STM compatibility of the fabricated probes was confirmed, the next logical step was to investigate their plasmonic capabilities. Although one does not expect to collect Raman spectra featuring distinct bands from a gold surface, the objective was to confirm the near-field activity of the tips in measuring increased luminescence. Additionally, a measurement on clean gold substrates should reduce the risk of contamination of the single probes and allow for further application to other samples of interest afterwards. Therefore, TER signals were collected following the procedure described in chapter 5 section 5.4.

Figure 6.13a depicts an optical image acquired through the Raman spectrometer coupling objective. It was found that the probe's shape together with the reflection from the sample surface allowed for a simple coarse alignment of the Raman laser relative to the very tip. This proved to be a huge advantage over commercially available TERS probes fabricated by wet etching of metal wires or metal-coated cantilevers, where it was found that the actual tip could often not be spotted precisely. In contrast to conventional tips, the fabricated probes feature smooth surfaces, yielding a contrast-rich optical image, and straight pyramid edges, guiding from the micron-scale structure to the nano-scale tip. For conventional tips, the rough alignment of the laser was found to be far more time intensive compared to probes fabricated in this work. After adjusting the laser, the precise hotspot was found by moving the focus point while the spectra acquisition was running. It was observed that there is typically a step-like increase in total signal intensity of at least an order of magnitude as soon as the hotspot is found. Then, the signal strength was further optimised by moving the laser spot in finer increments.

Figure 6.13b shows tip-enhanced Raman signals acquired using an extended scan with a laser power of 1 mW and 10 s accumulation time as well as a signal when the tip was retracted. Interestingly, it was found that beside a broad-band increase of the total signal, distinct bands appeared. It was supposed that these either originated from contamination of the gold substrate or from contamination of the freshly prepared tips. During investigation it was found that the appearing sharp bands changed, appeared or disappeared when the tip was moved as well as during continuous TERS signal acquisition. On the other hand, the broad-band signal increase over the whole spectrum was found to be present reliably. Secondly, when using a freshly prepared gold substrate, no or rarely similar sharp bands were detected. Hence, it was concluded that the origin of these bands were adsorbed molecules on the gold surface and not a contamination of the probe. Furthermore, from the measurements on clean gold substrates it was deduced that the release process yielded non-contaminated TERS probes and this allowed for the conclusion, that the silicon moulds had been pristine before metal deposition. In addition, it was found that a clean substrate had to be prepared a short time in advance, or the substrate has to be stored under clean conditions and atmosphere.

Due to the fact that a clean gold sample allowed for a stable near-field signal acquisition of the increased luminescence, it was used to collect signal-distance curves. Therefore, TERS acquisition was set to acquire one signal per second at 1.3 mW power, and the tip was retracted 20 nm from the surface and approached again with

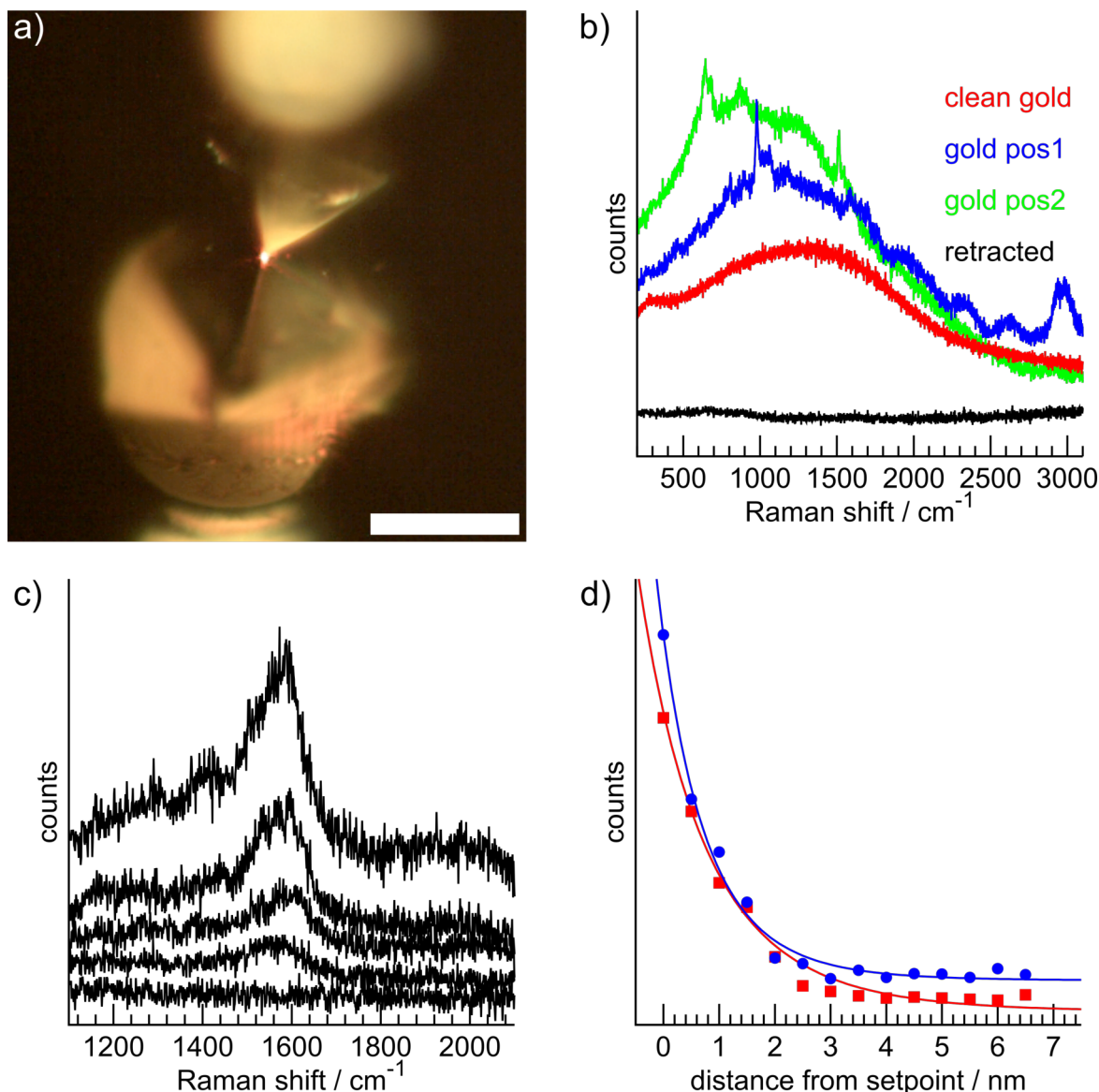


Figure 6.13.: a) Optical image of a TERS probe engaged to a gold sample in STM feedback. The shape of the tip together with the reflection from the sample surface allowed for good coarse alignment of the laser to the hotspot area (scale bar 60 μm). b) TERS and far-field spectra collected in extended scan mode. c) Set of collected approach curves showing the five signals closest to the gold surface: starting from the bottom, each curve was acquired with the tip being 5 Å closer to the gold surface. d) Integrated signals of luminescence enhancement for two approaches (points) and the respective fits (curves) calculated using equation 3.15 (chapter 3 section 3.4).

a speed of  $5 \text{ \AA s}^{-1}$  using the SPM's piezoelectric stage. Figure 6.13c shows typical signals collected during one of these measurements. Again, the maximum signal as well as the distinct shape of the signal changed with the position of the probe on

the clean gold sample. Using the integrated signal over  $1400\text{ cm}^{-1}$  to  $1800\text{ cm}^{-1}$  in the collected spectra allowed to evaluate signal-distance curves. Figure 6.13d shows two of the curves obtained in this way, by fixing a set-point distance of 1 nm and varying the hypothetical tip radius  $R$  as well as the background noise  $I_{noise}$  as fit parameters according to equation 3.15.

$$I(z) = I_{set} \cdot \frac{(R + z_{set})^{10}}{(R + z)^{10}} + I_{noise}$$

Both showed the expected  $z^{-10}$  dependency. Note that the broad-band signal and

Curve colour	$I_{set}$ in counts (fixed)	$z_{set}$ in nm (fixed)	$R$ in nm (floating)	$I_{noise}$ in counts (floating)
red	537.3	1	12.3	23.4
blue	618.8	1	8.3	79.7

Table 6.2.: Fit results of the curves depicted in Figure 6.13d.

not a distinct peak was evaluated, which allowed the function to converge against a constant value for large distances, corresponding to the background noise. Interestingly, tip radii of 12.3 nm and 8.3 nm were found from fitting the two depicted functions. These values appeared to be too low compared to the values measured during the analytical SEM characterisation of the tips, which were in the range of 35 nm. However, it was supposed that the analytical model, which assumes a sharp tip and a flat surface, is insufficient to describe this specific experiment. More precisely, as seen in the STM measurements before, the experimental conditions consist of a sharp tip in proximity to a rough surface. Thus, a stronger near-field generation could be expected, which then is reflected in lower tip radii values in the simple analytical model.

In summary, it was found that a clean gold surface offers a good test sample to investigate the STM and TERS functionality of the fabricated probes. Lateral resolution, STM characteristics and TERS capability were investigated without risking to contaminate the tips. Finally, a gold sample was always kept at hand to verify functionality of the probes during the following experiments.

### 6.4.3. Tip-enhanced Raman spectroscopy on a malachite green covered gold surface

Starting with malachite green coated gold substrates, all the next experiments were performed to acquire further insight into the properties of the fabricated probes as well as to investigate the samples at hand. In contrast to the already performed work, all the following samples featured an intended coverage with molecules expected to yield Raman signals.

First TERS measurements were performed on a  $(8\text{ mm})^2$  gold substrate coated with  $10\ \mu\text{l}$  of  $10^{-7}\text{ mol l}^{-1}$  MGITC solution. Calculating the surface coverage yielded

less than  $10^{-4}$  molecules per  $\mu\text{m}^2$  or a mean inter-molecule distance in the range of some nanometres for a perfect distribution of the molecules. With these numbers in mind, a sufficient Raman sensitivity for few molecule detection was expected to be required to measure any signals. Experimentally, tips were engaged as described before in STM feedback and a  $(1.28\ \mu\text{m})^2$  topography scan was performed. Afterwards, the Raman laser was adjusted for near-field excitation as well as signal collection, and TERS data were acquired.

Figure 6.14a shows the acquired STM image. Again, a sputtered gold surface could be recognised, although only little optimization of the PID feedback control was done. After the start of the TERS acquisition, the tip was moved by manual control over the surface, and spots yielding malachite green TERS signals as well as spots without malachite green signal were found.

Figure 6.14b depicts two baseline-corrected spectra acquired at the points marked with the respective colours in the STM image. The distance between these two points was measured to around 100 nm, which gave a first upper boundary for the lateral size of the TERS hotspot. A further determination of the lateral resolution was planned to be performed by acquiring TERS data along a line scan over a point where Raman bands were detected.

However, it was found that the sample yielded highly unstable signals with respect to time and position. Figure 6.14c shows five baseline-corrected TERS spectra taken at the same point with 1 s in between each acquisition. While the red spectrum resembled perfectly the Raman signature of malachite green, the yellow spectrum already showed different relative band intensities and new bands. Finally, in the black spectrum acquired at last the signal vanished. These changes, namely new bands appearing, a change of the relative band intensities, the whole spectrum appearing or disappearing, or variations of total intensity were observed regularly. Due to the complexity of TERS experiments, different reasons for such an unstable signal generation exist, e.g. the decomposition of molecules due to the high electrical field. Also, several causes were already discussed in literature [95]. However, it is supposed that the main reason in the present case was the mobility of the MGITC molecules. Due to the high electrical field and the anisotropic molecular structure of MGITC, rotations of the molecules could be initiated, which lead to changes in relative band intensity. Furthermore, electrostatic forces could drag molecules in or push molecules out of the hotspot, leading to the appearance and disappearance of signals. Yet, these observations support the assumption that few molecule detection was achieved.

Figure 6.14d depicts standard far-field spectra collected from three kinds of samples coated with  $10^{-3}\ \text{mol l}^{-1}$ ,  $10^{-5}\ \text{mol l}^{-1}$  or  $10^{-7}\ \text{mol l}^{-1}$  MGITC solution. Although the same excitation power as in the TERS measurements with a sixty times longer acquisition time is applied, only the samples modified with a molecular concentration higher than in the TERS measurement, yielded clear signals. For the  $10^{-3}\ \text{mol l}^{-1}$  and  $10^{-5}\ \text{mol l}^{-1}$  coated sample, MGITC bands comparable to the TERS measurements were found, while the  $10^{-7}\ \text{mol l}^{-1}$  sample did not show MGITC Raman bands at all. This supported once more the conclusion that during TERS measurement the gap-mode led to an extremely high signal amplification. Otherwise, the clear signals discussed earlier could not be explained.

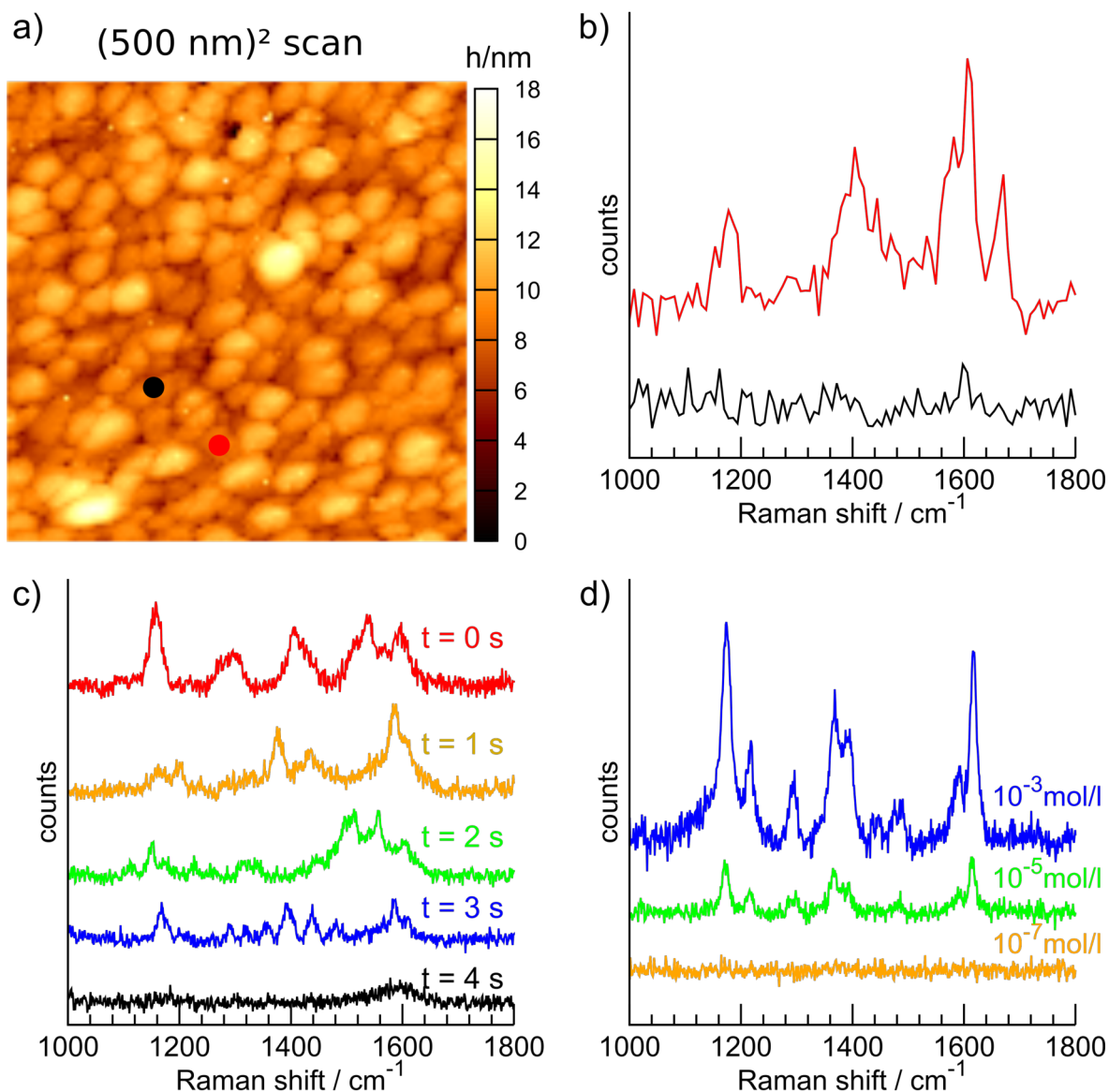


Figure 6.14.: a) STM image of an area with a size of  $(500 \text{ nm})^2$  acquired from a MGITC coated gold sample. b) Two baseline-corrected TERS spectra collected from the spots marked in the STM image with arbitrary offset. c) Baseline corrected MGITC spectra that typically occurred in TERS when collecting signal from a single point for several seconds with arbitrary offset. The red spectrum resembled the expected fingerprint, in the yellow spectrum new bands arose, and in the black spectrum no more signal was found. d) Baseline-corrected far-field spectra taken from the samples covered with different concentrations of MGITC with arbitrary offset. The blue spectrum originates from the sample coated with the  $10^{-3} \text{ mol l}^{-1}$  stock solution, the green spectrum from the coating with the  $10^{-5} \text{ mol l}^{-1}$  solution and the yellow spectrum from the coating with the  $10^{-7} \text{ mol l}^{-1}$  solution.

Note that TER investigations on the two samples coated by higher concentrations of MGITC solutions were performed as well, and both resulted in the measurement of TER signals practically everywhere on the surface. A calculation of the mean inter-molecule distance yielded values of around 1 nm for the  $10^{-5} \text{ mol l}^{-1}$  coated sample and a multilayer coverage for the  $10^{-3} \text{ mol l}^{-1}$  coated sample. While this allowed for a direct measurement of TER signals without scanning the tip, signal stability over time could not be achieved either. This was again attributed to the lack of immobilisation of the malachite green molecules. Worse, unwanted contamination with MGITC molecules of the STM tips was more often observed in these cases, yielding strong malachite green signal collection even when the sample was retracted and thus rendering the probe useless for further application. It was concluded that a higher surface concentration of molecules directly increased the chance for a contamination of the probe. Nonetheless, the higher concentration malachite green samples were used for an evaluation of the fabrication process by testing a set of ten routinely fabricated probes. With each tip, strong TER signals were collected, though they were collected from different areas on the sample<sup>3</sup>, varying in intensity and showing the already discussed signal instability. Due to the latter reasons, a precise determination of the reproducibility of the tip fabrication process with respect to the plasmonic properties was not possible here, although confirmation of the TER activity was achieved.

In summary, the malachite green coated samples presented a direct approach to verify the TERS functionality of the fabricated probes. This way, the TER activity of ten out of ten tips from a routinely fabricated set of probes was confirmed. Especially a sample coated with a highly diluted solution required strong near-field enhancement of the optical excitation to allow for measurable signal collection during the short acquisition time. Furthermore, due to the incomplete coverage, scanning of the tip was necessary to find regions with molecules present, indicating a lateral resolution in the range of some ten nanometres. On the other hand, due to the unstable nature of the Raman spectra and the far-field signal below the detection limit, the determination of a contrast factor was not possible in this case. Hence, samples yielding stable Raman spectra over time and a measurable far-field signal were searched for. Furthermore, a homogeneous coverage of the surface was expected to be favourable, to avoid the influence of local concentration differences when determining the contrast factors. This led from samples with randomly distributed MGITC molecules, which were also resonant to the excitation, to samples covered with thin, nonresonant scattering layers of Raman active materials.

### 6.4.4. Investigation of ultra-thin amorphous carbon layers

The next set of samples consisted of layers of sputtered carbon on gold with thicknesses in the range of 3 nm to 20 nm. Due to the slow sputter process, a complete coverage of the sample surface with carbon was expected. Furthermore, after fabrication STM feedback was tested positively, allowing for stable tip control as well

---

<sup>3</sup>A precise positioning of ten different tips at the same spot is impossible, without imaging several hundreds of square microns of sample surface in STM feedback each time.

as imaging, and a nonresonant, stable, broad-band Raman signal was expected [96–98].

Firstly, standard Raman measurements on the thickest carbon layer revealed a weak signal generation, hence, long acquisition times were required to achieve a reasonable signal-to-noise ratio. Figure 6.15a shows the collected Raman signal, acquired over 3 min using a laser power of 0.70 mW and a 50x objective. The spectrum was described by fitting two Gaussian functions accounting for the G- and D-peak, depicted in black and brown, respectively. The red dotted line corresponds to the sum of these curves. Due to the achieved fit quality, a more precise analysis using a combination of a Breit-Wigner-Fano line and a Lorentzian curve was found to be not necessary. The G-peak center was found to be located at  $1534\text{ cm}^{-1}$  and the D-peak at  $1366\text{ cm}^{-1}$ , which is in accordance with typical literature values of  $1500\text{ cm}^{-1}$  to  $1630\text{ cm}^{-1}$  for the G-mode and around  $1350\text{ cm}^{-1}$  for the D-mode [97]. The broad widths as well as the high intensity of the D-peak relative to the G-peak are characteristic for amorphous carbon [96, 97].

Next, the samples were utilised for further application of the fabricated TERS probes. After ensuring STM compatibility and proper tunnelling feedback, the TERS coupling was adjusted until near-field signal collection was achieved. Afterwards, TER signals were collected using lift-mode scanning with the same excitation power of 0.70 mW as in the far-field measurement. In this mode, the tip was scanned along a single line for 100 nm in tunnelling feedback, retracted for 50 nm from the sample surface at the endpoint and retraced along the acquired curvature. Back at the beginning, the tip was approached to the surface in feedback again and the next cycle started. With the lowest possible scan frequency of 0.1 Hz, it was possible to collect 10 TER spectra per cycle. Thus, five spectra during trace and five spectra during retrace were acquired. For data analysis, only the middle three spectra for the trace or retrace were evaluated by averaging the signal, to avoid influence of the approach and retraction moves.

Figure 6.15b shows TER signals acquired in this way. In detail, signals from traces in feedback (brown, green, yellow) and signals from the respective retraces (black, blue, red) are depicted. During the trace phases, strong near-field enhancement of the signals was observed, which allowed to collect Raman spectra with reasonable signal-to-noise ratio in only 3 s, compared to the 180 s in the far-field measurement using the same excitation power. Furthermore, the signals were found to be stable over time; in fact, no change of the spectrum was observed at all. One reason for this was supposed to be the fact that a solid layer of molecules is present, in opposition to mobile MGITC molecules on the samples before. On the other hand, the carbon layer was assumed to be more resistant against decomposition and was not composed of extended anisotropic molecules with a rotationally dependant Raman signal. Note that no contamination of the tip was observed, otherwise carbon signals would have occurred during the retrace phases. Finally, due to the thickness of the carbon layer in the range of some nanometres, the gap-mode, an origin of strong field enhancement, was supposed to contribute less than in the measurements before.

To evaluate a contrast factor  $cf$ , TER spectra taken from a sample with a 10 nm thick carbon coating were compared to far-field Raman spectra collected using the

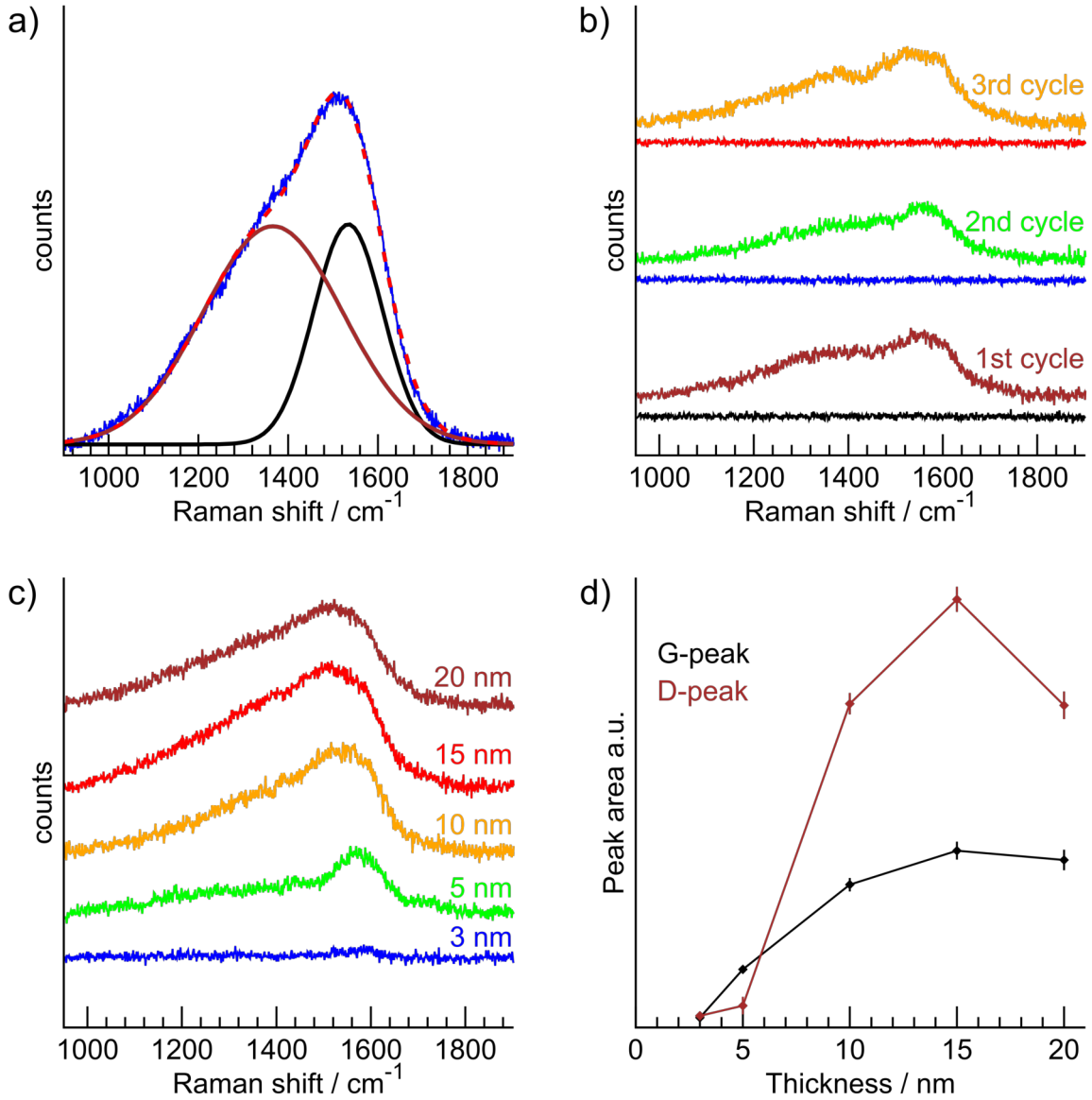


Figure 6.15.: a) Far-field spectrum (blue) with fitted G- and D-peak in black and brown, respectively. The dashed red curve depicts the sum of both fits. b) Baseline-corrected TERS spectra with arbitrary offset taken in lift-mode showing the stability of the signal generation. c) Baseline-corrected TERS spectra with arbitrary offset acquired from samples with different carbon layer thicknesses. d) Peak areas of G- and D-peaks fitted to the spectra shown in c).

100x objective with the same laser power. Next, by comparing the intensities, defined as peak areas, of the measured and fitted G-peaks  $I(G)$  and factoring in the measurement time  $t$ , the contrast factor (e.g. in the case of the tip used in Figure 6.15c) was calculated to

$$cf = \frac{I_{TERS}(G)}{I_{Raman}(G)} \cdot \frac{t_{Raman}}{t_{TERS}} = 14.2 \quad .$$

Contrast factors in the range of 10 to 100 are typically observed for nonresonant molecules in TERS [86].

The carbon samples also offered an opportunity to examine the stability of the fabricated probes with respect to sample changes and contamination. For this purpose, the set of carbon samples was investigated using the same TERS probe for each sample, starting with the thickest carbon coating. An incidence of tip contamination during the measurement should thus be noticed by a constant signal, although less carbon is present on the next sample. Likewise, tip damage should be noticed by a missing near-field signal. Figure 6.15c shows a series of averaged TER spectra collected for different carbon layer thicknesses with a single probe. Each curve is averaged over 10 spectra, collected at the same point with an acquisition time of 1 s. As expected, the thinner carbon layers yielded a weaker broad-band signal, due to the reduced amount of material. Interestingly, these layers also showed only a weak G-peak signal and no or only a relatively weak D-peak signal. This was again reflected in the respective peak areas, which were evaluated by fitting two Gaussian curves and are depicted in Figure 6.15d for the different carbon layer thicknesses. Note that the G-peak curve shows a typical saturation shape, which may be interpreted to give an indication of the vertical extension of the hotspot. Starting at a thickness of around 10 nm to 15 nm, the signal stops rising with respect to the carbon thickness. Since only carbon in the hotspot volume of the tip is considerably contributing to the TER signal, the intensity stops rising as soon as the carbon thickness exceeds the vertical extension of the hotspot.

In summary, carbon-coated gold samples offered a good opportunity to test the TER properties of probes with respect to sensitivity. Due to the fact that the ultra-thin carbon layers showed an extremely weak far-field signal, TER signal generation could be directly verified by lift-mode scanning. Furthermore, the complete coverage of the surface and the fact, that a set of varying carbon thicknesses could be fabricated allowed to directly investigate the stability of single tips with respect to sample changes. Also, a calculation of the contrast factor was possible by comparing the near-field to the far-field signal. Finally, the carbon TER signal was found to be stable over time and contamination of the probes was not observed. It was assumed that this is due to the fact that a stable layer of compact molecules instead of large, mobile molecules is present. However, a disadvantage was the great broadness of the carbon peaks, which made background correction and signal identification difficult. Thus, a sample combining all the above mentioned advantages and yielding several sharp bands would be favourable.

### 6.4.5. Mapping concentration variations of PEDOT:PSS on the nano-scale

The last samples which were investigated by the fabricated pyramidal STM TERS probes were silicon substrates coated with a thin layer of gold followed by a layer of PEDOT:PSS polymer<sup>4</sup>. These substrates were fabricated to combine the different prerequisites required for a test sample for STM TERS while offering all the

---

<sup>4</sup>Samples were fabricated by Dr. Dominik Gollmer at the University of Tübingen.

necessary properties. First and of vital importance, PEDOT:PSS was expected to be compatible to STM feedback due to its electrical conductivity, which most polymeric materials do not feature. Secondly, it is known that PEDOT:PSS offers sharp, characteristic bands in its Raman signature, which allow for a clear confirmation of the plasmonic activity of the tip [99]. Also, due to the layer thickness of around 25 nm the gap-mode could be neglected and only the plasmonic near-field contribution of the free tip was utilised. Thirdly, the polymer was expected to yield a directly measurable far-field contribution, such that a determination of the contrast factor can be achieved simultaneously. Fourthly, since the PEDOT:PSS layer was fabricated by standard thin film processes, the fabrication of lateral structures in the range of some ten nanometres is a viable possibility. In the future, such a sample could become a standardised test substrate for TERS systems and probes, allowing to quantise and compare lateral resolution and contrast factors.

To start with, a conventional Raman investigation of the fabricated sample was performed. Figure 6.16a shows a far-field spectrum acquired with the 100x objective, a laser power of 1.3 mW and an acquisition time of 30 s. The spectrum showed a strong and sharp peak at  $520\text{ cm}^{-1}$ , which originated from the silicon substrate. Furthermore, the characteristic PEDOT:PSS bands were visible, as reported in literature for Raman investigations [99] and TERS measurements [100]. Note that the signal height of the strongest PEDOT:PSS band at  $1433\text{ cm}^{-1}$  was measured to be comparable to the silicon signal at  $520\text{ cm}^{-1}$ .

Next, Raman mapping was performed to acquire insight into the coating homogeneity over a large area. Figure 6.16b depicts two Raman maps on the tens of micrometres scale measured with a pixel size of  $(1\text{ }\mu\text{m})^2$ . In the upper map, the peak height at  $1433\text{ cm}^{-1}$  is depicted by the colour scale, accounting for PEDOT:PSS. A homogeneous signal over most of the sample was found with isolated spots of higher values up to a factor of 5. However, these points were distinguishable from the surrounding area in the optical image and could originate from accumulations of PEDOT:PSS. The correlated increase in the silicon signal (lower map) could be explained with signal contributions from close-by PEDOT:PSS peaks to the silicon peak. Another explanation could be defects of the gold layer, leading to SERS enhancement of the PEDOT:PSS signal and optical access to the underlying silicon. Areas containing such points were avoided during later TERS imaging. The lower map shows the peak height at  $520\text{ cm}^{-1}$  depicted by the colour scale, accounting for the silicon substrate. Again, a very homogeneous signal was found which allowed to assume that the gold layer has only a weak or no effect on the results. Various defects or inhomogeneities of the metal layer could lead to a SERS enhancement, which would complicate an evaluation of the TERS results, as discussed before. In summary, near-constant signals for PEDOT:PSS and silicon were collected over a large area with isolated spots of higher signal intensities, assigned to polymer accumulations or SERS hotspots. The absolute signal intensities of silicon and PEDOT:PSS were again found to be comparable in far-field measurements.

Next, TERS measurements were performed using the fabricated pyramidal tips, a tunnelling bias of 0.8 V and a current set point of 1 nA. After a  $(1.28\text{ }\mu\text{m})$  sized STM image was acquired, the TERS configuration was set up, and TERS imaging in an area of  $600\text{ nm} \cdot 230\text{ nm}$  was started. Figure 6.16c shows two TERS maps on

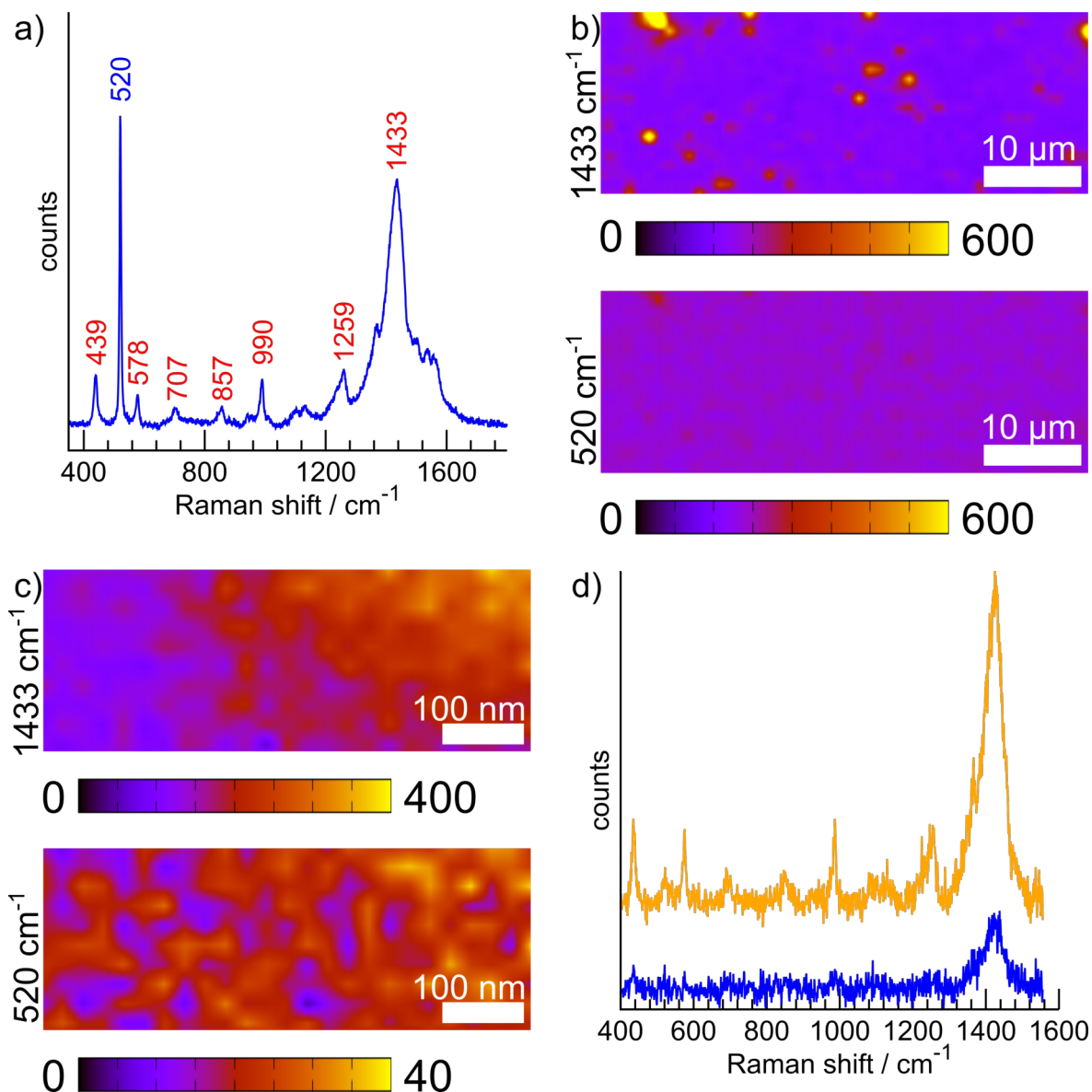


Figure 6.16.: a) A far-field spectrum collected with the 100x objective in standard Raman configuration. b) Far-field maps of  $50\ \mu\text{m} \cdot 20\ \mu\text{m}$  size for PEDOT:PSS and silicon bands. c) Near-field maps of  $600\ \text{nm} \cdot 230\ \text{nm}$  size for PEDOT:PSS and silicon bands. d) Two spectra from the near-field maps. The yellow spectrum originated from the right side, the blue spectrum from the left side of the maps.

the hundreds of nanometre scale with a pixel size of  $(20\ \text{nm})^2$ . As before, the upper map refers to the PEDOT:PSS signal and the lower map to the silicon signal, while the data was plotted the same way as for the maps in b) by evaluating the respective peak heights. Firstly, note that in contrast to the standard Raman data a difference of an order of magnitude between the maximum values of the two data sets was found, with the PEDOT:PSS yielding the stronger signal. This confirmed the assumption that near-field signal from around the tip volume was collected, resulting in a strong

signal from the PEDOT:PSS layer and only a weak far-field contribution from the silicon beneath. Furthermore, this contrast factor of around 10 was high enough to allow for a lateral resolution in the range of some ten nanometres, as clear features were visible in the map. In detail, a low signal was collected on the left side with a gradual increase around the middle of the map to a strong signal on the right side. The exact far-field contribution was unknown, but expected to be much weaker than the measured PEDOT:PSS near-field signal since practically no silicon peak from far-field scattering was found, and thus, it was assumed that a variation of the amount of PEDOT:PSS was the origin for the observed features. Another evidence for TERS was the silicon signal which was found to be extremely weak in the mapped area as expected, if the origin was only far-field scattering. Although a weak correlation with the PEDOT:PSS signal is visible, this could again originate from an overlap of the close-by PEDOT:PSS peaks and the silicon peak or a change in the gap distance to the underlying gold layer due to PEDOT:PSS thickness variations.

Finally, in Figure 6.16d two spectra from the map in c) are depicted. The yellow TERS spectrum originated from the upper right part of the map (high signal) and depicts the measured Raman bands which could be precisely assigned to PEDOT:PSS. Furthermore, in contrast to the far-field spectrum in a), the silicon peak was very close to the background level. The blue TERS spectrum originated from the left side of the map (low signal), yet, the main PEDOT:PSS peak was still visible, as well as some lower peaks. However, it is unclear how much the far-field exactly contributed to this signal.

It is worth mentioning that the PEDOT:PSS layer was found to yield a stable signal over time during TERS measurements on a single spot. This was assumed to be, above all, a consequence of the immobilisation of the molecules in a solid layer. Furthermore, no contamination of the utilised tips was observed. Beside the immobilisation of the PEDOT:PSS molecules, this could also be attributed to the well working STM feedback on this conductive polymer.

In summary, the fabricated PEDOT:PSS samples were found to yield spectra containing PEDOT:PSS bands as well as a peak from the underlying silicon in far-field Raman measurements. A large-scale mapping revealed a homogeneous polymer coating with points of accumulated PEDOT:PSS, which were also visible in the optical image and could thus be avoided in TERS measurements. The STM feedback was found to work properly with standard imaging parameters. In TERS measurements, the near-field signal was found to be stable over time and to yield the characteristic sharp bands, as expected. Contamination of the probes was not observed. These two points were again attributed to the immobilisation of the molecules and stability against decomposition. By comparing the near-field signal of PEDOT:PSS to the far-field signal of the underlying silicon, a contrast factor around 10 could be directly estimated. Thus, TERS mapping in the range of some hundred nanometres was possible, revealing a resolution in the range of some ten nanometres. Finally, it was demonstrated (not shown here) that it is possible to fabricate PEDOT:PSS samples with defined features in the range of some ten nanometres by electron beam lithography. All these properties together make PEDOT:PSS a perfectly suited candidate as a standardised TERS test sample.

## 6.5. Template stripping of AFM TERS cantilevers

This section comprises the results for the fabrication of AFM TERS cantilevers by combining template stripping with micro-mechanical structures. The cantilevers were structured out of SU-8 negative photoresist, which is a well-established material in MEMS processes and offers appropriate properties (e.g. mechanical stiffness and high chemical resistance) for such applications [101, 102]. This was a pragmatic approach, whereas an integration of a template stripping step in a conventional silicon cantilever process chain would have required specialised equipment and knowledge as well as profound experience. As before, some related articles are discussed followed by the results achieved in this work.

Already in 1999, before tip-enhanced Raman spectroscopy was proposed, and for a different application Genolet et al. reported a template stripping process for the fabrication of polymeric cantilevers with pyramidal tips [81]. Pyramidal cavities were fabricated on a silicon substrate by anisotropic wet etching and sharpened by oxidation. Afterwards, cantilever beams as well as chips were fabricated out of a thin layer and a thick layer of SU-8, respectively. A dry release process was established, yielding soft cantilevers with a spring constant of around  $2.5 \text{ N m}^{-1}$ , a resonance frequency of around 87 kHz and typical tip radii of around 30 nm. The fabricated cantilevers were applied to image DNA strands by AFM feedback. It was noted that the mould was found to be reusable after cleaning.

Highly related to the discussed study and the present work is an investigation of Keller et al. on the stress and strain generation during SU-8 cantilever fabrication [103]. In their work, SU-8 cantilever beams were fabricated using different process parameters, especially varying post-exposure bake temperatures, and the initial bending after release was investigated. It was noted that with an optimised post-exposure bake using temperatures of or below  $70^\circ\text{C}$ , diffusion of the photoactive component was prevented and thus, lithography resolution and device release was improved. A prolonged hard bake at higher temperatures around  $90^\circ\text{C}$  was reported to yield low cantilever bending after release and improved storage stability.

In 2014, Geerlings et al. published a process development for the fabrication of in-plane cantilevers, using the template stripping technique and silicon nitride as tip material [104]. In this work, a silicon substrate was anisotropically wet etched using silicon nitride as mask material and circular-shaped mask openings as structures. Due to this, diamond-shaped cavities with tips in several directions formed, which were sharpened by oxidation and moulded by silicon nitride deposition. After etching parts of the silicon away, sharp in-plane tips with radii in the range of ten nanometres were achieved. In this case, the cantilever chip and beam were structured out of the silicon substrate. The fabricated cantilevers were successfully mounted in a commercial AFM and utilised for imaging different sample surfaces. A comparison to commercially available cantilevers yielded a similar performance.

### 6.5.1. Fabrication of metal, beam and chip

For the purpose of cantilever fabrication, only moulds with a silicon oxide mask were utilised, due to the formation of a smaller undercut during wet etch compared to a silicon nitride mask. The reason for this is the higher etch rate of silicon oxide compared to silicon nitride. Furthermore, instead of a single gold metal layer as before, a composite layer of gold followed by chromium was sputter deposited. The gold layer with a thickness of 100 nm was expected to be sufficient for plasmon excitation, while the following 10 nm chromium layer was deposited to facilitate adhesion to the SU-8 structures.

All SU-8 bake processes were performed using slow temperature ramps of below  $10 \text{ K min}^{-1}$  and a low post-exposure temperature to minimise stress, which is of particular importance for thick layers above  $50 \mu\text{m}$  [103, 105, 106].

The thickness  $t$  of the first SU-8 layer, which later formed the cantilever beam, was chosen to be  $10 \mu\text{m}$  to achieve a reasonable spring constant. An estimation for the latter could be calculated in advance using a mechanical model [107], the geometrical beam dimensions and the Young's modulus  $E \approx 2.5 \text{ GPa}$  to  $4.0 \text{ GPa}$  of SU-8 [101, 105, 106]. The lithography mask featured a beam width  $w$  of  $100 \mu\text{m}$  and a beam length of  $500 \mu\text{m}$ . However, the final length was defined by the positioning of the cantilever chip lithography mask and could be reduced freely. To achieve a stable structure and allow for a proper release, typically lengths  $l$  in the range of  $300 \mu\text{m}$  to  $500 \mu\text{m}$  were chosen. Together, the spring constant  $k$  was then calculated in advance to be in the range of

$$k = \frac{E \cdot w \cdot t^3}{4 \cdot l^3} = 0.5 \text{ N m}^{-1} \text{ to } 3.7 \text{ N m}^{-1} .$$

This value is comparable to commercial silicon AFM probes designed for contact mode.<sup>5</sup> However, due to the cubic dependency on the SU-8 thickness, it could be further tuned over a wide range.

On the other hand, a calculation of the first resonance frequency  $f_0$ , using a SU-8 density of  $\rho = 1190 \text{ kg m}^{-3}$  [108], yields a value in the range of

$$f_0 = \frac{1.029 \cdot t}{2\pi l^2} \cdot \sqrt{\frac{E}{\rho}} = 9 \text{ kHz to } 33 \text{ kHz} .$$

Cantilevers with these properties could be applied for contact mode AFM feedback, and the low spring constant might be beneficial for reduced tip wear and damage. On the other hand, tapping mode measurements are usually performed using stiffer cantilevers with a higher resonance frequency in the range of 300 kHz. SU-8 cantilevers were found not to be suited for this mode.

Figure 6.17a shows a tilted SEM image of the fabricated SU-8 thin layer. An open question was the filling of the cavity by SU-8 resist during spin coating. As visible in the images, a flat surface around the beam area over the buried tip was observed, which indicated a complete fill. However, to achieve further confirmation on this point, FIB SEM analysis was once more applied. Notably, large-area milling had

<sup>5</sup>For example, Bruker's RESP cantilevers offer a spring constant of  $0.1 \text{ N m}^{-1}$  to  $5 \text{ N m}^{-1}$ .

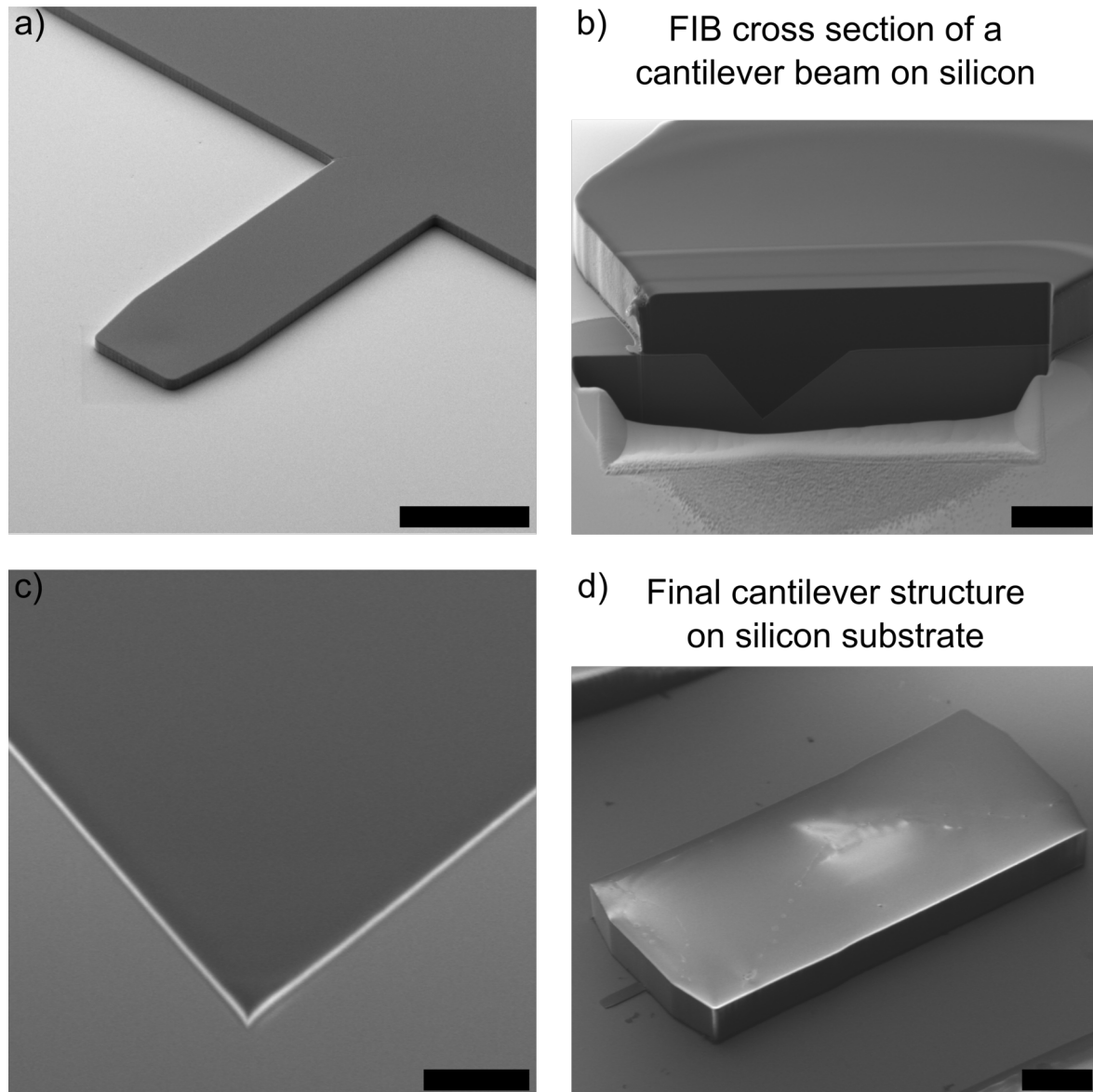


Figure 6.17.: a) Tilted SEM image of the structured thin SU-8 layer showing the cantilever beam material over the buried, pyramidal cavity (scale bar 100  $\mu\text{m}$ ). b) Overview of a FIB milled cross section to investigate the cavity filling (scale bar 20  $\mu\text{m}$ ). c) Higher magnification SEM image of the tip region, showing a complete fill and a defect-free interface between the SU-8 and the metal layer (scale bar 2  $\mu\text{m}$ ). d) Tilted SEM image of the final cantilever (scale bar 500  $\mu\text{m}$ ).

to be performed to analyse a cross-section of the buried, micron-scaled tip volume. Figure 6.17b shows an overview image of the prepared section. There, no entrapped air or other defects were visible. Figure 6.17c shows a magnification of the very tip structure. Again, a complete SU-8 volume without voids, cracks or discontinuities was observed. Furthermore, a defect free interface to the metal layer was found, which is of particular importance for release and functionality of the probes.

Finally, the thick layer of SU-8 was fabricated in a two-step process to form the chip. Here, temperature ramps and proper spin coating were the critical parameters to achieve a defect-free layer which yields high quality structures in the end. Figure 6.17d shows a tilted SEM image of the final SU-8 structure after lithography of the SU-8 thick layer. A well-defined chip body was observed, attached to the short cantilever beam.

### 6.5.2. Cantilever release

The cantilever release was performed manually using tweezers. The chip height was aimed to be around  $500\ \mu\text{m}$ , which was sufficient for manipulation by hand. However, a low yield of around 10% had to be taken into account, which was attributed to the manual release procedure and thus, imprecise motions. A specialised tool for proper gripping and a defined release motion, well-aligned perpendicular to the substrate surface, would be necessary to achieve an effective process for individualisation of the structures. Typical defects experienced during release were a breaking of the cantilever beam or the damaging of the tip, both of which could be avoided with a specialised tool in the future.

A process step for metal removal was found to be optional. Due to the low thickness of the metal layer, it could be removed quickly in a dry etch step using ion milling. However, due to the same reason the metal was found to break well along the structure edges during release.

Figure 6.18a and b shows tilted SEM images of released cantilevers. Note that an examination by optical microscopy was found to be sufficient for confirmation of a successful release step. Undamaged released cantilevers were stored under clean conditions until they were applied for AFM TERS measurements.

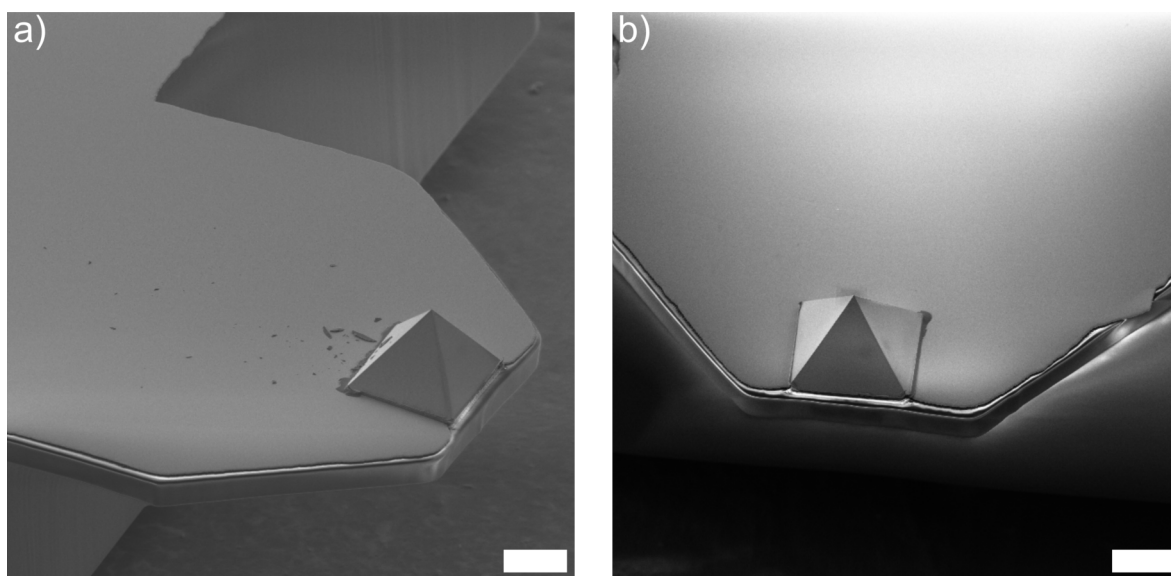


Figure 6.18.: a) and b) Tilted SEM images of cantilever beams after release with the pyramidal gold tip located at the end (scale bars  $20\ \mu\text{m}$ ).

### 6.5.3. AFM TERS measurements

The thus-fabricated cantilevers were tested for AFM and TERS functionality on a carbon sample, similar to the samples investigated in section 6.4.4. However, this time a silicon substrate was coated with a 200 nm thick photo resist, structured by electron beam lithography and developed<sup>6</sup>. Afterwards, a 30 nm thick gold layer was sputter deposited, followed by a 20 nm thick amorphous carbon layer, and a lift-off in acetone was performed. Therefore, structured carbon samples were fabricated with different features. As before, the Raman far-field signal was found to be below the detection limit with acquisition times of only several seconds.

The fabricated AFM cantilevers were mounted in the SPM just as commercially available ones. This was possible due to the matching dimensions, defined by the optical lithography. After adjustment of the optical laser for feedback signal, a total voltage of over 2 V on the quadrant photodiode was measured. This value is comparable to silicon cantilevers coated with a metallic reflection layer and is attributed to the full metal coverage on the bottom side as well as the transparency of the SU-8, resulting in good reflective properties.

Before AFM measurements were performed, optical access to the cantilever tip was investigated. For this purpose, the cantilever was imaged through the TERS objective and manually engaged to the sample surface until a reflection on the surface appeared. It was found that due to the geometrical conditions in the utilised set-up (see chapter 5 section 5.3), a reduction of the angle between the TERS objective and the sample surface from 30° to around 15° was necessary for optical access to the tip.

Figure 6.19a shows an optical image of the cantilever acquired through the TERS objective. In contrast to the fabricated STM TERS probes, here, the geometrical excitation conditions were well reproducible for each probe. The polar angle as well as the azimuthal angle of the pyramidal tip with respect to the Raman laser beam were defined by the cantilever geometry and the angle of the TERS objective.

Next, the cantilevers were engaged in a slow manner, using a piezoelectric sample stage with a sweep amplitude of 800 nm and a motor step of 400 nm until a deflection of 1 V was detected on the quadrant photodiode. AFM imaging was performed using this set point for feedback, and a PID setting of 1.0/0.1/0 was found to optimise the signal. It was found that scan speeds of up to 20  $\mu\text{m s}^{-1}$  could be used.

Figure 6.19b shows a  $(20 \mu\text{m})^2$  scan acquired on a carbon marker structure, resembling the number 4. The measured height of around 40 nm was in good accordance with the fabrication process. Furthermore, damages on the structure could be identified, which were already observed optically. These were attributed to a defective resist mask, leading to a removal of structure parts during lift-off.

In a next step, the tip was moved on top of the carbon structure and the optical TERS path was aligned. After carbon near-field signal was successfully detected with an acquisition time of 1 second and a laser power of 0.7 mW, a 2.5  $\mu\text{m}$  long line scan along the blue arrow in Figure 6.19b was started. Figure 6.19c shows exemplary TER spectra, which were collected at different distances from the starting point.

---

<sup>6</sup>This work was performed by Omar Tanirah at the Institute for Applied Physics, University of Tübingen, Germany.

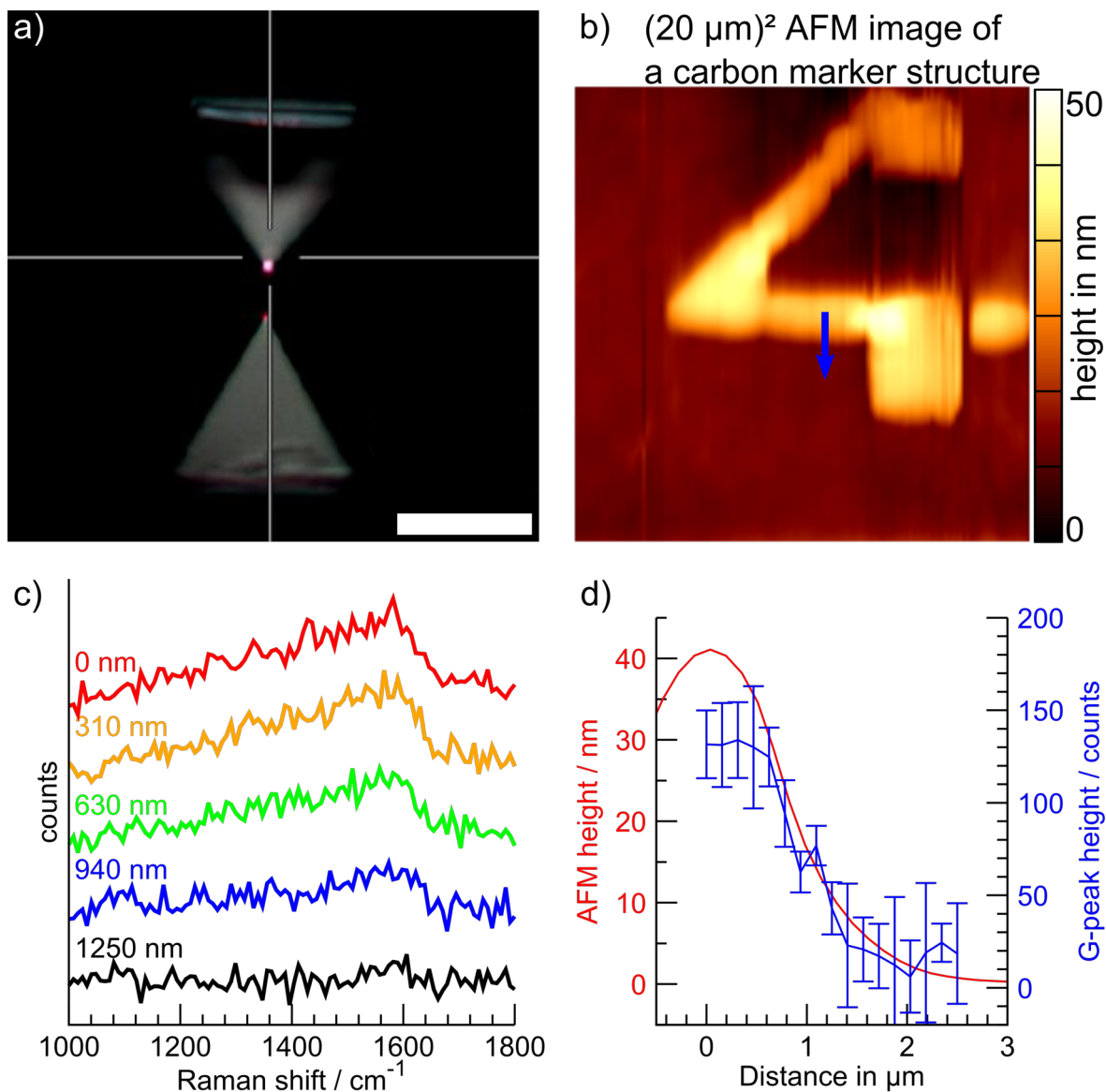


Figure 6.19.: a) Optical image of the cantilever beam and the pyramidal metal tip acquired through the TERS objective. The reflection on the sample surface is visible (scale bar 20  $\mu\text{m}$ ). b) AFM image of a structured carbon sample, showing a marker in the shape of the number 4. The blue arrow shows the path of the performed 2.5  $\mu\text{m}$  TERS line scan. c) Exemplary baseline-corrected TER spectra with arbitrary offset collected during the line scan at different distances from the starting spot. d) A comparison of the AFM height signal and the evaluated maximum G-peak intensity of the carbon band in the TER signals.

Here, the already observed amorphous carbon signal was visible, disappearing after around 1  $\mu\text{m}$  along the scan as the edge of the carbon structure is reached.

Figure 6.19d shows a comparison of the collected AFM height signal and the evaluated height of the G-peak in the TER signal at different points along the line scan.

Clearly, a correlation between the signal and the structure was observed. Note that the large error bars resulted from the high noise in the signals, which could have been presumably lowered by integrating for several more seconds. Furthermore, the height signal is a convolution of the actual sample geometry and the tip shape, which has to be considered especially when using tips with large apex angles. However, due to the low height of the carbon structure, the influence of the tip apex on the lateral resolution could be estimated to be in the range of some ten nanometres. Thus, the continuous decline of the structure's height over more than 1  $\mu\text{m}$  is supposed to originate from the fabrication process and has to be improved in the future.

Finally, although TER enhancement by the cantilever tips was observed (due to the low carbon thickness, no signal appeared in pure far-field measurements), further investigations are necessary to determine values for the contrast factor and the lateral resolution. The latter could be performed on a structured sample with sharp features in the nanometre range, as planned for the future.

In summary, polymeric cantilevers with pyramidal gold tips were fabricated by standard clean room processes. The structures were designed to be compatible to commercial AFM systems and provide spring constants comparable to commercially available probes for contact mode. However, due to the material choice low resonance frequencies of the cantilever beams were expected and thus, the fabricated cantilevers were not applicable for non-contact AFM. An idea for the future is to fabricate the cantilever beam out of a 2  $\mu\text{m}$  thick silicon nitride layer, deposited by PECVD, and adjust the dimensions for an appropriate resonance frequency around 300 kHz. Combined with a thick SU-8 chip, this could be a promising way to achieve cantilevers especially suited for tapping mode applications.

The batch-fabricated cantilevers were partly successfully released from the substrate using tweezers and could be handled similar to standard cantilevers. Yet, a specialised tool for release was found to be necessary to increase the yield and provide an efficient individualisation process.

Finally, the fabricated probes were mounted in the SPM and utilised for TERS measurements in combination with contact-mode AFM feedback. Here, typical signals from thin amorphous carbon layers were collected and correlated to the structure geometry. However, a more detailed investigation of the probes with a standardised TERS test sample is necessary to characterise the cantilevers for their TERS properties.

## 6.6. Template stripping of SERS substrates

The last section comprises the description of all SERS related results achieved. There are different routes to approach the fabrication of SERS substrates. One can either match the structures' plasmonic resonance to the excitation wavelength, to the resonance wavelength of the material of interest, achieve both, work with broad-band structures, or several structures of different resonance wavelengths. Each of these possibilities can be achieved with different fabrication techniques, providing distinct advantages and disadvantages.

Already, template stripping is known to allow for the fabrication of surfaces covered by plasmonically active pyramidal structures on a large scale in a reproducible way [77, 109]. However, this technique requires the fabrication of a mould, which causes limitations for the structure geometries (e.g. no concave side walls) as well as a need for large-scale lithography techniques. The latter can be problematic when the structure size approaches the nano-scale and optical lithography is insufficient (e.g. the requirement for nano-imprint lithography).

Another way of SERS substrate fabrication is the immobilisation of metallic structures, functionalised with the material of interest, on a substrate using a colloidal solution [110]. For example, metal particles with a defined diameter can be suspended on a glass surface. In this case, the plasmon resonance can be matched to the wavelength of the excitation or the material of interest. However, the resulting random distribution of the particles on the surface limits the reproducibility and allows for accumulations of particles or areas without any particles at all.

Other common techniques to fabricate engineered substrates are soft lithography [111, 112] and electron-beam lithography [113]. Both offer the possibility to structure large areas with defined features in the nanometre range and can be further combined with specialised metal deposition or dry etch processes, e.g. inclined sputtering or inclined etching. However, these techniques lack the batch fabrication compatibility and are often costly as well as complex.

### 6.6.1. Fabrication of SERS substrates

Moulds for SERS substrates were fabricated using the established processes. In this case, the silicon wafers featured arrays of pyramidal cavities with different base dimensions and spacings, from 10  $\mu\text{m}$  to 100  $\mu\text{m}$ . As in the case of the STM TERS probe moulds, a 1  $\mu\text{m}$  thick gold layer was deposited. Here, this was done to later prevent Raman scattering from the adhesive below the gold, which was utilised for release. Metal lift-off was found to be optional, resulting in SERS substrates featuring either solely gold pyramids or a complete gold layer with pyramidal structures.

For release, a short plasma activation of the final mould surface was found useful to facilitate bonding. SERS substrates were fabricated by using UV-curable adhesive and standard sample glass slides found in optical microscopy. The ability to successfully release large arrays around  $(2\text{ mm})^2$  after curing was attributed to the small wedge angle during separation, resulting from the glass slide's dimensions.

Figure 6.20 shows HIM and SEM images with various magnifications of released SERS substrates. It was observed that a damage-free release over wide areas was

achieved. The only defects observed at times were isolated missing pyramids, which was attributed to insufficient wetting of the cavity by the photo-curable adhesive. Especially with high magnification imaging, tip radii in the range of some ten nanometres could be observed, similar to the released structures during STM and AFM probe fabrication.

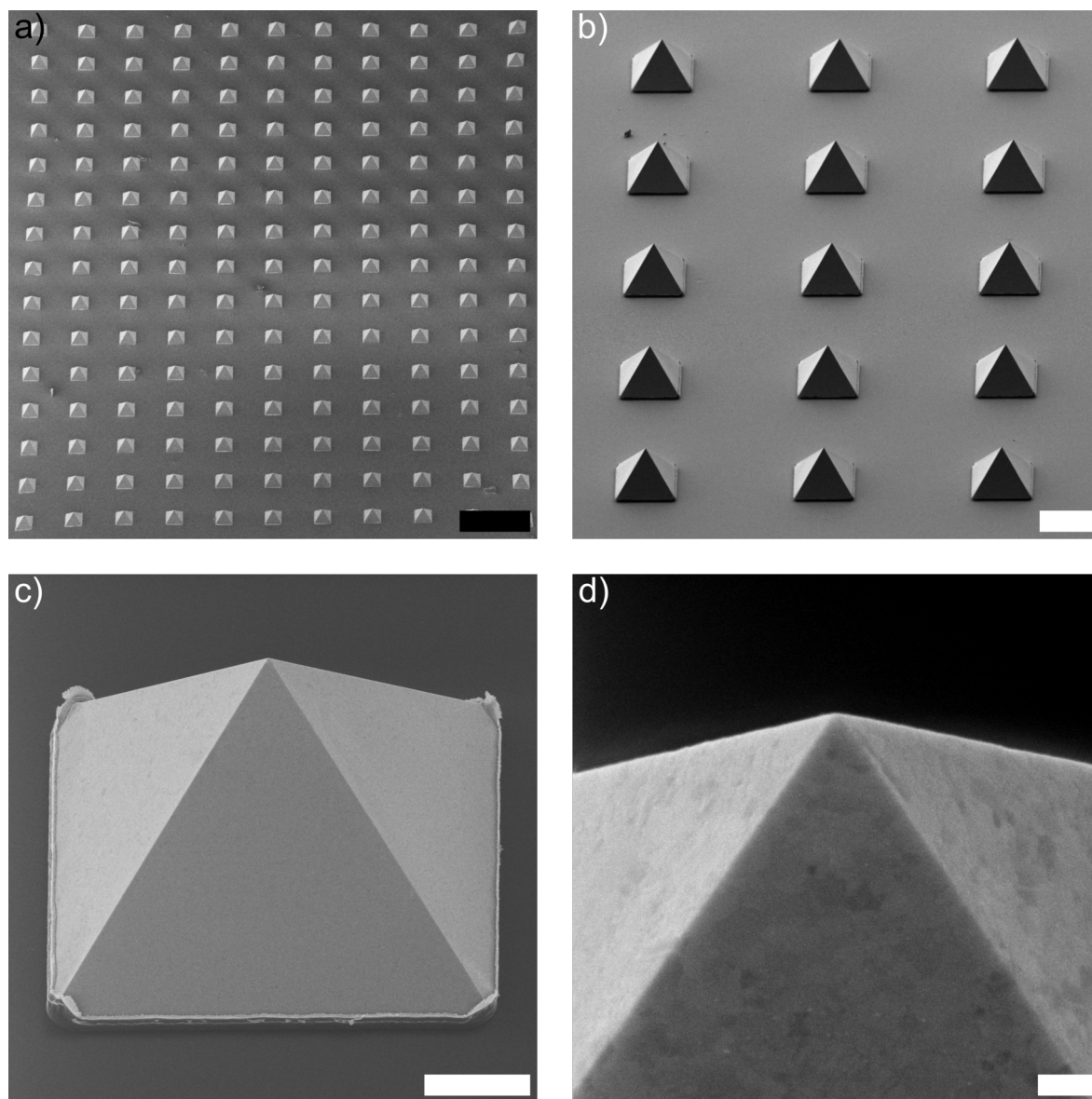


Figure 6.20.: a) Tilted HIM image of a released pyramid array in the millimetre range (scale bar 100  $\mu\text{m}$ ). b) Tilted SEM image of several released gold pyramids (scale bar 20  $\mu\text{m}$ ). c) Tilted HIM image of a single pyramid (scale bar 5  $\mu\text{m}$ ). d) High magnification HIM image of the very tip showing a tip radius in the range of some ten nanometres (scale bar 200 nm).

### 6.6.2. SERS measurements

SERS measurements were performed on a substrate fabricated by template stripping of pyramidal gold structures with a continuous gold film in-between using the described processes. Afterwards, the surface was coated with 10  $\mu\text{l}$  of a  $10^{-3} \text{ mol l}^{-1}$  solution of MGITC and after drying of the solvent (ethanol), SERS measurements were performed. The excitation power was kept below a maximum value of 0.13 mW, to prevent decomposition of the dye molecules, using the red laser with a wavelength of 633 nm for excitation. The acquisition time was set to 10 s per point.

Figure 6.21a shows an optical image taken using the standard light path in the Raman spectrometer. Due to the utilised low magnification, the depth of focus could be neglected for Raman measurements, considering the pyramid height of around 12  $\mu\text{m}$ . The coloured circles mark three points at which Raman spectra were collected. The acquired signals are depicted in Figure 6.21b with the respective colour. It was observed that on around 95% of the pyramid tips strong MGITC signals could be collected. These signals were attributed to SERS enhancement by the metal structure. This assumption was based on the fact that far-field signals collected on the flat gold surface in between the pyramids did not yield any discernible MGITC bands, as expected for the utilised measurement parameters, the utilised objective and the MGITC concentration. However, due to the concentration of the MGITC solution a complete coverage of the sample surface was expected.

To further investigate the SERS enhancement, mapping of a single metal pyramid was performed. Figure 6.21c shows a Raman map taken on a structure, depicting the colour coded maximum intensity of the Raman band at  $1620 \text{ cm}^{-1}$ . The white lines outline the pyramid edges. From the collected signal, it was assumed that a SERS hotspot was present at the pyramid tip as well as SERS hotspots were present along the left metal base edge. However, the high signal at the left base edge could also result from an accumulation of MGITC molecules during drying. Figure 6.21d depicts three spectra out of the map, showing signals from the tip area as well as from the left and right sides of the map. MGITC Raman bands are visible in the spectra from the tip and the left edge. Again, a variation of the signal at a single spot over time was observed, comparable to the TERS measurement on MGITC before. This was again attributed to the large, anisotropic molecule and the lack of immobilisation during functionalisation.

In summary, SERS substrates based on template stripped metal pyramids with areas of around  $(5 \text{ mm})^2$  were fabricated. The final substrates were investigated by SEM and HIM and showed a defect-free release of metal structures over large areas. Afterwards, the surface was functionalised by MGITC dye molecules. SERS measurements were performed, and hotspots on pyramid tips and base edges were observed.

However, note that the design of the substrates allows for several improvements. Firstly, the density of the pyramids could be increased by using a base size of down to  $(1 \text{ }\mu\text{m})^2$  and a minimal grid spacing in between. This would yield an increased amount of structures while still allowing to collect only signal from a single hotspot at once. Furthermore, due to the decreased base dimension a structure height below

1  $\mu\text{m}$  would be achieved, allowing for higher magnification while still being able to neglect the depth of focus.

Another route could be the utilisation of nano-imprint lithography for the mask, allowing to fabricate structures with base edges of some hundred nanometres. Thus, several hotspots could be measured at once, allowing for an improved application for the ensemble detection of e.g. small concentrations of molecules in solutions.

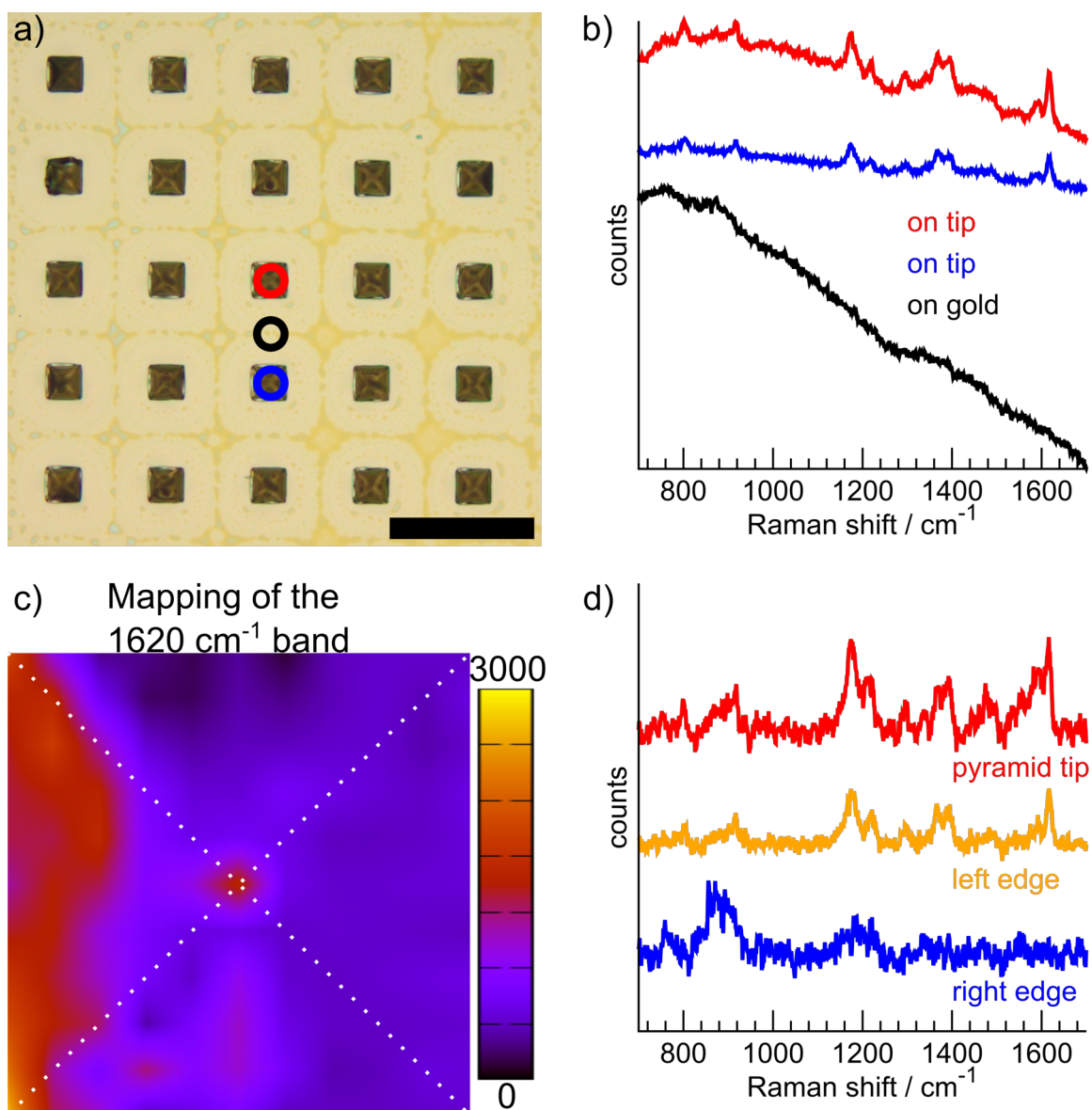


Figure 6.21.: a) Optical image of the functionalised SERS substrate with points of spectra acquisition (scale bar  $100\ \mu\text{m}$ ). b) SERS spectra with arbitrary offsets acquired at the points marked in the optical image. c) SERS map of a single pyramid with a size of  $(40\ \mu\text{m})^2$ . The white lines mark the pyramid edges. SERS enhancement at the tip and increased intensity at the left edge was observed. d) Exemplary baseline-corrected SERS spectra with arbitrary offset from the map acquired over a single pyramid. Besides the signature Raman bands of MGITC at  $1100\ \text{cm}^{-1}$  to  $1600\ \text{cm}^{-1}$ , a broad-band at around  $900\ \text{cm}^{-1}$  of unknown origin is visible.



## 7. Summary and Outlook

In the present work, a stable simulation model to investigate the electrical near-field excitation at the tip of pyramidal gold structures by a Gaussian laser beam was created. The field enhancement was evaluated in dependency of the angles of incidence of the excitation beam (azimuthal and polar), and in dependency of the tip apex radius and angle. It was found that the angles of incidence have a limited influence on the near-field enhancement, yielding factors of 3.7 to 5 in the experimentally relevant range. The apex angle of the pyramidal structure was found to be optimally suited in the range of around  $30^\circ$  to  $70^\circ$ , yielding an enhancement of a factor of 4 to 5. The apex radius was found to be the most important parameter, yielding an enhancement factor of up to 10 for a radius of 5 nm and only 3 for a radius of 40 nm. The simulations were repeated with an additional metal surface located 5 nm below the tip. In this case, a similar dependency of the field enhancement on the variation parameters as for the free tip was found. However, the total field enhancement was found to be a factor of 4 to 6 higher, and the near-field distribution was found to be more localised. This was attributed to the presence of a gap-mode, allowing to excite oscillations of free charges in the metal surface. In the future, variations of several parameters at once could be performed to acquire knowledge about the correlation between these. Furthermore, time-dependent calculations could yield insight into the particular plasmon resonance modes of the structure.

In the beginning of the experimental part, a batch process for the fabrication of high quality moulds on silicon substrates was established. The characteristics of the moulds were investigated and evaluated by combined FIB-SEM analytics, and smooth surfaces as well as sharp apex angles down to  $33^\circ$  after oxidation were found. Metallisation of the moulds with gold by sputter deposition was investigated. It was found that sputtering yields a defect-free coverage of the cavity sides, and a polycrystalline layer with grain diameters in the micrometre range. However, the formation of cavities at the very tip was observed. This is supposed to limit the accomplishment of smaller apex radii and could be presumably avoided in the future by thicker oxidation. Furthermore, additional metal materials, for example silver, could be tested for process compatibility.

Next, a release process for individual metal structures by ball bonding was established. This allowed to fabricate electrically conductive probes with cycle times of some seconds, which were attachable to a SPM adapter. A further development could improve the attachment of the probes after bonding to the adapter pieces, lowering the process time and allowing for higher throughput. A possible way to achieve this could be a crimp connection to the metal adapter.

The fabricated structures were tested for their applicability as STM TERS probes. Firstly, their STM functionality was verified in a comparison to standard tungsten STM probes by scanning a gold surface, and imaging a roughness in the nanometre range. High congruency of the images was found, and an additional comparison to SEM imaging verified a working STM feedback. Next, the measurement of the tunnelling current as a function of the tip-sample distance allowed to evaluate the work function, which was found to be in agreement with literature values. In the future, a reference sample with a sharp feature could be utilised to precisely evaluate the apex shape by deconvolution of the measured topography signal.

The applicability of the fabricated structures as TERS probes was, firstly, investigated by collecting near-field luminescence signals from clean gold surfaces. In this case, the typical  $z^{-10}$  dependency of a near-field signal on the tip-sample distance was found. Furthermore, it was noted that the pyramidal shape is beneficial for the coarse laser alignment.

Secondly, surfaces covered with low concentrations of MGITC molecules were investigated. In this case, near-field signals presumably originating from the detection of few molecules were acquired. However, the signals were found to be unstable with respect to Raman bands and intensity, which was attributed to the missing immobilisation of the molecules. Even so, MGITC substrates were used to test a set of ten routinely fabricated probes for tip-enhancement, and near-field signals were collected from each.

Thirdly, ultra-thin amorphous carbon layers were imaged. Here, a broad-band TER signal was found, and due to the high stability of the signal, contrast factors in the range of 5 to 20 were reliably found.

Finally, a thin PEDOT:PSS layer was investigated by TERS. A comparison of the acquired near-field spectrum to the typical far-field spectrum revealed that apparently a dominant signal contribution from the volume around the tip was measured. Furthermore, TERS imaging in the range of some hundred nanometres was performed, resolving presumably variations in PEDOT:PSS thickness on this length scale. Note that this material was found to yield a stable TERS signal with distinct bands, and that it appears to be compatible to nano- and micro-structuring processes. Thus, PEDOT:PSS is a potential material for a future TERS reference sample, allowing to objectively test for sensitivity and lateral resolution of TERS probes and set-ups.

Furthermore, a batch process for the fabrication of polymeric cantilevers with template-stripped pyramidal tips was developed. Although only a low-yield release was manually achieved, in the future, a specially designed instrument could increase the yield, and thus allow for a complete efficient fabrication chain.

First TERS measurements in AFM feedback were performed, verifying the near-field activity of the tips. TER signals from thin amorphous carbon structures were collected and correlated to the topography signal. Given that AFM feedback can be applied to many surfaces, a great variety of different samples could be investigated in the future.

---

In the final section, a process to fabricate SERS substrates with arrays of pyramidal tips was established. Here, a defect-free release over areas in the millimetre range was achieved.

These substrates were coated with MGITC molecules, and it was found that surface-enhanced Raman signals can be measured. In around 95% of the cases, a plasmonic hotspot at the tip was found. In the future, several improvements to the concepts are viable. One could increase the density of the pyramids to around  $1 \mu\text{m}^{-2}$ , allowing for a single hotspot in the laser spot and maximum density of structures at once. Furthermore, one could utilise different structuring techniques, for example nano-imprint lithography, which allow to fabricate pyramids in the scale of some ten nanometres. This would allow to measure signals from several hotspots at once. Thus, such substrates could be employed for the detection of low concentrations of Raman active molecules in solution.



# Bibliography

1. Tinsley, J. N. *et al.* Direct detection of a single photon by humans. *Nature Communications* **7**, 12172– (2016).
2. Pines, D. & Bohm, D. A Collective Description of Electron Interactions: II. Collective vs Individual Particle Aspects of the Interactions. *Phys. Rev.* **85**, 338–353 (1952).
3. Ruthemann, G. Elektronenbremsung an Röntgenniveaus. *Annalen der Physik* **437**, 135–146 (1948).
4. Lang, W. *Optik* **3**, 233 (1948).
5. Watanabe, H. Experimental Evidence for the Collective Nature of the Characteristic Energy Loss of Electrons in Solids—Studies on the Dispersion Relation of Plasma Frequency. *Journal of the Physical Society of Japan* **11**, 112–119 (1956).
6. Tredgold, R. On the interpretation of the characteristic energy losses of electrons in thin foils. *Physica* **22**, 1219–1222 (1956).
7. Ritchie, R. H. Plasma Losses by Fast Electrons in Thin Films. *Phys. Rev.* **106**, 874–881 (1957).
8. Brown, R. W., Wessel, P. & Trounson, E. P. Plasmon Reradiation From Silver Films. *Phys. Rev. Lett.* **5**, 472–473 (1960).
9. Steinmann, W. Experimental Verification of Radiation of Plasma Oscillations in Thin Silver Films. *Phys. Rev. Lett.* **5**, 470–472 (1960).
10. Ninham, B. W., Powell, C. J. & Swanson, N. Plasmon Damping in Metals. *Phys. Rev.* **145**, 209–217 (1966).
11. Zeppenfeld, K. Anisotropic plasmon behaviour in graphite. *Physics Letters A* **25**, 335–336 (1967).
12. Otto, A. Excitation of nonradiative surface plasma waves in silver by the method of frustrated total reflection. *Zeitschrift für Physik* **216**, 398–410 (1968).
13. Kretschmann, E. & Raether, H. Radiative Decay of Non Radiative Surface Plasmons Excited by Light. *Zeitschrift für Naturforsch. A* **23**, 2135–2136 (1968).
14. Dawson, P., de Fornel, F. & Goudonnet, J.-P. Imaging of surface plasmon propagation and edge interaction using a photon scanning tunneling microscope. *Phys. Rev. Lett.* **72**, 2927–2930 (1994).
15. Hecht, B., Bielefeldt, H., Novotny, L., Inouye, Y. & Pohl, D. W. Local Excitation, Scattering, and Interference of Surface Plasmons. *Phys. Rev. Lett.* **77**, 1889–1892 (1996).

16. Juan, M. L., Righini, M. & Quidant, R. Plasmon nano-optical tweezers. *Nat Photon* **5**, 349–356 (2011).
17. Li, J. *et al.* Plasmon-induced resonance energy transfer for solar energy conversion. *Nat Photon* **9**, 601–607 (2015).
18. Forati, E., Dill, T. J., Tao, A. R. & Sievenpiper, D. Photoemission-based micro-electronic devices. *Nature Communications* **7**, 13399 (2016).
19. *Confocal Raman Microscopy* 1st ed. (eds Dieing, T., Hollricher, O. & Toporski, J.) ISBN: 9783642125218 (Springer-Verlag Berlin Heidelberg, 2011).
20. Smekal, A. Zur Quantentheorie der Dispersion. *Naturwissenschaften* **11**, 873–875 (1923).
21. Raman, C. V. A new radiation. *Indian Journal of Physics* **2**, 387–398 (1928).
22. Meister, K. *et al.* Markierungsfreie Visualisierung von löslichen Metallcarbonylkomplexen in lebenden Zellen mithilfe von Raman-Mikrospektroskopie. *Angewandte Chemie* **122**, 3382–3384 (2010).
23. Aggarwal, R. *et al.* Measurement of the absolute Raman cross section of the optical phonon in silicon. *Solid State Communications* **151**, 553–556 (2011).
24. Maker, P. D. & Terhune, R. W. Study of Optical Effects Due to an Induced Polarization Third Order in the Electric Field Strength. *Phys. Rev.* **137**, A801–A818 (1965).
25. Begley, R. F., Harvey, A. B. & Byer, R. L. Coherent anti-Stokes Raman spectroscopy. *Applied Physics Letters* **25**, 387–390 (1974).
26. Synge, E. XXXVIII. A suggested method for extending microscopic resolution into the ultra-microscopic region. *The London, Edinburgh, and Dublin Philosophical Magazine and Journal of Science* **6**, 356–362 (1928).
27. Betzig, E., Lewis, A., Harootunian, A., Isaacson, M. & Kratschmer, E. Near Field Scanning Optical Microscopy (NSOM): Development and Biophysical Applications. *Biophysical Journal* **49**, 269–279 (1986).
28. Dürig, U., Pohl, D. W. & Rohner, F. Near-field optical-scanning microscopy. *Journal of Applied Physics* **59**, 3318–3327 (1986).
29. Smith, D. A. *et al.* Development of a scanning near-field optical probe for localised Raman spectroscopy. *Ultramicroscopy* **61**, 247–252 (1995).
30. Wessel, J. Surface-enhanced optical microscopy. *J. Opt. Soc. Am. B* **2**, 1538–1541 (1985).
31. Fleischmann, M., Hendra, P. & McQuillan, A. Raman spectra of pyridine adsorbed at a silver electrode. *Chemical Physics Letters* **26**, 163–166 (1974).
32. Anderson, M. S. Locally enhanced Raman spectroscopy with an atomic force microscope. *Applied Physics Letters* **76**, 3130–3132 (2000).
33. Hayazawa, N., Inouye, Y., Sekkat, Z. & Kawata, S. Metallized tip amplification of near-field Raman scattering. *Optics Communications* **183**, 333–336 (2000).

34. Stöckle, R. M., Suh, Y. D., Deckert, V. & Zenobi, R. Nanoscale chemical analysis by tip-enhanced Raman spectroscopy. *Chemical Physics Letters* **318**, 131–136 (2000).
35. Hayazawa, N., Yano, T., Watanabe, H., Inouye, Y. & Kawata, S. Detection of an individual single-wall carbon nanotube by tip-enhanced near-field Raman spectroscopy. *Chemical Physics Letters* **376**, 174–180 (2003).
36. Chen, C., Hayazawa, N. & Kawata, S. A 1.7 nm resolution chemical analysis of carbon nanotubes by tip-enhanced Raman imaging in the ambient. *Nature Communications* **5**, 3312– (2014).
37. Bailo, E. & Deckert, V. Tip-Enhanced Raman Spectroscopy of Single RNA Strands: Towards a Novel Direct-Sequencing Method. *Angewandte Chemie International Edition* **47**, 1658–1661 (2008).
38. Neugebauer, U. *et al.* On the Way to Nanometer-Sized Information of the Bacterial Surface by Tip-Enhanced Raman Spectroscopy. *ChemPhysChem* **7**, 1428–1430 (2006).
39. Sun, M., Zhang, Z., Zheng, H. & Xu, H. In-situ plasmon-driven chemical reactions revealed by high vacuum tip-enhanced Raman spectroscopy. *Scientific Reports* **2**, 647– (2012).
40. Hayazawa, N., Saito, Y. & Kawata, S. Detection and characterization of longitudinal field for tip-enhanced Raman spectroscopy. *Applied Physics Letters* **85**, 6239–6241 (2004).
41. Demming, A. L., Festy, F. & Richards, D. Plasmon resonances on metal tips: Understanding tip-enhanced Raman scattering. *The Journal of Chemical Physics* **122**, 184716 (2005).
42. Williams, C. & Roy, D. Fabrication of gold tips suitable for tip-enhanced Raman spectroscopy. *Journal of Vacuum Science Technology B* **26**, 1761–1764 (2008).
43. Yeo, B.-S., Zhang, W., Vannier, C. & Zenobi, R. Enhancement of Raman Signals with Silver-Coated Tips. *Appl. Spectrosc.* **60**, 1142–1147 (2006).
44. Höppener, C., Lapin, Z. J., Bharadwaj, P. & Novotny, L. Self-Similar Gold-Nanoparticle Antennas for a Cascaded Enhancement of the Optical Field. *Phys. Rev. Lett.* **109**, 017402 (2012).
45. Ren, B., Picardi, G. & Pettinger, B. Preparation of gold tips suitable for tip-enhanced Raman spectroscopy and light emission by electrochemical etching. *Review of Scientific Instruments* **75**, 837–841 (2004).
46. Lloyd, J. S., Williams, A., Rickman, R. H., McCowen, A. & Dunstan, P. R. Reproducible electrochemical etching of silver probes with a radius of curvature of 20 nm for tip-enhanced Raman applications. *Applied Physics Letters* **99**, 143108 (2011).
47. Kalkbrenner, T., Ramstein, M., Mlynek, J. & Sandoghdar, V. A single gold particle as a probe for apertureless scanning near-field optical microscopy. *Journal of Microscopy* **202**, 72–76 (2001).

48. Farahani, J. N. *et al.* Bow-tie optical antenna probes for single-emitter scanning near-field optical microscopy. *Nanotechnology* **18**, 125506 (2007).
49. Fleischer, M. *et al.* Gold Nanocone Near-Field Scanning Optical Microscopy Probes. *ACS Nano* **5**, 2570–2579 (2011).
50. Tanirah, O., Kern, D. P. & Fleischer, M. Fabrication of a plasmonic nanocone on top of an AFM cantilever. *Microelectronic Engineering* **141**. Micro/Nano Fabrication 2014, 215–218 (2015).
51. De Angelis, F. *et al.* Nanoscale chemical mapping using three-dimensional adiabatic compression of surface plasmon polaritons. *Nature Nanotechnology* **5**, 67–72 (2010).
52. Berweger, S., Atkin, J. M., Olmon, R. L. & Raschke, M. B. Adiabatic Tip-Plasmon Focusing for Nano-Raman Spectroscopy. *The Journal of Physical Chemistry Letters* **1**, 3427–3432 (2010).
53. Johnson, T. W. *et al.* Highly Reproducible Near-Field Optical Imaging with Sub-20-nm Resolution Based on Template-Stripped Gold Pyramids. *ACS Nano* **6**, 9168–9174 (2012).
54. Im, H. & Oh, S.-H. Oxidation Sharpening, Template Stripping, and Passivation of Ultra-Sharp Metallic Pyramids and Wedges. *Small* **10**, 680–684 (2014).
55. Julian Chen, C. *Introduction to Scanning Tunneling Microscopy: Second Edition* (Oxford University Press, 2007).
56. Ferraro, J. R., Nakamoto, K. & Brown, C. W. *Introductory Raman Spectroscopy (Second Edition)* 434 (Academic Press, 2002).
57. Hart, T. R., Aggarwal, R. L. & Lax, B. Temperature Dependence of Raman Scattering in Silicon. *Phys. Rev. B* **1**, 638–642 (1970).
58. Maier, S. A. *Plasmonics: Fundamentals and Applications* (Springer US, 2007).
59. Oubre, C. & Nordlander, P. Optical Properties of Metallodielectric Nanostructures Calculated Using the Finite Difference Time Domain Method. *The Journal of Physical Chemistry B* **108**, 17740–17747 (2004).
60. Wokaun, A. in *Solid State Physics* (eds Henry Ehrenreich, D. T. & Seitz, F.) 223–294 (Academic Press, 1984).
61. Pettinger, B., Domke, K. F., Zhang, D., Picardi, G. & Schuster, R. Tip-enhanced Raman scattering: Influence of the tip-surface geometry on optical resonance and enhancement. *Surface Science* **603**. Special Issue of Surface Science dedicated to Prof. Dr. Dr. h.c. mult. Gerhard Ertl, Nobel-Laureate in Chemistry 2007, 1335–1341 (2009).
62. Zienkiewicz, O. C., Taylor, R. L. & Zhu, J. *The Finite Element Method: Its Basis and Fundamentals* (Butterworth-Heinemann, 2013).
63. Johnson, P. B. & Christy, R. W. Optical Constants of the Noble Metals. *Phys. Rev. B* **6**, 4370–4379 (1972).
64. Kogelnik, H. & Li, T. Laser Beams and Resonators. *Appl. Opt.* **5**, 1550–1567 (1966).

65. Seidel, H., Csepregi, L., Heuberger, A. & Baumgärtel, H. Anisotropic Etching of Crystalline Silicon in Alkaline Solutions: I . Orientation Dependence and Behavior of Passivation Layers. *Journal of The Electrochemical Society* **137**, 3612–3626 (1990).
66. Elwenspoek, M. On the Mechanism of Anisotropic Etching of Silicon. *Journal of The Electrochemical Society* **140**, 2075–2080 (1993).
67. Horcas, I. *et al.* WSXM: A software for scanning probe microscopy and a tool for nanotechnology. *Review of Scientific Instruments* **78** (2007).
68. Martina, M., Röhler, S., Ingino, P. & Burkhardt, C. Correlative SPM, Raman and SEM analytic of biomedical devices and coatings. *Microscopy and Analysis SPM supplement*, 23–28 (2015).
69. Martina, M., Fleischer, M. & Burkhardt, C. Template stripping and bonding of smooth probes with nanoscale features for tip-enhanced Raman spectroscopy. *Microelectronic Engineering* **171**, 31–36 (2017).
70. Micic, M., Klymyshyn, N., Suh, Y. D. & Lu, H. P. Finite Element Method Simulation of the Field Distribution for AFM Tip-Enhanced Surface-Enhanced Raman Scanning Microscopy. *The Journal of Physical Chemistry B* **107**, 1574–1584 (2003).
71. Downes, A., Salter, D. & Elfick, A. Finite Element Simulations of Tip-Enhanced Raman and Fluorescence Spectroscopy. *The Journal of Physical Chemistry B* **110**, 6692–6698 (2006).
72. Roth, R. M. *et al.* Resonant-plasmon field enhancement from asymmetrically illuminated conical metallic-probe tips. *Opt. Express* **14**, 2921–2931 (2006).
73. Ossikovski, R., Nguyen, Q. & Picardi, G. Simple model for the polarization effects in tip-enhanced Raman spectroscopy. *Phys. Rev. B* **75**, 045412 (2007).
74. Bouhelier, A. & Novotny, L. in *Surface Plasmon Nanophotonics* (eds Brongersma, M. L. & Kik, P. G.) 139–153 (Springer Netherlands, Dordrecht, 2007).
75. Hegner, M., Wagner, P. & Semenza, G. Ultralarge atomically flat template-stripped Au surfaces for scanning probe microscopy. *Surface Science* **291**, 39–46 (1993).
76. Fernandez-Cuesta, I. *et al.* V-groove plasmonic waveguides fabricated by nanoimprint lithography. *Journal of Vacuum Science & Technology B: Microelectronics and Nanometer Structures Processing, Measurement, and Phenomena* **25**, 2649–2653 (2007).
77. Nagpal, P., Lindquist, N. C., Oh, S.-H. & Norris, D. J. Ultrasoft Patterned Metals for Plasmonics and Metamaterials. *Science* **325**, 594–597 (2009).
78. Hu, Y., Kumar, P., Xu, R., Zhao, K. & Cheng, G. J. Ultrafast direct fabrication of flexible substrate-supported designer plasmonic nanoarrays. *Nanoscale* **8**, 172–182 (2016).
79. Kaye, G. & Laby, T. *Tables of Physical and Chemical Constants* 16th (eds Noyes, J., Asher, J., Jones, O. & Phillips, G.) (Longman Scientific & Technical, 1995).

80. Nielsen, C. B., Christensen, C., Pedersen, C. & Thomsen, E. V. Particle Precipitation in Connection with KOH Etching of Silicon. *Journal of The Electrochemical Society* **151**, G338–G342 (2004).
81. Genolet, G. *et al.* Soft, entirely photoplastic probes for scanning force microscopy. *Review of Scientific Instruments* **70**, 2398–2401 (1999).
82. Deal, B. E. & Grove, A. S. General Relationship for the Thermal Oxidation of Silicon. *Journal of Applied Physics* **36**, 3770–3778 (1965).
83. Tinguely, J.-C. *et al.* Gold Nanoparticles for Plasmonic Biosensing: The Role of Metal Crystallinity and Nanoscale Roughness. *BioNanoScience* **1**, 128–135 (2011).
84. Jose, J. *et al.* Individual Template-Stripped Conductive Gold Pyramids for Tip-Enhanced Dielectrophoresis. *ACS Photonics* **1**, 464–470 (2014).
85. Chen, H. S. & Turnbull, D. Thermal Properties of Gold-Silicon Binary Alloy near the Eutectic Composition. *Journal of Applied Physics* **38**, 3646–3650 (1967).
86. Pettinger, B., Picardi, G., Schuster, R. & Ertl, G. Surface-enhanced and STM-tip-enhanced Raman Spectroscopy at Metal Surfaces. *Single Molecules* **3**, 285–294 (2002).
87. Pettinger, B., Ren, B., Picardi, G., Schuster, R. & Ertl, G. Nanoscale Probing of Adsorbed Species by Tip-Enhanced Raman Spectroscopy. *Phys. Rev. Lett.* **92**, 096101 (2004).
88. Jiang, N. *et al.* Observation of Multiple Vibrational Modes in Ultrahigh Vacuum Tip-Enhanced Raman Spectroscopy Combined with Molecular-Resolution Scanning Tunneling Microscopy. *Nano Letters* **12**. PMID: 22200250, 5061–5067 (2012).
89. Zhang, R. *et al.* Chemical mapping of a single molecule by plasmon-enhanced Raman scattering. *Nature* **498**, 82–86 (2013).
90. Dong, Z. C. *et al.* Generation of molecular hot electroluminescence by resonant nanocavity plasmons. *Nat Photon* **4**, 50–54 (2010).
91. Jiang, N. *et al.* Nanoscale Chemical Imaging of a Dynamic Molecular Phase Boundary with Ultrahigh Vacuum Tip-Enhanced Raman Spectroscopy. *Nano Lett.* **16**, 3898–3904 (2016).
92. Michaelson, H. B. The work function of the elements and its periodicity. *Journal of Applied Physics* **48**, 4729–4733 (1977).
93. Skriver, H. L. & Rosengaard, N. M. Surface energy and work function of elemental metals. *Phys. Rev. B* **46**, 7157–7168 (1992).
94. Jia, J.-F., Inoue, K., Hasegawa, Y., Yang, W.-S. & Sakurai, T. Scanning Tunneling Microscopy Measurements of the Local Work Function around Steps on the Au/Cu(111) Surface (STM-local states). *Science reports of the Research Institutes, Tohoku University. Ser. A, Physics, chemistry and metallurgy* **44**, 105–108 (1997).
95. Wang, Z. & Rothberg, L. J. Origins of Blinking in Single-Molecule Raman Spectroscopy. *The Journal of Physical Chemistry B* **109**, 3387–3391 (2005).

96. Schwan, J., Ulrich, S., Batori, V., Ehrhardt, H. & Silva, S. R. P. Raman spectroscopy on amorphous carbon films. *Journal of Applied Physics* **80**, 440–447 (1996).
97. Ferrari, A. C. & Robertson, J. Interpretation of Raman spectra of disordered and amorphous carbon. *Phys. Rev. B* **61**, 14095–14107 (2000).
98. Ferrari, A. C. & Robertson, J. Raman spectroscopy of amorphous, nanostructured, diamond-like carbon, and nanodiamond. *Philosophical Transactions of the Royal Society of London A: Mathematical, Physical and Engineering Sciences* **362**, 2477–2512 (2004).
99. Sakamoto, S., Okumura, M., Zhao, Z. & Furukawa, Y. Raman spectral changes of PEDOT–PSS in polymer light-emitting diodes upon operation. *Chemical Physics Letters* **412**, 395–398 (2005).
100. Mehtani, D. *et al.* Nano-Raman spectroscopy with side-illumination optics. *Journal of Raman Spectroscopy* **36**, 1068–1075 (2005).
101. Lorenz, H. *et al.* SU-8: a low-cost negative resist for MEMS. *Journal of Micromechanics and Microengineering* **7**, 121 (1997).
102. Conradie, E. H. & Moore, D. F. SU-8 thick photoresist processing as a functional material for MEMS applications. *Journal of Micromechanics and Microengineering* **12**, 368 (2002).
103. Keller, S., Haefliger, D. & Boisen, A. Fabrication of thin SU-8 cantilevers: initial bending, release and time stability. *Journal of Micromechanics and Microengineering* **20**, 045024 (2010).
104. Geerlings, J. *et al.* Design and fabrication of in-plane AFM probes with sharp silicon nitride tips based on refilling of anisotropically etched silicon moulds. *Journal of Micromechanics and Microengineering* **24**, 105013 (2014).
105. Li, B., Liu, M. & Chen, Q. Low-stress ultra-thick SU-8 UV photolithography process for MEMS. *Journal of Micro/Nanolithography, MEMS, and MOEMS* **4**, 043008 (2005).
106. Hammacher, J. *et al.* Stress engineering and mechanical properties of SU-8-layers for mechanical applications. *Microsystem Tech.* **14**, 1515–1523 (2008).
107. Meirovitch, L. *Analytical Methods in Vibrations* (Pearson, 1967).
108. Roch, I., Bidaud, P., Collard, D. & Buchaillot, L. Fabrication and characterization of an SU-8 gripper actuated by a shape memory alloy thin film. *Journal of Micromechanics and Microengineering* **13**, 330 (2003).
109. Cherukulappurath, S., Johnson, T. W., Lindquist, N. C. & Oh, S.-H. Template-Stripped Asymmetric Metallic Pyramids for Tunable Plasmonic Nanofocusing. *Nano Letters* **13**, 5635–5641 (2013).
110. Nie, S. & Emory, S. R. Probing Single Molecules and Single Nanoparticles by Surface-Enhanced Raman Scattering. *Science* **275**, 1102–1106 (1997).
111. Liu, G. L. & Lee, L. P. Nanowell surface enhanced Raman scattering arrays fabricated by soft-lithography for label-free biomolecular detections in integrated microfluidics. *Applied Physics Letters* **87**, 074101 (2005).

112. Cottat, M. *et al.* Soft UV nanoimprint lithography-designed highly sensitive substrates for SERS detection. *Nanoscale Research Letters* **9**, 623 (2014).
113. Kahl, M., Voges, E., Kostrewa, S., Viets, C. & Hill, W. Periodically structured metallic substrates for SERS. *Sensors and Actuators B: Chemical* **51**, 285–291 (1998).

# A. Appendix

## Metal lift-off

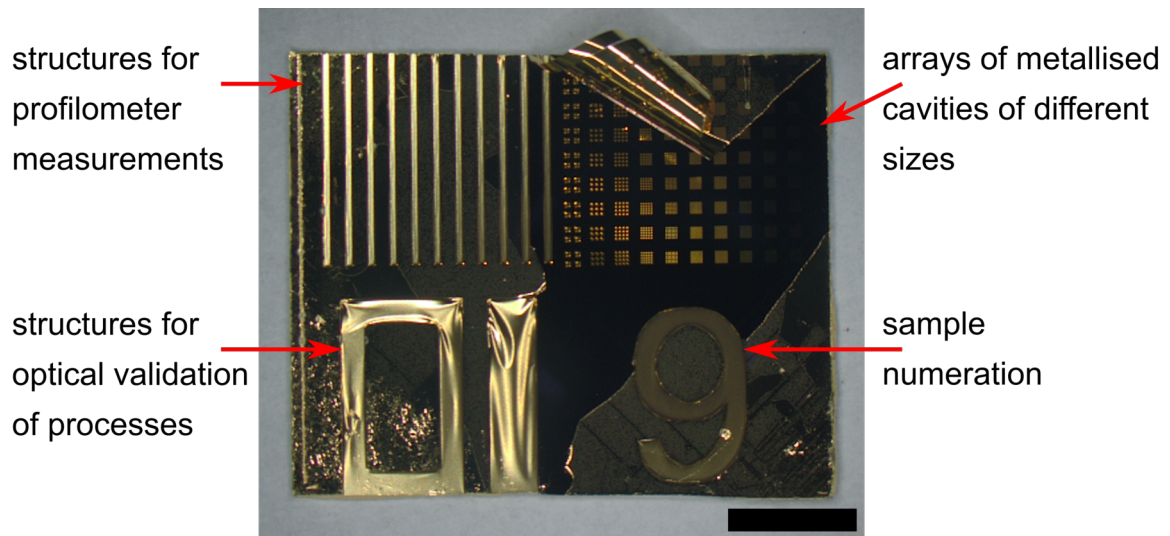


Figure A.1.: Labelled image of a fabricated sample showing metallised moulds and additional structures. The sample was imaged during the mechanical stripping of the gold layer. (scale bar 5 mm).

## Silver STM-TERS probes

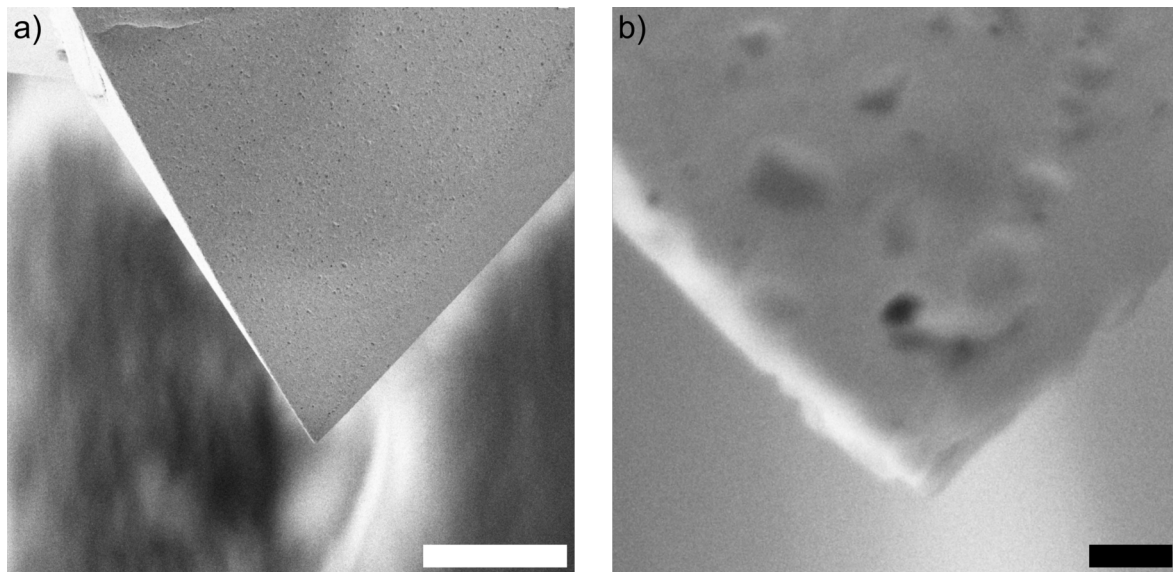


Figure A.2.: SEM images of a template-stripped silver tip released by ball bonding to a wire. The metallisation of the mould was performed by sputter deposition of a 100 nm thick silver layer followed by a 900 nm thick gold layer. The gold layer is needed to facilitate a stable bond during release. a) scale bar 10  $\mu\text{m}$  b) scale bar 200 nm.

---

## TERS probes for shear force feedback

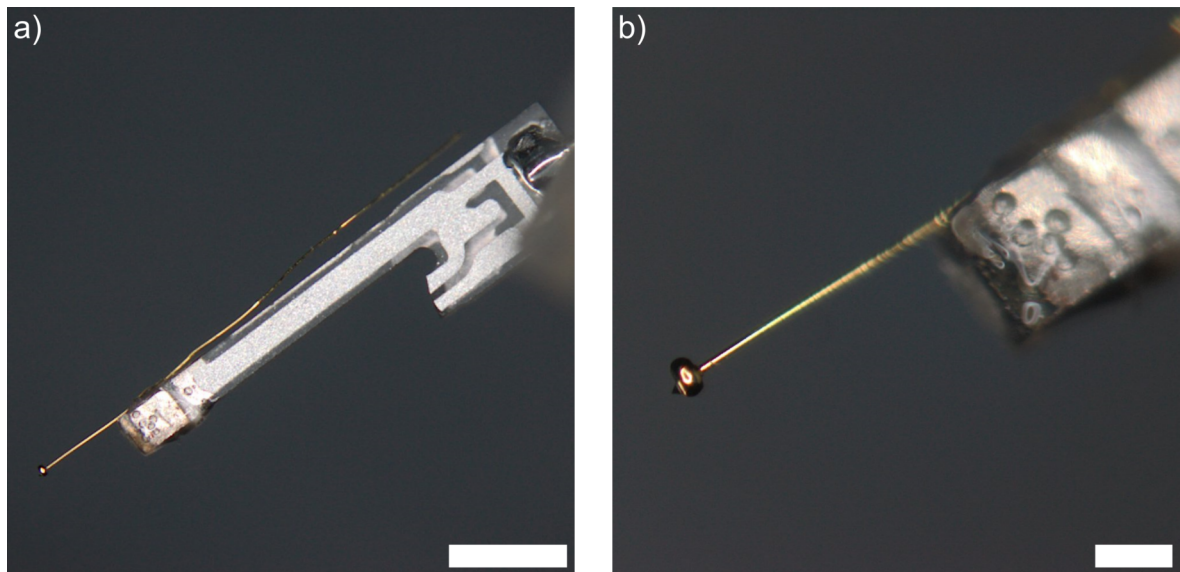


Figure A.3.: Optical images of a pyramidal gold tip released by ball bonding to a gold wire, and attached to a tuning fork (defective) for shear force feedback. a) scale bar 1 mm b) scale bar 200  $\mu\text{m}$ .